INAUGURAL-DISSERTATION

zur
Erlangung der Doktorwürde
der
Naturwisschenschaftlich-Mathematischen
Gesamtfakultät
der
Ruprecht-Karls-Universität
Heidelberg

Vorgelegt von

M.Sc. Chem. Eng. Trupti Kathrotia

aus

Visavadar, India

Tag der mündlichen Prüfung:

19. 05. 2011

Reaction Kinetics Modeling of OH*, CH*, and C_2* Chemiluminescence

Gutachter: Prof. Dr. Uwe Riedel

Prof.(apl.) Dr. Hans-Robert Volpp

Abstract

In the combustion processes, spontaneous emission of chemiluminescence species responsible for ultra-violet and visible light is in abundance. Due to its natural occurrence, it offers an inexpensive diagnostic tool for flames and other combustion processes. It is non-intrusive in nature and gives the facility to avoid expensive laser instrumentation.

In hydrocarbon oxidation most common electronically excited species are OH*, CH*, C_2*, and CO_2*, where * represents the electronically excited state of a given radical or molecule. In the early 1970s chemiluminescence has been identified as a marker for heat release, reaction zone, and equivalence ratio, thereby providing a relatively easy diagnostics alternative for online measurement of these features in practical combustion applications. However, the quantitative relationship between chemiluminescence, heat release, and equivalence ratio is mostly unknown except for a few correlations available in literature over small range of conditions. Therefore a reaction kinetic model predicting these species is necessary for the fundamental understanding of the chemiluminescence. This mechanism then can be provided for predicting excited species in simulations of various combustion devices.

A detailed reaction mechanism of chemiluminescence is not well studied. Therefore, the objective of this work is to develop a reaction mechanism of chemiluminescent species which can predict their concentrations in shock-tube and one-dimensional laminar flame experiments.

The mechanism developed in this thesis is validated against various experimental conditions in shock-tube experiments where it reproduces the ignition delay time very well. In addition, the species profiles which provide a more stringent test on the mechanism validation are calculated to reproduce the measured excited species concentrations in laminar premixed and non-premixed flames. The comparison proves accuracy of the mechanism.

The mechanism presented provides therefore a first step to quantitative understanding of the excited species and can be further used in the simulation of practical combustion systems.

Zusammenfassung

In Verbrennungsprozessen, ist Chemilumineszenz verantwortlich für einen großen Teil des ultravioletten und sichtbaren Lichts. Aufgrund ihres natürlichen Auftretens, bietet die spektroskopische Untersuchung der Strahlung ein kostengünstiges Diagnose Verfahren für Flammen und andere Verbrennungsprozesse: Das Messverfahren ist berührungslos, wodurch eine Beeinflussung der Flamme durch die Messmethode vermieden wird. Darüber hinaus erfordert die messtechnische Erfassung der Chemilumineszenz keine teure Instrumentierung wie etwa im Falle laserdiagnostischer Messmethoden.

In der Kohlenwasserstoffoxidation sind die häufigsten, elektronisch angeregten Spezies OH*, CH*, C_2* und CO_2*, wobei * den elektronisch angeregten Zustand eines bestimmten Radikals oder eines Moleküles bezeichnet. In den frühen 1970er Jahren wurde die Chemilumineszenz als Marker für Wärmefreisetzung, Reaktionszone und Äquivalenzverhältnis identifiziert, wodurch heute ein relativ einfaches Messverfahren zur Online-Messung dieser Größen in praktischen Verbrennungsprozessen gegeben ist. Allerdings ist die quantitative Beziehung zwischen Chemilumineszenz, Wärmefreisetzung und Äquivalenzverhältnis bis auf einige Angaben aus der Literatur, die einen begrenzten Gültigkeitsbereich haben, unbekannt. Die Voraussetzung für die vollständige, quantitative Beschreibung ist das Verständnis der reaktionskinetischen Vorgänge, die zur Bildung angeregter Spezies führen. Mechanismen, die in der Lage sind diese Vorgänge darzustellen, können in Simulationen von verbrennungstechnischen Apparaten eingesetzt werden.

Jedoch ist der reaktionskinetische Mechanismus, der Bildung und Verbrauch dieser angeregten Spezies darstellen kann, nicht vollständig verstanden. Daher ist das Ziel dieser Arbeit die Entwicklung eines Reaktionsmechanismus, der die zu erwartenden Mengen angeregter Spezies vorherzusagen vermag.

Der in dieser Arbeit dargestellte Mechanismus wird zunächst unter unterschiedlichen Bedingungen mit experimentellen Daten aus Stoßwellenrohrversuchen validiert. Es wird eine sehr gute Übereinstimmung zwischen gemessenen und berechneten Zündverzugszeiten erzielt. Darüber hinaus werden eindimensionale vorgemischte und nichtvorgemischte laminare Flammen mit Hilfe dieses Mechanismus berechnet. Der Vergleich gemessener und

berechnter räumlicher Konzentrationsprofile in diesen Flammen stellt ein sehr strenges Kriterium für die Validierung des Mechanismus dar. Es zeigt sich beim Vergleich zwischen Rechnung und Versuch, dass der Mechanismus in der Lage ist angeregte Spezies mit hoher Genauigkeit unter Flammenbedingungen vorherzusagen.

Somit stellt der Mechanismus einen ersten Schritt für die quantitative Berechnung angeregter Spezies dar und kann in der Simulation realer Verbrennungssysteme eingesetzt werden.

Acknowledgement

It is my great pleasure to acknowledge all the people who helped me directly or indirectly to accomplish this dissertation.

First and foremost, I express my sincere gratitude towards late Prof. Jürgen Warnatz for giving me opportunity to work for my dissertation in his group. I thank my supervisor Prof. Uwe Riedel for his constant inspiration and support towards the work and giving me have independence in my work.

I gratefully acknowledge Prof. Ulrich Maas, Universität Karlsruhe, for providing his code INSFLA and Deutsche Forschungsgemeinschaft (DFG) for financial support through out this work.

My sincere thanks to Ingrid Hellwig for organising administration related hurdles. I thank all my coworkers at IWR and DLR-Stuttgart for making a cheerful work atmosphere. Helpful meeting and discussion with ChemLum-project members will always be a pleasant memory.

Last but not least, I am thankful to my family for their constant encouragement and support. I dedicate this thesis to my parents.

Trupti Kathrotia
Heidelberg, March 2011

Contents

1 Introduction

1.1 Flame spectra

Luminescence occurring due to chemical excitation, referred to as *Chemiluminescence* (CL), is found in the visible and ultra-violet band of flame spectra. In hydrocarbon flames the four major emitters found are OH*, CH*, C_2*, and CO_2* [1], here star (*) refers to electronically excited molecules. The study of CL dates back to 1960s where Gaydon published his pioneering works on the flame spectroscopy. The flame spectra

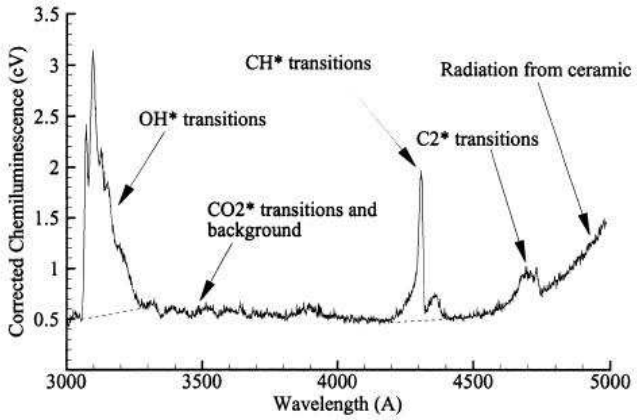

Figure 1.1: Flame spectrum of a hydrocarbon flame showing the appearance of various excited species at different wavelengths [2].

in the visible and ultra-violet (UV) regions occur generally due to the transition of electrons in molecules from one configuration to another configuration. A typical flame spectrum obtained from hydrocarbon combustion is shown in Fig. 1.1. In this figure, the detected chemiluminescence is corrected from background emission. Most of the stable product of combustion does not give strong emission spectra in the visible or UV

region. However, the OH* radical gives a strong spectrum with peak intensity at about 309 nm. In the flame zone, other unstable species that give emission in the visible and near ultraviolet region are CH*, C_2*, and CO_2*. The OH* emission in hydrogen and nitrous oxide-hydrogen flames is weak compared to the one found in hydrocarbon flame and the spectra of hydrocarbon flames are more complex. The emission of CO_2* appears as a continuum which extends from 300 nm to 600 nm seen as blue color. In the primary combustion zone, the emission of CH at about 387 nm and at 432 nm are seen. In addition to CH*, the bands of C_2* between 436 nm and 564 nm called Swan bands are found in the visible region of flame spectra. The Swan bands of C_2* are visible mainly in the fuel rich gas mixtures.

The lower state of OH* is the ground state which is an inverted doublet state ($X^2\ \Pi$). The higher state is the normal doublet Σ state OH($A^2\ \Sigma^+$). In addition to this there exists excited OH($B^2\ \Sigma^+$) state from 420 nm to 600 nm in the visible region and another OH($C^2\ \Sigma^+$) in the ultraviolet region from 225 to 260 nm. As these two bands are not identified in flames and they are not studied in combustion diagnostics. In present work only OH($A^2\ \Sigma^+$) is considered for the OH* chemiluminescence.

In the CH* spectrum, three major bands are emitted by the CH molecule. The one seen at a wavelength of 431 nm (CH($A^2\Delta$)) is the strongest of the three bands (accounts for about 80% of total CH*) and appears violet in the visible region. The other two low populated states are CH($B^2\Sigma^-$) and CH($C^2\Delta$). The present work considers mainly CH($A^2\Delta$) state. With a very recent availability of CH($B^2\Sigma^-$) measurement this CH* state is also discussed.

Online measurement and control of the heat release rate and local equivalence ratio in practical combustion devices are of great importance in industrial applications. A precise control of combustion processes in practical applications is needed to avoid pollutants and to save limited resources of the existing hydrocarbon fuels. The online measurement of combustion processes would help to reduce pollutant emission, increase the efficiency and to control instabilities inside the devices. This requires measurement of equivalence ratio and flame temperature during the operation. In practical combustion applications, a harsh environment (e.g. high temperature, soot, turbulence) exists which makes the combustion diagnostics difficult. Many optical measurement techniques have been considered for the diagnostic applications due to their compatibility at extreme conditions in combustors. However, cost inefficiency, time, and other limitations

have made them inattractive. Due to the extreme conditions in practical combustion applications, the diagnostic tools require sensors that can withstand it. Common optical diagnostic methods such as absorption, scattering, and fluorescence need external light sources which makes them expensive. Chemiluminescence on the other hand has the advantage that the measured light signal occurs naturally in the combustion zone and only a simple optical detection system is needed. Also, it has found great importance in the field of diagnostics due to its simplicity (in terms of measurement) and non-intrusive nature (no outside probe is required thereby the system is undisturbed). However, this would require reliable method by which online measurement is possible. Over the years, chemiluminescence measurement has gathered attention for its simple non-intrusive measurement techniques compared to expensive laser measurements. It has been identified from a few scattered studies [3, 4] that excited species such as OH* and CH* occur within the reaction zone, thereby providing identification of the reaction zone. In addition, chemiluminescence has been seen to have a correlation with the heat release rate [3, 4], and also with the equivalence ratio. Thereby, from the online control, sufficient information can be gathered to understand combustion process prevailing inside the combustor.

As early as in the 1970s, chemiluminescence has been identified as a potential marker for the heat release rate, reaction zone, and equivalence ratio. The major CL species are formed in the thin reaction zone thereby their detection can provide information on the location of reaction zone [5]. So far, scatter modeling efforts to relate chemiluminescence and heat release have been done varying from premixed laminar to moderately turbulent flame conditions [3,4,6–10]. Most of the studies on chemiluminescence are limited to particular conditions (e.g. at specific fuel stoichiometry, given temperature and pressures, type of burners, strain rates) and so their interpretation may not be extrapolated to other conditions. Due to which, the use of chemiluminescence in combustion diagnostics remains still limited.

Chemiluminating species are considered as important intermediates that characterize the reaction zone due to its appearance in the narrow region of the flame front and are a potential marker for the heat release and the reaction zone in combustion systems [4, 6, 11, 12]. The CL species have advantage over stable species, such as formaldehyde CH_2O, HCO, which are also considered to be correlating well with the heat release location but are difficult to measure. Samaniego et al. [7] studied CO_2* chemiluminescence in lean methane and propane premixed flame and presented a quantitative correlation between

CO_2* emission and heat release rate. They investigated CO_2* in laminar and turbulent premixed flames. Najm and coworkers [6] studied several flame observables such as the concentrations of OH, CH, CO, CH_3, and CH_2O; various concentration products such as [OH][CH_2O], [OH][CH_4], and [OH][CO] in premixed methane flames with a two-dimensional counter-rotating vortex pair. They also studied the concentration product of [CH][O_2], [C_2H][O], and [CO][O] related to OH*, CH*, and C_2* formation respectively. They found that the concentration product of precursors of the OH* and CO_2* were well correlating with the peak heat release rate. Haber et al. [8] examined the relationship between OH* and CH* light emissions and heat release in Bunsen Burner flames. They suggested OH* as a good indicator of heat release whereas CH* as not an adequate indicator of the heat release in methane combustion. Among recent studies Hardalupas et al. [3] and Panoutsos and coworkers [4] studied OH*, CH*, C_2*, and CO_2* emission in natural gas-air, methane-air premixed counter-flow flames. They studied the effect of strain rate and equivalence ratio on chemiluminescence intensity and its applicability as a heat release indicator. They found mainly OH*, CH* and CO_2* as good indicators of the heat release but not C_2*. The intensity ratio of OH*/CH* was found to be a good measure of the local equivalence ratio. They also explained a potential technique to utilize chemiluminescence in practical burners for measuring the time-dependent local equivalence ratio. In [5] a numerical study in premixed laminar flame condition was aimed to investigate the potential of excited species as a heat release marker. The usefulness of chemiluminescence for sensing the equivalence ratio in a combustion system has been studied by Nori et al. [9,10]. They found the ratio of CH* to OH* correlating with the fuel stoichiometry in a lean methane system. However, they were unable to hold the correlation beyond certain limits of temperature and pressure. The intensities from CH*, C_2*, OH*, and CO_2* have been used to determine the location of the reaction zone as well. Their experimental-modeling study also showed the utility of CH*, under certain temperature and pressure condition, for sensing the heat release rate.

1.2 Motivation

Experiments for a wide range of conditions of temperature, pressure, strain rate, equivalence ratio, and types of combustors are restricted due to their limitations on time and cost. Modeling studies, on the other hand provide an alternative flexible approach with

all above advantages over experiments. An understanding of the chemiluminescence in combustors requires detailed studies of formation and consumption of the excited species. The aim of the present work is to provide such detailed chemical kinetics reaction mechanism which can give information on the occurrence of the chemiluminating species in the reaction zone and their concentrations that can be validated with the measured intensities in various shock-tube and laminar flame measurements. The chemiluminescence mechanism developed will provide a basis for studies of chemiluminescence and its relation to heat release rate, equivalence ratios, marker of the reaction zone in combustion applications.

1.3 Research goals

The concentration of excited species in flames is much lower (atleast four to five orders of magnitude) compared to the important intermediate species (CH, OH, H_2O). Therefore, the incorporation of the chemiluminescence sub-mechanism into basic hydrocarbon oxidation mechanism does not affect global properties like ignition delay times and flame speeds. However, some of the intermediate products of combustion such as CH, H, O, C_2H, and C_2 provide the basis for the formation of chemiluminating chemistry. The concentration of these species is not important for the validation of the global parameters (flame velocity, ignition delay times) of basic hydrocarbon chemistry. However, these species are important in formation of excited species. Therefore, for the development of chemiluminescence mechanism, it is very important to validate first the intermediate species chemistry, keeping the global parameter unvaried. In addition, ground state C_2 and C_3 are important precursors in the formation of excited CH* and C_2*. The reaction kinetics of these species is not yet a part of hydrocarbon chemistry and therefore its incorporation and validation is also important part of present work. So, in order to provide validated chemiluminescence reaction mechanism, the objective of the present work is threefold

(i) Modification of the basic hydrocarbon chemistry with respect to its important intermediates concentrations (CH, C_2H).

(ii) Addition of C-, C_2-, and C_3-species reactions.

(iii) Development and validation of a reaction kinetic scheme to describe chemiluminescence.

2 Physical Chemistry Background

A chemically reacting flow system can be characterized by specifying its properties such as pressure, density, temperature, flow velocity, and concentration of species at each point in space and time. These properties can vary with time and space. Some of these properties such as the mass, energy, and momentum are conserved and their change is described by conservation equations. This equations are the starting point of the mathematical description of reacting flows. The different systems vary from each other by boundary conditions and physicochemical conditions.

2.1 Homogeneous reacting system

The ignition delay times measured in a shock-tube are modeled by treating the reaction system as a homogeneous mixture heated up by the shock wave. Therefore, the general conservation equations are reduced to ordinary differential equations [13].

Conservation of mass:
The equation for conservation of total mass is also called continuity equation which explains that the change of total mass with respect to time is zero,

$$\frac{\partial m}{\partial t} = \frac{\partial(\rho V)}{\partial t} = 0 \tag{2.1}$$

Here m is the total mass and V is the volume of the system, ρ is the density of the mixture, and t is the time.

Conservation of species mass:

$$\frac{\partial \rho_i}{\partial t} = M_i \dot{\omega}_i \tag{2.2}$$

with $\rho_i = \rho w_i$. Here ρ_i is the partial density of the species i, w_i is the mass fraction of species i, $\dot{\omega}_i$ is the chemical rate of production of species i (molar scale), and M_i is the molar mass of species i. With ρ being constant we obtain

$$\frac{\partial w_i}{\partial t} = \frac{M_i}{\rho}\dot{\omega}_i. \tag{2.3}$$

Conservation of energy:

$$\frac{\partial T}{\partial t} - \frac{1}{\rho c_p}\frac{\partial p}{\partial t} + \frac{1}{\rho c_p}\sum_{i=1}^{n_s}\dot{\omega}_i h_i M_i = 0 \tag{2.4}$$

where p = pressure, T = temperature, c_p is the specific heat capacity at constant pressure, n_s = number of species, and h_i is the specific enthalpy of species i.

The system is closed by the Ideal Gas Law :

$$pV = nRT. \tag{2.5}$$

The equation system is solved numerically by the software packages DASSL (using the backward differentiation formula) [14] or LIMEX (using extrapolation method) [15].

2.2 One-dimensional laminar flames

2.2.1 The structure of laminar premixed flames

Laminar premixed flat flame offer the advantage of well defined flame conditions suitable for fundamental investigations experimentally and also for mathematical treatment of the combustion processes. The structure of a laminar premixed flat flame consists of a porous disk burner, ∼10 cm in diameter, through which the premixed fuel and air flows (see Fig. 2.1). The fuel and oxidizer emerge from the disk and flow into the flame. This flame appears as a luminous disk located few mm above the porous disk. If the burner diameter is large enough, the curvature effects at the edges can be neglected and within the edges, a flat flame is obtained.

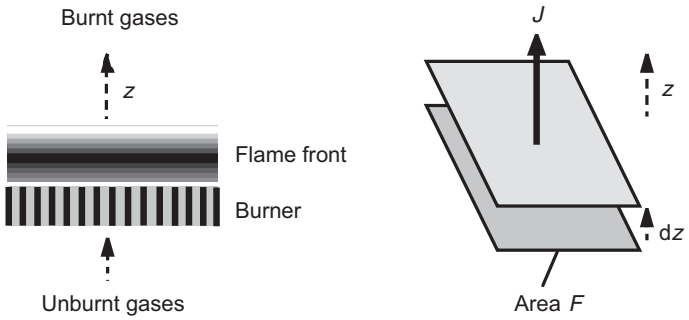

Figure 2.1: Schematic sketch of a laminar premixed flat flame.

The one-dimensional treatment is further simplified by the following assumptions [13]:

(i) the flame is stationary.

(ii) the perfect gas law is valid.

(iii) external forces such as gravitation are negligible.

(iv) the system is continuous as the mean free path of the molecules is small compared to the flame thickness.

(v) the pressure is constant.

(vi) the kinetic energy of the gas flow is negligible compared to other terms in the energy conservation equation.

(vii) the Dufour-effect (thermal diffusion) can be neglected.

(viii) heat flux due to the radiation of gases and particles is negligible (acceptable for non-sooting flames).

(ix) the system is in local thermal equilibrium.

For any conserved variable $E(z,t)$ in a one-dimensional system, the general relation is

$$\frac{\partial W}{\partial t} + \frac{\partial J}{\partial z} = Q \tag{2.6}$$

where W is density of conserved variable (E per volume), J is flux of the conserved variable (E per surface·time), Q is source (or sink) of the conserved variable (E per volume·time).

Conservation of overall mass:
The density W in the conservation equation is given by the total mass density ρ. The flux describes the movement of mass and is given by $J = \rho v$. Here v is mean mass velocity. The source term of the mass conservation equation (2.6) is zero (Q = 0) since chemical reactions neither create nor destroy mass:

$$\frac{\partial \rho}{\partial t} + \frac{\partial(\rho v)}{\partial z} = 0. \tag{2.7}$$

Conservation of species mass:
The density velocity W is given by partial density of species i which is $\rho_i = m_i/V = w_i\rho$. The flux J is given by $J = \rho_i v_i$. In addition, it has a source term which describes the formation or consumption of the species i in chemical reactions. Therefore $Q = M_i\dot{\omega}_i$ and the conservation equation reads

$$\frac{\partial \rho w_i}{\partial t} + \frac{\partial \rho w_i v_i}{\partial z} = M_i\dot{\omega}_i = r_i, \tag{2.8}$$

where r_i = chemical rate of production (mass scale). The mass velocity v_i of species i is composed of the mean mass velocity v of the center of mass of the mixture and a diffusion velocity V_i (relative to the center of mass), which is caused by molecular transport due to concentration gradients of the species i, $v_i = v + V_i$.

with $\rho_i = \rho w_i$, $v_i = v + V_i$, and $j_i = \rho w_i V_i$,

$$\frac{\partial \rho w_i}{\partial t} + \frac{\partial \rho v w_i}{\partial z} + \frac{\partial j_i}{\partial z} = M_i\dot{\omega}_i. \tag{2.9}$$

Conservation of energy:
The W term in equation (2.6) is given by $\sum_i \rho_i h_i = \sum_i \rho w_i h_i$. Here h_i is the specific enthalpy of species i. The flux $J = \sum_i \rho_i v_i h_i + j_q = \sum_i \rho v_i w_i h_i + j_q$, in which j_q is the heat flux corresponding to the diffusion flux introduced in the species mass equation (j_i). No source term is considered ($Q = 0$).

$$\sum_{i=1}^{n} \frac{\partial \rho w_i h_i}{\partial t} + \sum_{i=1}^{n} \frac{\partial \rho v w_i h_i}{\partial z} + \sum_{i=1}^{n} \frac{\partial}{\partial z}(\rho V_i w_i h_i) + \frac{\partial j_q}{\partial z} = 0. \tag{2.10}$$

Inserting a few relations such as $v_i = v + V_i$, and the diffusion flux j_i yields the relation,

$$\rho v \sum_{i=1}^{n} w_i \frac{\partial h_i}{\partial z} + \rho \sum_{i=1}^{n} w_i \frac{\partial h_i}{\partial t} + \sum_{i=1}^{n} h_i M_i \dot{\omega}_i + \sum_{i=1}^{n} j_i \frac{\partial h_i}{\partial z} + \frac{\partial j_q}{\partial z} = 0. \tag{2.11}$$

The temperature is calculated by solving this energy equation (2.11). After inserting the heat flux j_q and using the relation $c_{p,i}\mathrm{d}T = \mathrm{d}h_i$ and $c_p = \sum w_i c_{pi}$ yields,

$$\rho c_p \frac{\partial T}{\partial t} = \frac{\partial}{\partial t}(\lambda \frac{\partial T}{\partial z}) - (\rho v c_p + \sum_{i=1}^{n} j_i c_{p,i}) \frac{\partial T}{\partial z} - \sum_{i=1}^{n} h_i \dot{\omega}_i \tag{2.12}$$

2.2.2 The structure of laminar non-premixed flames

The flame structure of non-premixed flames would require to solve the three-dimensional conservation equations for overall mass, momentum, enthalpy and mass of species i. However, the problem can be reduced spatially to one dimension by applying the boundary layer assumption (i.e. neglecting the diffusion in the direction orthogonal to streamline). As shown in Fig. 2.2, examples of burners providing one-dimensional configurations are the Tsuji burner [16] (it has a cylinder in cross flow) and the opposed-jet flow burner (where a laminar fuel flow leaves one duct to stagnate against the laminar oxidizer flow emerging from the opposite duct).

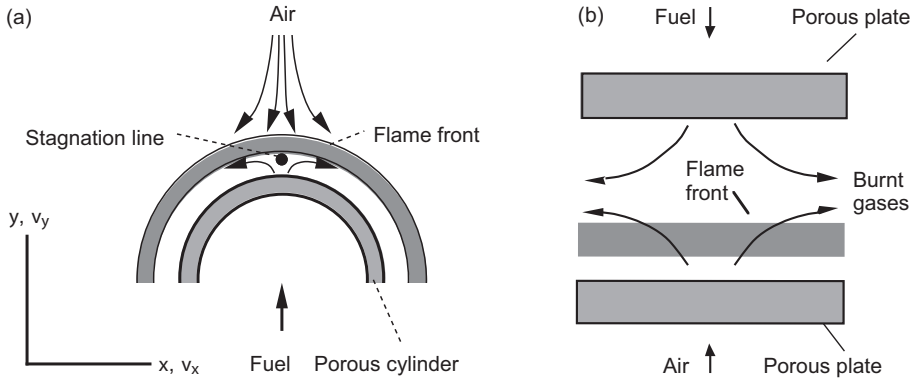

Figure 2.2: Schematic example of counterflow nonpremixed flame burner (a) Tsuji burner (b) opposed flow burner.

The following assumptions lead to an equation system which has only the time t and

one spatial coordinate y as independent variable [13].

(i) the solution is considered along the y axis

(ii) the normal velocity v_y is function of y only

(iii) the tangential velocity component v_x is proportional to the coordinate tangential to the flame x

(iv) all species mass fractions and temperature are functions solely of coordinate y normal to the flame

The equation system which describes the non-premixed flame is similar to premixed flames. The following conservation equations hold [13]:

Conservation equation for total mass:

$$\frac{\partial \rho}{\partial t} + 2\rho G + \frac{\partial(\rho v_y)}{\partial y} = 0 \tag{2.13}$$

Here v_x and v_y are normal and tangential velocity component respectively, G is the tangential velocity gradient ($G = \frac{\partial v_x}{\partial x}$).

Conservation equation for momentum:

$$\frac{\partial G}{\partial t} + \frac{J}{\rho} + G^2 - \frac{1}{\rho}\frac{\partial}{\partial y}(\mu\frac{\partial G}{\partial y}) + v_y\frac{\partial G}{\partial y} = 0. \tag{2.14}$$

Here J is the tangential pressure gradient ($J = \frac{\partial p}{\partial x}$). It is assumed to be constant throughout the flow field and therefore it is an eigenvalue of the system.

$$\frac{\partial v_y}{\partial t} + \frac{1}{\rho}\frac{\partial p}{\partial y} + \frac{4}{3\rho}\frac{\partial}{\partial y}(\mu G) - \frac{2\mu}{\rho}\frac{\partial G}{\partial y} - \frac{4}{3\rho}\frac{\partial}{\partial y}(\mu\frac{\partial v_y}{\partial y}) + v_y\frac{\partial v_y}{\partial y} = 0. \tag{2.15}$$

Conservation equation for total enthalpy:

$$\frac{\partial T}{\partial t} - \frac{1}{\rho}\frac{\partial p}{\partial t} + v_y(\frac{\partial T}{\partial y}) - \frac{1}{\rho c_p}\frac{\partial}{\partial y}(\lambda\frac{\partial T}{\partial y}) + \frac{1}{\rho c_p}\sum_i c_{p,i} j_{i,y}\frac{\partial T}{\partial y} + \frac{1}{\rho c_p}\sum_i h_i\dot{\omega}_i = 0. \quad (2.16)$$

Conservation equation for species mass:

$$\frac{\partial w_i}{\partial t} + v_y\frac{\partial w_i}{\partial y} - \frac{1}{\rho}\frac{\partial}{\partial y}j_{i,y} = \frac{\dot{\omega}_i}{\rho}. \quad (2.17)$$

The equations are similar to the premixed flame except that the mass flux ρv_y is not constant due to the mass flux in tangential direction. With appropriate boundary conditions, the solution of the above equations provides the flow variables (temperature, concentration, velocity profiles) which can be compared to experimental data.

2.3 Transport parameters and thermodynamic data

It is known from empirical observations that the concentration gradients cause mass transport called diffusion and that temperature gradients causes heat transport called heat conduction. The heat flux is proportional to the temperature gradient given by the Fourier law of heat conduction,

$$j_q = -\lambda\frac{\partial T}{\partial z}, \quad (2.18)$$

here λ is the heat conductivity of the mixture. The heat conductivity in the above equation is calculated from the mixture rule,

$$\lambda = \frac{1}{2}\left[\sum_i x_i\lambda_i + (\sum_i \frac{x_i}{\lambda_i})^{-1}\right], \quad (2.19)$$

where x_i is the mole fraction of the species i and λ_i is the heat conductivity of the species i.

The mass flux j_i of species i can be obtained from the extended form of Fick's law:

$$j_i = \frac{c^2}{\rho} M_i \sum_j M_j D_{ij} \frac{\partial x_j}{\partial z} - \frac{D_i^T}{T} \frac{\partial T}{\partial z}, \tag{2.20}$$

where c is the molar concentration, D_{ij} is multicomponent diffusion coefficient, x_j is mole fraction, D_i^T is thermal diffusion coefficient of species i.

For binary mixtures and for trace species ($w_i \to 0$) the simplified formulation is equivalent to the equation (2.20) given by,

$$j_i = -D_i^M \rho \frac{w_i}{x_i} \frac{\partial x_j}{\partial z} - \frac{D_i^T}{T} \frac{\partial T}{\partial z}, \tag{2.21}$$

where D_i^M denotes the diffusion coefficient for species i into the mixture of all other species with,

$$D_i^M = \frac{1 - w_i}{\sum_{j \neq i} \frac{x_i}{D_i}}. \tag{2.22}$$

The thermodynamic databases (e.g. JANAF-tables [17], Goos-Burcat database [18]) of large number species are tabulated as a function of temperature. The data are stored as polynomials in T. The molar heat capacities is expressed as polynomials of fourth order in T:

$$C_{p,i}(T) = a_1 + a_2 T + a_3 T^2 + a_4 T^3 + a_5 T^4, \tag{2.23}$$

$$H_i(T) = H_{i,298}^0 + \int_{298K}^{T} C_{p,i}(T) dT, \tag{2.24}$$

$$S_i(T, p_i) = S_{i,298}^0 + \int_{298K}^{T} \frac{C_{p,i}(T)}{T} dT + \int_{p^0}^{p_i} -\frac{R}{p M_i} dp. \tag{2.25}$$

To improve the accuracy, two different polynomials are used for low (∼200-1000 K) and high (∼1000-6000 K) temperatures. The switch temperature of the polynomials can

vary with different format of the databases.

2.4 Reaction kinetics

Temperature dependent rate coefficients

A reaction mechanism can consist of numerous elementary reactions which describes the consumption and formation of the reactants and the products. The overall reaction of the methane combustion can be given as

$$CH_4 + 2O_2 \rightarrow CO_2 + 2H_2O. \tag{2.26}$$

However, detailed investigations showed that the products water and carbon dioxide were produced due to many reactive intermediates reactions rather than single collision between the three reacting molecules. These intermediate reactions are elementary reactions which occur on a molecular level. A generalized equation of an elementary reaction r is given by

$$\sum_{s=1}^{S} \nu_{rs}^{(e)} A_s \quad \underset{\rightarrow}{k_r} \quad \sum_{s=1}^{S} \nu_{rs}^{(p)} A_s, \tag{2.27}$$

where k_r is the rate coefficient of the given reaction. It depends strongly on the temperature and is given by the modified Arrhenius equation

$$k_r(T) = A_r T^{n_r} \exp\left(-\frac{E_{a,r}}{RT}\right). \tag{2.28}$$

The rate for the formation of species i, $\dot{\omega}_i$ (in reaction r) is obtained from the sum of rate of all reactions (forward and backward) by

$$\dot{\omega}_i = \sum_{r=1}^{R} \left(\frac{\partial c_i}{\partial t}\right)_{\text{chem},r} = \sum k_r(T)(\nu_{ri}^{(p)} - \nu_{ri}^{(e)}) \prod_{s=1}^{S} c_s^{\nu_{rs}^{(e)}} \tag{2.29}$$

The Arrhenius parameters (A_r, n_r, and $E_{a,r}$) are provided in the reaction mechanism. Together with the ideal gas law, molar masses M_i, and the mass fractions (w_i) resulting from the simulations, concentration of the species c_i are obtained by

$$c_i = c\frac{M}{M_i}w_i \quad \text{and} \quad M = \left(\sum_i^s \frac{w_i}{M_i}\right)^{-1}, \quad c = \frac{p}{RT}. \tag{2.30}$$

The reaction rate of the backward reaction is k_{reverse} is calculated from the thermodynamic equilibrium constant K_c:

$$k_{\text{reverse}} = \frac{k_{\text{forward}}}{K_c}, \tag{2.31}$$

The equilibrium constant K_c can be obtained at standard pressure (p_0) from the standard molar free enthalpy ($\Delta_r G^0$):

$$K_c(T) = \left(\frac{p_0}{RT}\right)^{\nu_{ri}^{(p)}-\nu_{ri}^{(e)}} \exp\left(-\frac{\Delta_r G^0(T)}{RT}\right), \tag{2.32}$$

The standard molar free enthalpy ($\Delta_r G^0$) is calculated from the standard molar reaction enthalpy ($\Delta_r H^0$) and reaction entropy ($\Delta_r S^0$):

$$\Delta_r G^0(T) = \Delta_r H^0(T) - T\Delta_r S^0(T), \tag{2.33}$$

$$\Delta_r H^0(T) = \sum_i^s (\nu_{ri}^{(p)} - \nu_{ri}^{(e)}) H_i^0(T), \tag{2.34}$$

$$\Delta_r S^0(T) = \sum_i^s (\nu_{ri}^{(p)} - \nu_{ri}^{(e)}) S_i^0(T). \tag{2.35}$$

The molar enthalpies (H_i^0) and entropies (S_i^0) of the species are available from the thermodynamics databases [17, 18].

Pressure dependent rate coefficients

The rate coefficients of the reactions, under certain conditions, can also depend on the pressure. They are either dissociation (unimolecular) or recombination (trimolecular)

reactions whose rate increases with increasing pressure. The pressure dependence of the reaction rate can be understood in principle by the Lindemann model [19]. According to this model, such reactions are not elementary, rather they are a sequence of reactions.

Consider an unimolecular reaction AB → A + B [20]. Then according to Lindemann model the reaction splits into two steps:

$$\mathrm{AB} + \mathrm{M} \xrightarrow{k_1} \mathrm{AB}^* + \mathrm{M}, \tag{2.36}$$

$$\mathrm{AB}^* + \mathrm{M} \xrightarrow{k_{-1}} \mathrm{AB} + \mathrm{M}, \tag{2.37}$$

$$\mathrm{AB}^* \xrightarrow{k_2} \mathrm{A} + \mathrm{B}. \tag{2.38}$$

In the first step, collision occurs between the reactant AB and colliding molecule M. In this process, energy of M is transfered to AB and it reaches a state (AB*) above the energy barrier (2.36). This energized state AB* rearranges to form the product (2.38) or deactivates (2.37). If it is assumed that the steady-state condition is achieved in negligible time compared to the total reaction time then the unimolecular rate coefficient k_{uni} can be derived as follows:

$$\frac{\mathrm{d}[\mathrm{AB}^*]_{\mathrm{ss}}}{\mathrm{d}t} = k_1[\mathrm{M}][\mathrm{AB}] - (k_{-1}[\mathrm{M}] + k_2)[\mathrm{AB}^*]_{\mathrm{ss}} = 0 \tag{2.39}$$

Here subscript ss refers to steady state.

$$\frac{\mathrm{d}[\mathrm{A}]}{\mathrm{d}t} = \frac{\mathrm{d}[\mathrm{B}]}{\mathrm{d}t} = k_2[\mathrm{AB}^*] = k_2 \frac{k_1[\mathrm{AB}][\mathrm{M}]}{k_{-1}[\mathrm{M}] + k_2} = k_{\mathrm{uni}}[\mathrm{AB}] \tag{2.40}$$

$$k_{\mathrm{uni}} = \frac{k_1 k_2[\mathrm{M}]}{k_{-1}[\mathrm{M}] + k_2} \tag{2.41}$$

In low pressure limit ([M]→0) and high pressure limit ([M]→ ∞) these rate coefficients can be given by

$$[\mathrm{M}] \to 0, \quad k_{uni} \to k_{uni,0} \equiv k_0 = k_1[\mathrm{M}] \tag{2.42}$$

$$[\mathrm{M}] \to \infty, \quad k_{uni} \to k_{uni,\infty} \equiv k_\infty = \frac{k_1 k_2}{k_{-1}} \tag{2.43}$$

This is shown in the Fig. 2.3 where at low pressures the rate coefficient is proportional to [M] and a linear dependence results. At high pressures, the rate coefficient becomes independent of the pressure. The linear dependence at low pressures departs at certain pressure and it *falls off* to the high pressure limit. This transition region in which the k_{uni} switches from low pressure to high pressure regime is called the fall-off region. The

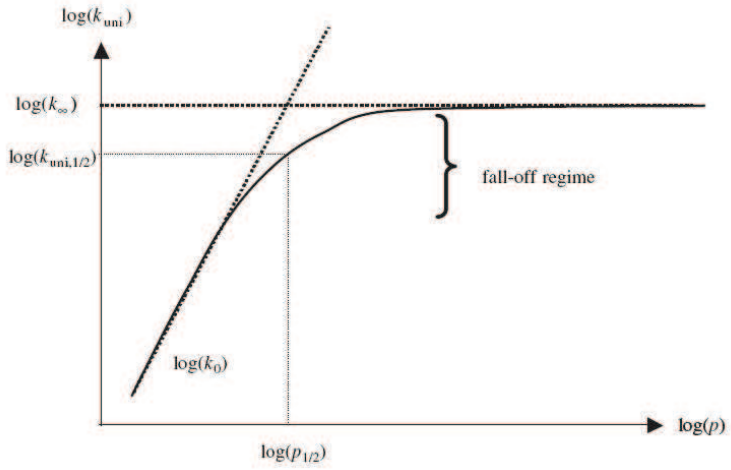

Figure 2.3: A fall-off plot for a unimolecular rate coefficient as function of pressure [20].

unimolecular rate coefficient is usually expressed in terms of the reduced pressure p_r:

$$k = k_{uni} = k_\infty(\frac{p_r}{1+p_r}), \qquad \text{where,} \quad p_r = \frac{k_0[M]}{k_\infty} \quad . \tag{2.44}$$

In practice, the equation (2.44) does not describe the fall-off curve completely due to additional complexity of collisional deactivation and activation, energy and angular momentum dependences of association and dissociation steps. Therefore, the equation (2.44) is modified by a broadening factor F,

$$k = k_{uni} = k_\infty(\frac{p_r}{1+p_r})F. \tag{2.45}$$

If F in above equation (2.44) is equal to one then it is the Lindemann form. An expression better fitted to experimental findings is given by Troe [21],

$$\log F = [1 + [\frac{\log P_r + c}{n - d(\log P_r + c)}]^2]^{-1} \log F_{cent} \tag{2.46}$$

with $c = -0.4 - 0.67\log F_{cent}$, $n = 0.75 - 1.27\log F_{cent}$, $d = 0.14$, and

$$F_{cent} = (1-\alpha)\exp(-T/T^{***}) + \alpha\exp(-T/T^{*}) + \exp(-T^{**}/T). \tag{2.47}$$

In the Troe pressure-dependent reaction [21], in addition to the k_∞ and k_0 rate parameters, these four parameters $\alpha, T^{***}, T^{**}, T^{*}$ are provided as input.

2.5 Chemiluminescent kinetics

In the combustion zone, the electronically excited species are formed from the energetic intermediate ground state species. These species formed are highly reactive. The lifetime of the formed excited species is short and they return to the ground state by emitting their energy which is immediately removed by passing into lower state (i.e. its ground state or a lower excited state). This emitted radiation in form of light (hv) is called luminescence. The luminescence arising from chemical excitation is called chemiluminescence.

In chemiluminescence, light is emitted by molecules returning to the ground state which were excited chemically rather than thermally. The chemiluminescence signal shows strong dependence on the chemical composition and weak dependence on the temperature [22]. The strongest chemiluminescent intensities in hydrocarbon flames are from OH* and CH* whereas C_2* has a relatively weak intensity. The OH* emission is found at 309 nm, CH* emission is found at 431 nm CH($A^2\Delta - X^2\Pi$), 390 nm CH($B^2\Sigma^- - X^2\Pi$), and at 314 nm CH($C^2\Delta - X^2\Pi$) in flame spectra. Among the three available states in CH*, the first two are the strongest. The Swan bands of C_2* are found between 436 - 564 nm. Since in chemiluminescence the excited species are due to chemical excitation, their formation does not depend on their ground state (which is the case for thermal excitation).

In addition to this, the excited molecules can undergo collisional quenching. In collisions with other molecules the electronically excited molecule may pass into a lower electronic state - which is often the ground state. This radiationless decay process is more common where the excess energy is transferred into the vibration, rotation, and

translation of surrounding molecules. This thermal degradation converts the excitation energy completely into thermal motion of particles, molecules or atoms i.e. to heat. Collisional quenching is either reactive or non-reactive in nature. When the excited species transfers its energy to the colliding molecule and comes to its ground state, this is called non-reactive collisional quenching. An excited molecule may also take part in chemical reactions [23]. When the energy transfer to the collider results in two different products (due to chemical reaction), this is called reactive collisional quenching. The spatial distribution of spontaneous emission depends on the orientation of the excited molecules and on the symmetry properties of the excited state. Since this processes involve collisions, their rates depend on the frequency of collisions and therefore on the availability of the colliding molecules. In the gas phase this process may occur within 10^{-8} s at normal pressure [23]. The probability that an excited molecule in the level E_i makes a transition to lower level E_k by spontaneous emission of a fluorescence quantum $h\nu_{ik}$ = E_i - E_k is given by Einstein coefficient A_{ik}, as shown in Fig. 2.4.

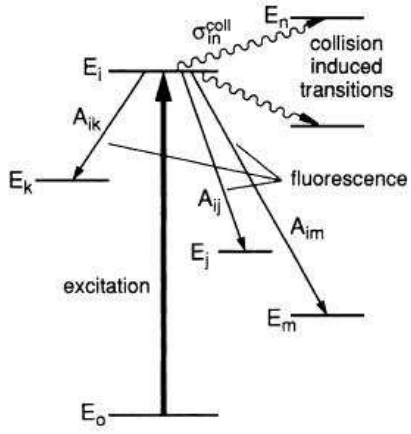

Figure 2.4: Radiative and collision induced decay channels of an excited level [24].

The quantitative analysis of the flame spectra would require, the relationship between the measured intensity and the excited state concentration, to be determined. Assume that the molecule has lower energy level E_1 and higher energy level E_2, as shown in Fig. 2.5. The excited molecule in the higher E_2 state may spontaneously convert its excitation energy by emitting photon ($h\nu$), where $h\nu$ = E_2 - E_1. The spontaneous emission rate from higher to lower level, i.e. the probability that a photon is emitted by a molecule, depends on the structure of the molecule and the selected transition. The spontaneous

emission rate is given by the Einstein coefficient of spontaneous emission A_{21} [24]. The

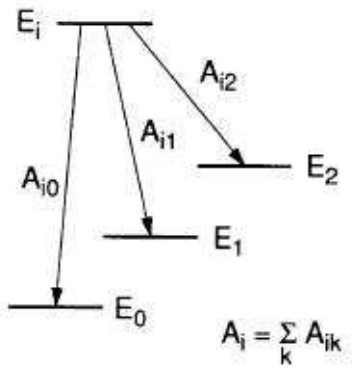

Figure 2.5: Radiative decay from a higher energy level E_i to lower levels [24].

measured chemiluminescent intensity I_i for species i is given by [25],

$$I_i = y_i c_i^*. \tag{2.48}$$

here, c_i^* is the concentration of the excited state molecule. y_i is the fluorescence yield which gives probability that an excited molecule will emit the photon. For a given transition from an excited to the lower level, it is given by the ratio of number density of excited state molecule that emits photons to the total number density (i.e. radiation + quenching rate)

$$y_i = A_{21}/(A_{21} + Q_{21}), \tag{2.49}$$

where the collisional quenching rate is defined as,

$$Q_{21} = \sum_j c_j k_j. \tag{2.50}$$

Here, the c_j is the concentration of the colliding molecules and k_j is the rate coefficients of the quenching reactions.

Therefore, by using the equation (2.48), the concentration of the excited species can be obtained from the measured intensities.

2.6 Analysis of the reaction kinetics

It is well-known that the reaction kinetics mechanism of the smallest hydrocarbon fuel (CH_4) would require the mechanism consisting of about 11 species and 58 elementary reactions. For higher hydrocarbons, several thousands of reaction would be required. The interaction of these reactions governs the combustion process. However, among them there are only few reactions which determine the rate of the overall process (called rate-limiting reactions). Therefore it is advantageous to know the set of reactions whose knowledge is sufficient to governs the entire combustion process.

The two major mechanism analysis methods performed are sensitivity analysis and reaction flow analysis. Through the sensitivity analysis it is possible to determine whether the reaction is rate limiting or not. This helps in understanding the relative importance of reaction as one requires a highly accurate rate data for the rate limiting reaction. On other hand, the accuracy of the rate data does not affect the simulation results of the non sensitive reactions. The reaction flow analysis determines the characteristic reaction paths thereby providing information on the formation and consumption pathways of a given species.

In a sensitivity analysis, the rate coefficients of the chemical reactions are considered as parameters. In a system with R reactions and S species, the change in concentration of species i is written as,

$$\frac{dc_i}{dt} = F_i(c_1, \ldots, c_s; k_1, \ldots, k_r), \tag{2.51}$$

where, $\quad i = 1, 2, \ldots, S \quad$ and $\quad c_i(t = t_0) = c_i^0$.

Here, c_i (concentration of species i) is the dependent variable and the time t is independent variable. c_i^0 is the initial condition at time t_0. The dependence of the solution c_i on the parameter k_r is called sensitivity. The absolute sensitivity is given by,

$$E_{i,r} = \frac{\partial c_i}{\partial k_r} \tag{2.52}$$

and the relative sensitivity is given by

$$E_{i,r}^{(rel)} = \frac{k_r}{c_i}\frac{\partial c_i}{\partial k_r} = \frac{\partial ln c_i}{\partial ln k_r}. \tag{2.53}$$

For given ±x% change in k_r, the sensitivity analysis gives information on changes in concentration of the given species. A high sensitivity indicates that the reaction is rate limiting. The analysis can be performed either globally or locally. The global sensitivity analysis considers the overall formation and consumption during the combustion process. The resulting analysis is integrated over the whole reaction time (for homogeneous time dependent system) and the results for stationary flames are integrated over the reaction zone. The local reaction flow analysis considers the formation and consumption of species locally, i.e. at specific times in time-dependent problem (ignition processes) or at specific locations in steady state processes (flat flame).

The reaction flow analysis gives information on the relative rate of formation and consumption of a species. From this analysis, one can draw the entire reaction pathway for the consumption and formation of a given species. The integral reaction flow analysis considers the overall formation and consumption during the combustion process. In homogeneous systems the results are integrated over the reaction time whereas in stationary flames they are integrated over the reaction zone. The local reaction flow analysis considers the formation and consumption of species at specific times (in homogeneous process) or at specific locations (flat flames). The reaction is considered to be unimportant if the formation (or consumption) of given species is below certain limit (e.g., 1%).

3 Kinetics Mechanism of C_1 to C_4 Hydrocarbon Oxidation

The concentration of chemiluminating species is low compared to the concentration of ground state species. Therefore, it is seen that their prediction depends on the species that are the direct precursors responsible for their formation. These intermediates such as CH, C_2H, C_2, and $^1CH_2$ are not directly important for the global validation (such as ignition delay time, flame velocity) of the basic hydrocarbon oxidation mechanism. Therefore, before developing the mechanism for the excited species, it is important to have a good prediction of such chemiluminescence precursor species.

The underlying mechanism originates from the dissertation of Heghes [26]. The C_1 to C_4 hydrocarbon mechanism in [26] is derived to model basic fuels at non-sooting conditions. This mechanism is modified in the present work with focus on the intermediates such as CH, C_2H, C_2 and is discussed in this chapter. The complete description of oxidation of hydrocarbons in the low and high temperature range requires incorporation of RO_2, RO_2H, aldehyde species, and radicals along with single, double and triple bond RH.

Initially H, O, OH radicals are produced by chain branching steps of O_2-H_2-reactions (oxy-hydrogen reactions). The hydrocarbon fuel molecules are attached by these radicals to form alkyl radicals (Fig. 3.1). These alkyls further decompose to smaller alkyls. In addition to the CH_3 decomposition path there is a competing recombination path which forms C_2H_6. This recombination path is important in the rich flame condition. The CH_3/C_2H_5 oxidation is rate limiting step. Similarly, the C_3/C_4 hydrocarbons decomposes to CH_4 and C_2H_5 and follows the C_1/C_2 chemistry pathways as shown in Fig. 3.1

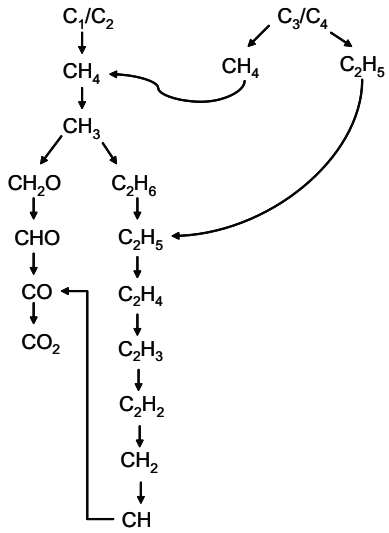

Figure 3.1: C_1 to C_4 hydrocarbon decomposition scheme.

3.1 H_2-O_2 oxidation

The mechanism of H_2-O_2 involves important chain branching steps forming H, O, and OH radicals. The reaction H + O_2 → OH + O (R1) is the most important chain branching reaction at high temperature and low pressures. Here, the number (R1) refers to the reaction number presented in mechanism in Appendix. A pressure- and temperature-dependent reaction H + O_2 + M → OH + O + M (R8) is competing with reaction (R1) and has chain terminating character, due to the relatively nonreactive nature of the HO_2 radical formed. At low pressures the main branching reactions H+O_2 (R1), O+H_2 (R2) and OH+H_2 (R3) are important. However, as the pressure increases leading to the second explosion limit region, the reaction rate is controlled by the reactions involving HO_2.

The kinetics scheme discussed in [26] has been modified in the current work, which is presented in Appendix. The underlying mechanism originating from Heghes 2007 [26] has considered reaction rate of H + O_2 + M = HO_2 + M (R8) as a sum of two Arrhenius expression. The present study considers only one reaction rate (R8) as shown in Appendix. The reaction H + O_2 = OH + O (R1) is the basic chain branching reaction at high temperature and flame propagation is highly sensitive to this reaction. Reaction (R8), thus, competes with reaction (R1) at the given temperature and pressure conditions. The ignition delay time measured from the onset of OH* profile is presented

in Fig. 3.2. The measurements are shown for lean and stoichiometric H_2/2-O_2 mixtures

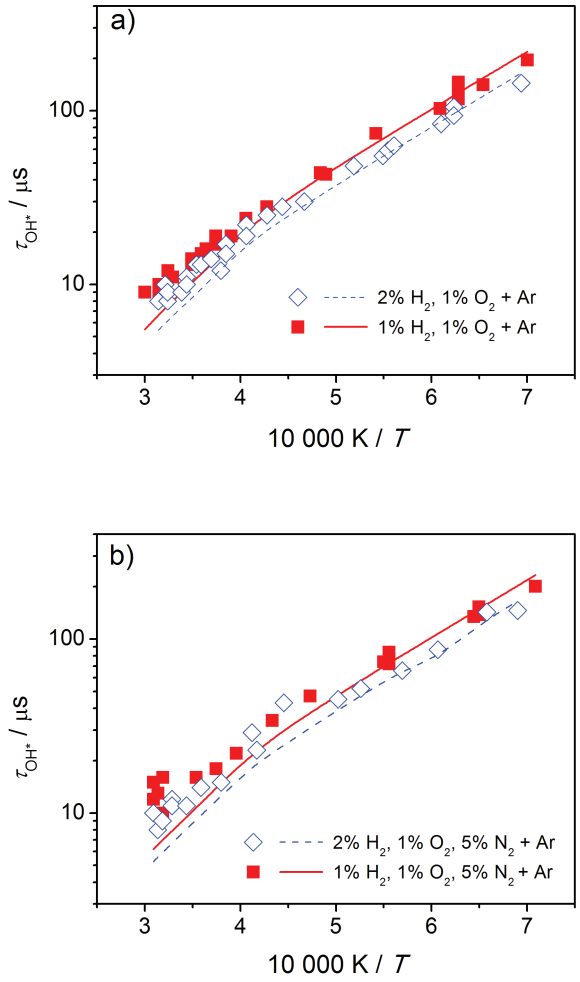

Figure 3.2: Ignition delay time with respect to the OH* concentration for lean and stoichiometric H_2/O_2 mixture with Ar (a) and Ar+N_2 (b) dilution, Symbols: shock-tube experiments, lines: simulations [27].

diluted in Ar and Ar+N_2. The ignition delay time of 1% H_2, 2% O_2 in argon at 1 bar from the shock-tube experiments of [28] measured near second explosion limit are presented in Fig. 3.3. The ignition delay time at higher temperatures are presented later in Chapter 5. Figure 3.4 presents various reported values of the laminar flame velocity measurements (recent and older) at 1 bar and 298 K initial temperature. Their references are as presented in Fig. 19 of [27]. The results from ignition delay time and flame velocity are in good agreement with the measurements.

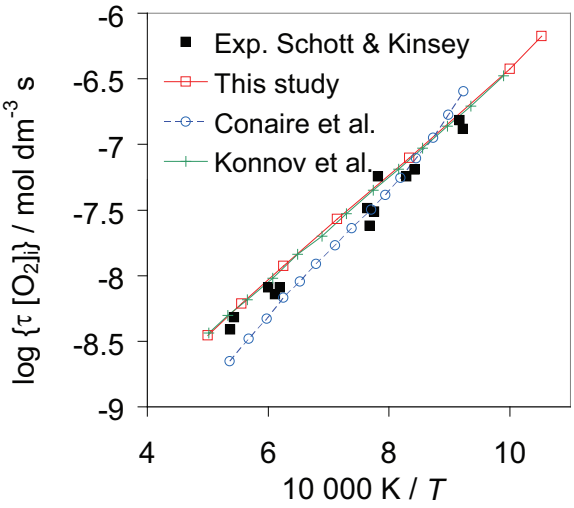

Figure 3.3: Ignition delay time of 1% H_2/2% O_2 mixture in argon at 1 bar. Symbols: experiments from Schott and Kinsey [28], lines: simulations with different mechanisms from literature (given in Fig. 17 of [27]).

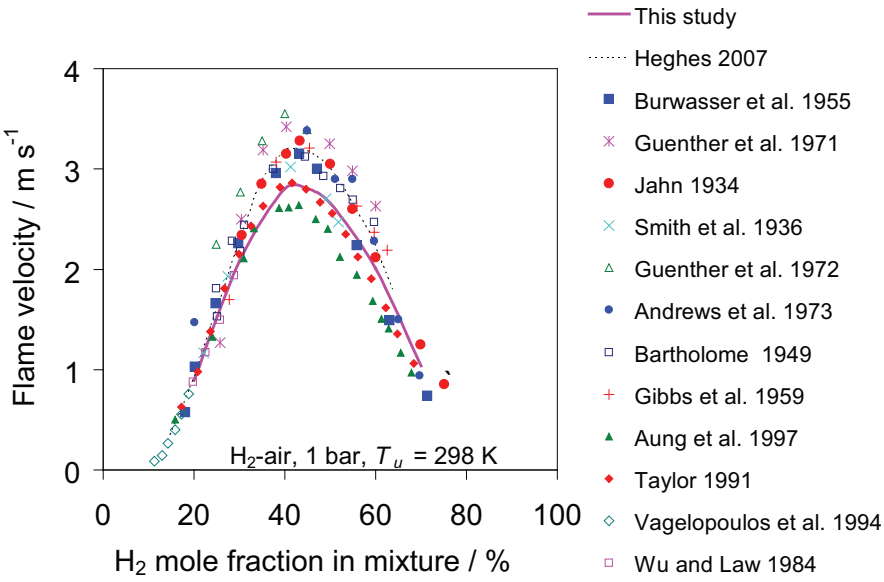

Figure 3.4: Measured laminar flame velocity of H_2/air mixtures as a function of the H_2 mole fraction at 1 bar and 298 K initial temperature. The flame velocities correspond to the one which are corrected for stretch effects: Aung et al. [29], Taylor [30], Vagelopoulos [31] and Wu and Law [32]. The velocities from the remaining authors are not corrected for the stretch effects and are as reported in Warnatz [33].

Absolute concentrations measured in hydrogen-air flame by Smith et al. [34] provide stringent test on the hydrogen sub-mechanism. A one-dimensional simulation of the premixed burner-stabilized laminar flame is performed to obtain the concentrations of major radicals and stables species measured in [34] by molecular beam mass spectroscopy. The flame is fuel rich with $\phi = 1.91$ at 0.05 bar. The results from the simulation show that the H and O concentrations (at OH* peak), important for OH* formation, are well predicted with deviations of +2% and +20% compared to the measurements. The measurement error of these atoms is estimated to be 10%. This comparison is intended to provide an understanding of the relevance of H and O concentrations for the prediction of OH* in flames. As shown in Fig. 3.5, other radicals and stable species such are H_2, H_2O, OH, and O_2 are also in good agreement with the measurements.

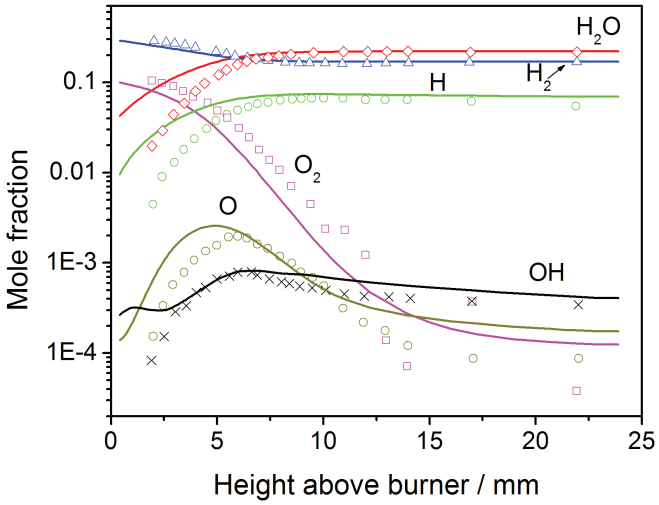

Figure 3.5: Comparison of absolute concentrations for the major radicals and stable species in a rich $H_2/O_2/Ar$ laminar premixed flame at 0.05 bar. Symbols: experiments [35], line: simulation.

3.2 C_1-C_2 oxidation

The primary hydrocarbon oxidation product CO oxidizes to CO_2 in a subsequent slow secondary reaction CO + OH $\rightarrow$ CO_2 + H. The reverse of this reaction (CO_2 + H $\rightarrow$

CO + OH) is important to establish water gas equilibrium [36]. CO is mainly formed in the reaction CHO + M → CO + H + M.

3.2.1 C_1 chemistry

The smallest hydrocarbon fuel methane is widely studied in combustion as it is an important fuel itself but is also produced during the oxidation of most of the hydrocarbons. In the oxidation of CH_4, the fuel is attacked by H, O, OH radicals which forms CH_3. The reaction $CH_4 + M \rightarrow CH_3 + H + M$ initiates the thermal decomposition at high temperature ignition forming CH_3:

$$(R94) : CH_4 + H \rightarrow CH_3 + H_2,$$

$$(R95) : CH_4 + O \rightarrow CH_3 + OH,$$

$$(R96) : CH_4 + OH \rightarrow CH_3 + H_2O.$$

The CH_3 thus formed reacts with O to form formaldehyde (CH_2O) which further reacts rapidly to generate CHO:

$$(R66) : CH_3 + O \rightarrow CH_2O + H,$$

$$(R54) : CH_2O + H \rightarrow CHO + H_2,$$

$$(R55) : CH_2O + O \rightarrow CHO + OH,$$

$$(R56) : CH_2O + OH \rightarrow CHO + H_2O.$$

The CHO is thermally decomposed to CO. The methane oxidation is completed by the oxidation of CO to CO_2:

$$(R34) : CHO + M \rightarrow H + CO + M,$$

$$(R35) : CHO + H \rightarrow H_2 + CO.$$

The ignition delay time of $CH_4/O_2/Ar$ mixtures measured at atmospheric pressure (Fig. 3.6) and at high pressures (Fig. 3.7) are found to be in very good agreement with the measurements. The ignition delay times is sensitive to the chain branching reaction

(R1). The simulations for the shock-tube experiments were obtained at atmospheric pressures [37] and at high pressures of 18 and 60 bar [38].

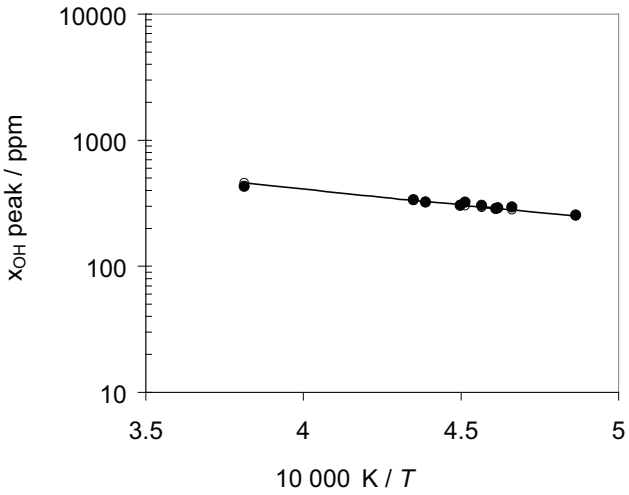

Figure 3.6: Comparison of peak OH concentrations for $CH_4/O_2/Ar$ stoichiometric mixture at 1 bar. Symbol: shock-tube experiment [37], line: simulation from present work.

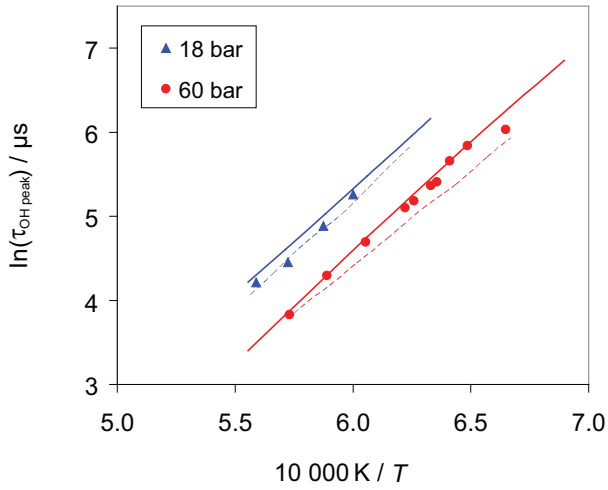

Figure 3.7: Ignition delay time determined from peak OH concentration for 0.5% CH_4, 2.5% O_2 with diluent argon (18 bar) and nitrogen (60 bar). Symbols: experiment [38], continuous line: simulation from present work, dashed line: simulation with GRI-mech 3.0 [39].

The measurement of peak OH concentrations for $CH_4/O_2/Ar$ stoichiometric mixture at 1 bar pressure is obtained in shock-tube experiment [37]. As shown in Fig. 3.6 the simulated OH peak concentrations are in very good agreement with the measurements. At high pressures (Fig. 3.7), Petersen et al. [38] measured ignition delay time based on the OH peak time for the mixture of 0.5% CH_4-2.5% O_2 with argon (18 bar) and nitrogen (60 bar) as diluent. The simulated ignition delay times, as shown in Fig. 3.7, are in very good agreement with the measurements at both pressures. The ignition delay time obtained by using the GRI-mech 3.0 [39] slightly underpredicts the measurement at 60 bar.

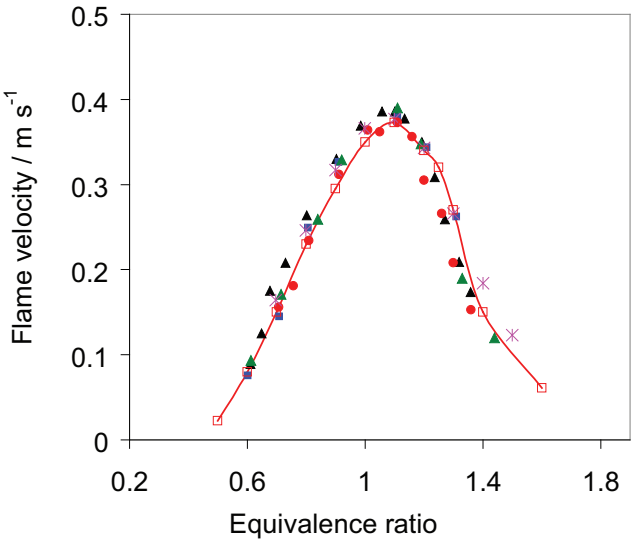

Figure 3.8: Laminar flame velocity of $CH_4/O_2/N_2$ mixture at 298 K initial temperature and at 1 bar. Line: simulation from present work, symbols: experiments from [26, 31].

The burning of the premixed laminar flat flames is characterized by the laminar flame velocity. The flame velocity of the reacting mixture depends on the fuel stoichiometry, the pressure and the initial temperature. It is seen in sensitivity analysis that the reaction (R1) is the most sensitive reaction independent of the fuel stoichiometry [13]. In addition to this, a chain terminating reaction (R8) has a large negative sensitivity as it reduces the H atoms in the mixture. The reaction $CO + OH \rightarrow CO_2 + H$ (R22) which governs the heat release is also a rate limiting reaction. Figure 3.8 presents flame velocity of $CH_4/O_2/N_2$ at 1 bar pressure and 298 K initial temperature. The experimental points are obtained from the studies of [26,31]. A good agreement between simulated velocities

and experimental velocities is obtained at different equivalence ratios.

3.2.2 C_2 chemistry

The simple scheme of decomposition of CH_4 is complicated by the recombination of CH_3 in the reaction

$$(R173) : CH_3 + CH_3 \rightarrow C_2H_5 + H.$$

This recombination path consumes about 30% CH_3 in stoichiometric CH_4-air flames which increases to 80% in rich flame. Thus from stoichiometric to rich conditions, knowledge on the combustion of C_2-hydrocarbons is getting more and more important in addition to the C_1-hydrocarbons chemistry.

The recombination path is dominated by reaction,

$$(R76) : CH_3 + CH_3 + M \rightarrow C_2H_6 + M,$$

where the C_2H_6 formed is further attacked by H, O, and OH radicals to form C_2H_5. There are many competing reactions consuming C_2H_5. In one channel it oxidizes to CH_2CHO and CH_2CO, and finally forms CH_3. The major channel is the reaction of C_2H_5 with O_2 and thermal decomposition forming C_2H_4:

$$(R176) : C_2H_5 + O_2 \rightarrow C_2H_4 + HO_2,$$

$$(R172) : C_2H_5 + M \rightarrow C_2H_4 + H + M.$$

In a less important channel, C_2H_5 reacts with H atoms to form CH_3 again:

$$(R173) : C_2H_5 + H \rightarrow CH_3 + CH_3.$$

The C_2H_4 formed in above channel oxidizes with H, OH and forms mainly CH_3 and CHO:

$$(R157) : C_2H_4 + OH \rightarrow C_2H_3 + H_2O,$$

$$(R155) : C_2H_4 + O \rightarrow CH_3 + CHO.$$

In addition, C_2H_4 reacts back to C_2H_5 and another channel forms C_2H_3 (about 55% in stoichiometric CH_4 flames).

$$(R152) : C_2H_4 + H + M \rightarrow C_2H_5 + M,$$

$$(R153) : C_2H_4 + H \rightarrow C_2H_3 + H_2.$$

The C_2H_3 formed from C_2H_4 is converted mainly to C_2H_2 by thermal decomposition and by reaction with H atoms:

$$(R139) : C_2H_3 + M \rightarrow C_2H_2 + H + M,$$

$$(R140) : C_2H_3 + H \rightarrow C_2H_2 + H_2.$$

3.2.3 C_2H_2 chemistry

The C_2H_2 plays an important role under fuel rich conditions. It is an important precursor for the formation and growth of soot. In addition to this, the acetylene chemistry is also important for the present work as the direct precursors to the excited species formation (e.g. CH, C_2H, C_2) are formed from acetylene. The C_2H_2 formed in the recombination channel is consumed by the attack of O and OH atoms:

$$(R129) : C_2H_2 + OH \rightarrow C_2H + H_2O.$$

$$(R128) : C_2H_2 + O \rightarrow HCCO + H,$$

$$(R127) : C_2H_2 + O \rightarrow {}^3CH_2 + CO,$$

As discussed in [26], the channel forming C_2H is the dominant reaction (65% lean-, 70% rich- methane/air flame) followed by reaction forming HCCO (27% lean-, 22% rich-methane/air flame) whereas the third channel which forms CH_2 in the triplet state is a minor channel (less than 10%). Among these C_2H_2 consumption reactions, the reaction of $C_2H_2 + O_2 \rightarrow HCCO + OH$ (R128) is found very important for the ignition delay time of acetylene mixtures. Whereas the flame speed of such mixtures is sensitive to the rate of $C_2H_2 + OH \rightarrow C_2H + H_2O$ (R129).

The mechanism presented in [26] is referred to hereafter as original mechanism whereas

the modifications made to original mechanism is referred to as modified mechanism.

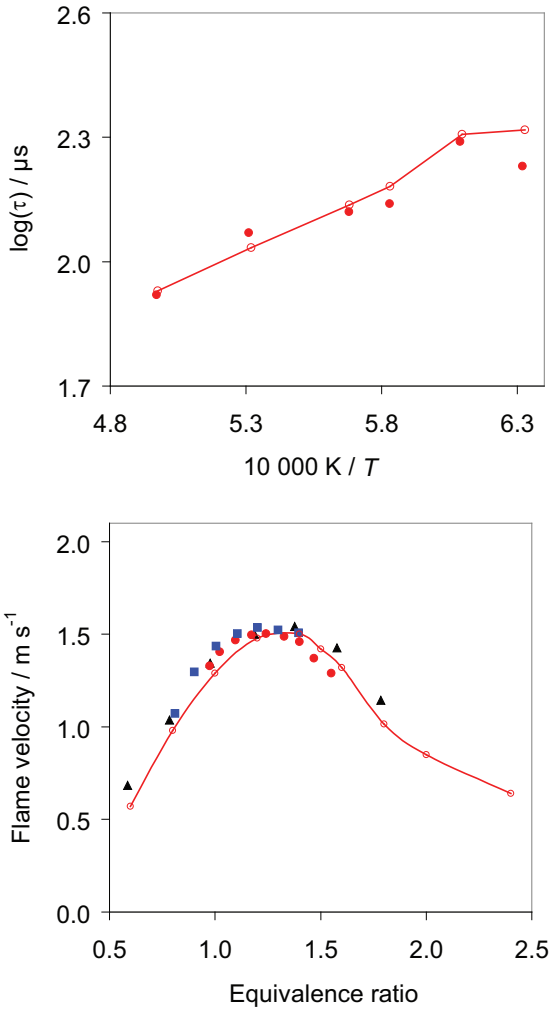

Figure 3.9: (a) Ignition delay time for a 0.5%C_2H_2/0.8%O_2 mixture diluted in argon, pressure in the range 0.64-0.78 bar. The ignition delay time is derived at the time when the concentration of [CO]+[CO_2] attains its 10% value. Symbols: experiments [40], line: simulation. (b) Comparison of measured and simulated laminar flame velocity of $C_2H_2/O_2/N_2$ mixtures at different stoichiometry. The initial temperature of the mixture is 298 K and the pressure 1 bar. Line: simulation, symbols: experiments from [41].

The original mechanism failed to predict the experimental ignition delay times of C_2H_2. The simulated ignition delay times were about two orders of magnitude lower than the measurements. Therefore, the C_2H_2 formation and consumption paths were reinvesti-

gated. While modifying the mechanism one has to be careful as the reaction which influences the ignition delay time has also influence on the flame velocity. In order to match the measured ignition delay time it would require to decrease the rate of reaction (R128). The rate of this reaction is not well studied and no recommendation is made in the database by Baulch et al. [42]. Therefore a factor of 4 slower rate recommended by Miller et al. [43] which is equal to $k_{(\mathrm{R128})} = 5.0{\times}10^7 T^{1.5}\exp(\text{-}126\ \mathrm{kJ\ mol^{-1}}/RT)\ \mathrm{cm^{-3}\ mol^{-1}\ s^{-1}}$ is taken into account. Also the reaction rate of (R129) has been modified within the available limit of k given in [42]. Based on these changes, the ignition delay time is decreased compared to the earlier predictions in [26] and excellent agreement is seen with the measurement as is shown in Fig. 3.9a. The flame velocities of acetylene-air mixtures are also well reproduced as given in Fig. 3.9b.

Acetylene chemistry plays important role in fuel rich conditions where soot and poly-cyclic aromatic hydrocarbons (PAH) is formed. In context of present work, it is an important precursor leading to all excited species formation (see Fig. 3.10). Therefore it is important to validate the mechanism for its prediction of acetylene concentration in flames.

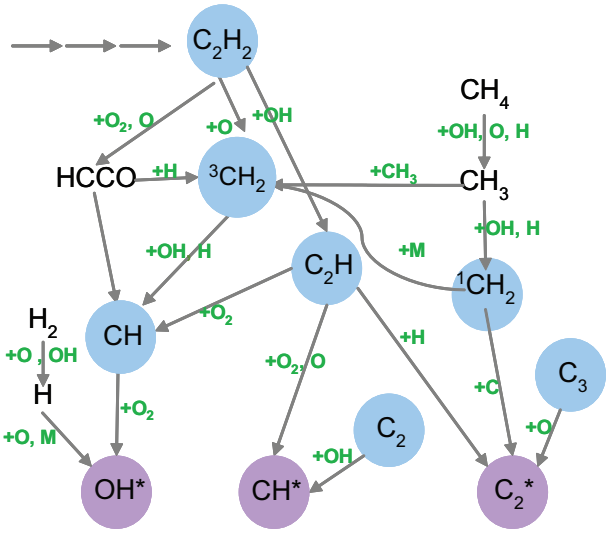

Figure 3.10: Reaction scheme of chemiluminescence species formation from its major precursor C_2H_2.

The measurement of C_2H_2 concentration has been carried out in diffusion flame conditions by Wagner et al. [44]. The experiments are performed in Tsuji-type burner [16] where the fuel exits through a porous cylinder into a vertically upward directed air flow.

Table 3.1: Operating conditions of CH_4-air diffusion flame.

a / s^{-1}	v_{air} / m s^{-1}	v_{fuel} / m s^{-1}	T_{fuel} / K
100	-1.0	0.18	473
150	-1.5	0.21	562
200	-2.0	0.25	651

The measured flow velocity at the fuel-side exit and the strain rate at the air-side are input parameters to the calculations. The experimental conditions of the burner operation are presented in the Table 3.1.

The quantitative experimental profile of C_2H_2 are measured using *Tunable Diode Laser Absorption Spectroscopy* (TDLAS) [45]. The C_2H_2 mole fractions in laminar diffusion flames are measured at different strain rates. In addition to C_2H_2 mole fractions, gas phase temperatures are also recorded using *Coherent Antistokes Raman Spectroscopy* (CARS). The spatial profiles of acetylene and the gas phase temperature in CH_4-air counter-flow diffusion flames are obtained at varying strain rates a of 100, 150, 200, and 300 s^{-1}. The experimental conditions are summarized in Table 3.1. As the flames are measured with air from the atmosphere, there exists about 1% relative humidity in air.

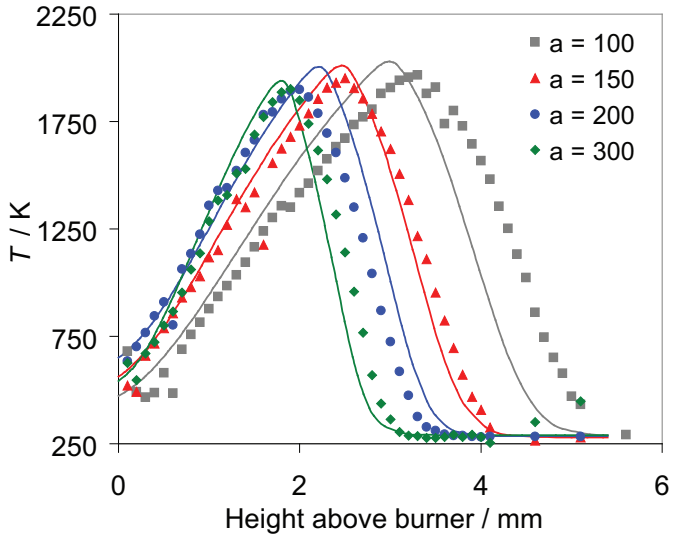

Figure 3.11: Comparison of experimental (symbol) and simulated (line) temperature profile for CH_4-air non-premixed flame with a = 100, 150, 200, and 300 s^{-1}.

The presence of humidity has a small influence, e.g. when the calculations are performed with 1% relative humidity in air, the peak temperatures are about 18 K (at 100 s^{-1} strain rate) lower than those calculated with dry air. The temperature calculated with 1% relative humidity in air are closer to the measurements. Also, the calculations do not account for the heat losses to the surroundings and therefore there is about 60 K difference in measured and calculated peak temperature.

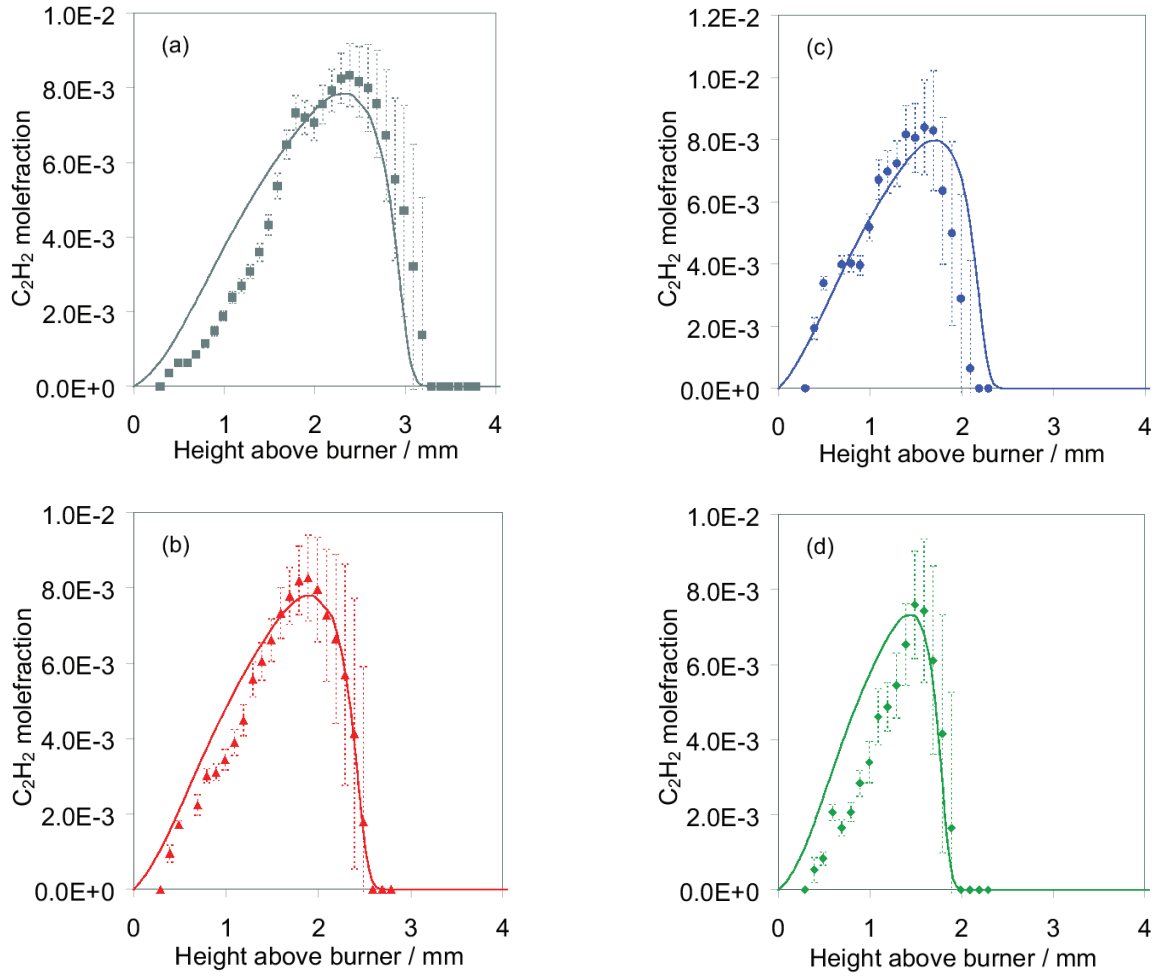

Figure 3.12: Comparison of experimental (symbol) and simulated (line) C_2H_2 mole fractions for CH_4-air non-premixed flame with (a) a = 100 s^{-1}, (b) a = 150 s^{-1}, (c) a = 200 s^{-1}, and (d) a = 300 s^{-1}.

Figure 3.11 shows the comparison of experimental and calculated temperature profiles at different stain rates. The simulated temperature profiles are in good agreement with the measurements. At strain rate 100, the temperature decrease is faster compared to the measurements. Since the flow measurements at exit conditions are difficult, there is

an error of about ±0.5% for the fuel flows and about a ±2.0% (a = 100) to ±0.7% (a = 300) error in air velocity measurement. This errors leads to a change in position of the flame by which the discrepancy in the position of the measured and calculated profiles is reduced. The temperatures at other strain rates are in very good agreement with the measurements.

The measured and calculated C_2H_2 mole fractions are compared in the Fig. 3.12. The error bars on measured C_2H_2 profile accounts for the uncertainty of the absorption line fit. Therefore the resulting mole fraction is divided by the signal to noise ratio (SNR) between the extracted absorption line area and residual noise on the signal [45]. The measured and simulated C_2H_2 mole fractions are in excellent agreement at all three strain rates.

3.2.4 Modifying important intermediate concentration

In addition to this, for the development of chemiluminescence mechanism, it is important to have better prediction of certain intermediate species such as CH, C_2H which are direct precursors of the excited states formation. The prediction of these species is not a criterion for the mechanism validations presented in [26], but it is important in the context of the present work and therefore a further modification of the original mechanism is carried out. The absolute CH concentrations in their ground states are studied in a series of hydrocarbon (methane-, ethane-, and ethylene- air) premixed laminar flames by Smith et al. [46]. Among other recent works, Thoman and McIlroy [47] measure absolute CH concentration in stoichiometric and rich methane/oxygen/argon-flame via cavity ringdown spectroscopy. The mechanism discussed in [26] predicts the CH concentrations about 4 times higher than the measurements. Therefore, it is necessary to investigate the CH formation and consumption pathways that lead to such overprediction. The main channel to CH formation is via C_2H or HCCO decomposition whereas the $^3CH_2$ is the minor channel to CH formation as shown in Fig. 3.13. The simulated concentration of C_2H is in good agreement with the measurement in Bastin et al. [48].

The following changes are made to the mechanism from [26] to achieve better prediction of C_2H_2 ignition delay time and better prediction of CH concentrations in flames.

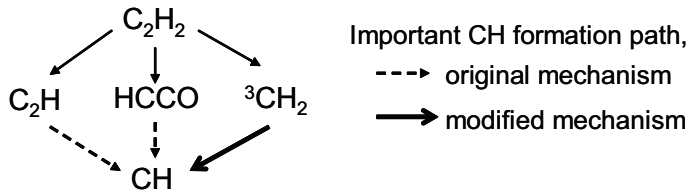

Figure 3.13: Schematic of the formation pathways of CH. Dotted line: in mechanism from [26], continuous line: modified path in present work.

1. It has been reported in [49–51], that the dominant path to CH is via $^3CH_2$. The formation of CH species are linked to the C_2H_2 decomposition pathway. In the original mechanism [26] the CH formation path is dominated via the C_2H path as a high reaction rate is selected for the reaction $C_2H + O_2 \rightarrow CO_2 + CH$ (R119).

   The reaction of C_2H with O_2 leads to four branching reactions (R117)-(R120) forming mainly CO, CO_2, CH, and HCCO as reaction products. A recommended branching ratio of CO:CO_2 in [42] is 9:1, which implies that the important channels lead to CO. Therefore, the reaction CO_2 + CH (R119) channel leads to only 10% of the total rate which is considered the major channel in the original mechanism of [26]. This newly incorporated rate leads to the reduction of CH-concentrations in flames. An additional modification is made for the rate of reaction CH + H $\rightarrow$ C + H_2 (R25) which is increased by factor of four in the recommended limit of log $k = +0.6$ [42]:

$$\begin{aligned} (\text{R117}) - (\text{R120}) : C_2H + O_2 &\rightarrow CHO + CO, \\ &\rightarrow H + CO + CO, \\ &\rightarrow CO_2 + CH, \\ &\rightarrow HCCO + O. \end{aligned}$$

2. The second change made is the rate of the important reactions C_2H_2 + H $\rightarrow$ C_2H + H_2 (R126) and $C_2H_2 + O_2 \rightarrow$ HCCO + OH (R130) which improves the prediction of C_2H_2-O_2 atmospheric ignition delay times (T = 1500 - 2000 K) and flame velocity (ϕ = 0.5 - 2.4).

3. The flame velocity of CH_4-air flames at rich conditions is overpredicted in the

original mechanism [26]. An error in the k_∞ of the pressure dependent reaction $CH_4 + M \rightarrow CH_3 + H + M$ (R93) found in the original mechanism is corrected. The reaction of CH_3 with O_2 is an important propagation step in methane combustion. The rate of $CH_3 + O_2 \rightarrow O + CH_3O$ (R72) is taken from the recommendation of Tsang et al. [52]. This change improves the prediction of CH_4-O_2 ignition delay time prediction at high pressures (see Fig. 3.7).

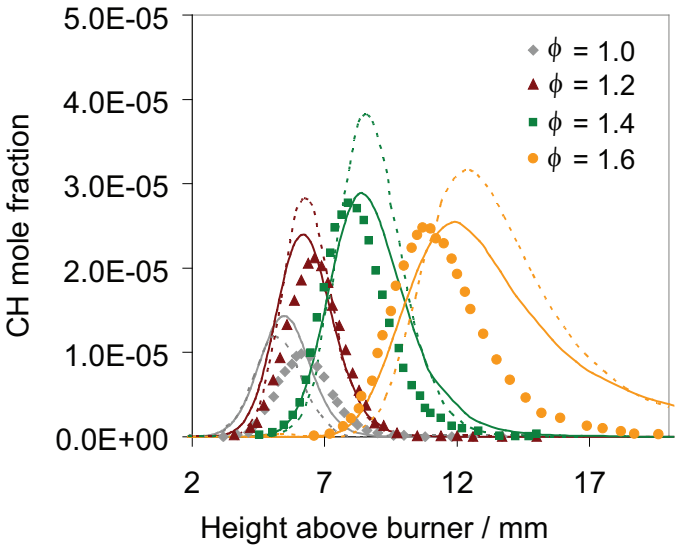

Figure 3.14: Comparison of measured and simulated absolute CH concentrations for $CH_4/O_2/Ar$ flames at four fuel stoichiometries (ϕ = 1.0, 1.2, 1.4, and 1.6). Experiments: Thoman et al. [47]. Symbols: experiments, line: simulation present work, dashed line: simulation with Gri-mech 3.0 [39].

The above modifications lead to the better prediction of CH concentrations in flame conditions. Among recent works, Thoman et al. [47] measured CH concentrations in stoichiometric and rich methane-oxygen-argon flames (ϕ = 1.0, 1.2, 1.4, and 1.6) via cavity ringdown spectroscopy at 0.04 bar pressure. The selection of argon instead of nitrogen (in air) is done to avoid the effect of CH consumption via NO rather than O_2. The CH concentrations simulated with the original mechanism [26] are about 4 to 4.5 times higher than the measured absolute concentrations. Including the above modifications, the calculated concentrations are in very good agreement with measurements. As shown in Fig. 3.14, the peak value of CH mole fraction from GRI-mech 3.0 [39] at rich conditions are about 1.5 times higher compared to the measurements whereas the

results from the mechanism discussed here are closer to the measurement. The stoichiometric flame appears closer to the burner surface in simulation whereas they appears slightly later in the measurement. In the richest flame (ϕ = 1.6), the consumption of CH is slower than predicted by the measurement which is likely due to the fact that at rich conditions there is consumption of CH leading to the formation of soot precursors. As the soot formation is not included in the mechanism, the decay part shows slow consumption of CH.

A reaction flow analysis is performed at the distance from burner where CH concentration peaks i.e. for the stoichiometric case at z = 0.51 cm and for rich case, ϕ = 1.6, at z = 1.18 cm. The CH concentration is dominated by the reaction of $^3CH_2$ with H and OH. Under rich conditions the reaction $^3CH_2$ + H is the major reaction channel forming CH. As known, the $^3CH_2$ is formed in the reaction $^1CH_2$ + M $\rightarrow$ $^3CH_2$ + M reaction in addition to the smaller channel HCCO + H $\rightarrow$ $^3CH_2$ + CO. This secondary channel contributes about 20% in the rich case whereas under stoichiometric condition it is a minor (5%) channel. Subsequently, C_2H_2 is the important precursor for HCCO and C_2H concentration whereby explaining the importance of acetylene chemistry in this reaction channel which will be further linked to the chemiluminating species formation. The $^1CH_2$ is formed from the decomposition of CH_4 to CH_3. The sensitivity analysis

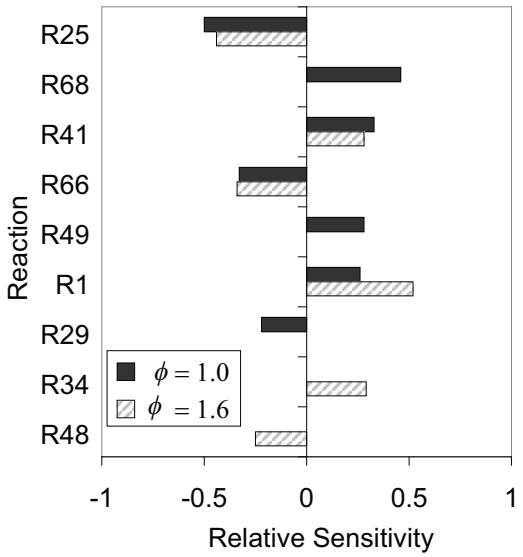

Figure 3.15: Sensitivity analysis performed at the peak of the CH concentration for the $CH_4/O_2/Ar$ flames [47] at stoichiometric (ϕ = 1.0) and fuel-rich (ϕ = 1.6) condition. The concentration profiles are presented in earlier Fig. 3.14.

performed at these conditions shows that the CH formation has positive sensitivity towards the reaction $CH_3 + OH \rightarrow {}^1CH_2 + H$ and reaction ${}^3CH_2 + H \rightarrow CH + H_2$ at both fuel stoichiometries (Fig. 3.15). As seen in the reaction flow analysis, this is due to the fact that they are the important formation channels to the CH production. Similarly, the CH has negative sensitivity to the $CH + H \rightarrow C + H_2$ and $CH + O_2 \rightarrow CHO + O$ reactions which are both important CH consumption reactions. Figure

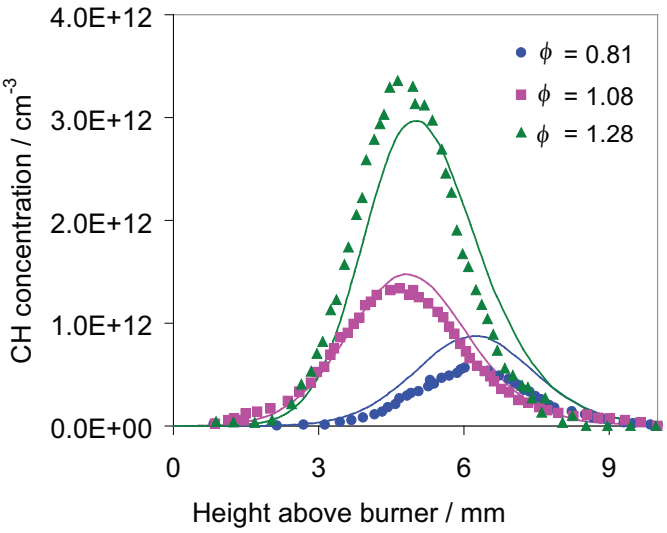

Figure 3.16: Comparison of measured and simulated absolute peak CH-concentrations for lean ($\phi = 0.8$), stoichiometric and rich ($\phi = 1.28$) CH_4 - air flames. Symbols: experiments (Berg et al. [53]), line: simulation.

3.16 shows CH prediction in CH_4-air flames at three fuel stoichiometry measured in [53]. The CH concentrations are in very good agreement with the measurements. The CH concentrations in stoichiometric and rich CH_4-, C_2H_4-, C_2H_6- air flames are also measured by Smith et al. [46]. The peak CH concentration with modified and original mechanism are shown in Fig. 3.17. The concentration of CH at given stoichiometry are nearly the same irrespective of the fuel. The original mechanism overpredicts the CH concentrations by a factor of two to three. As seen Fig. 3.17, the modified mechanism captures the CH concentrations for all three stoichiometries of methane -air flames. There is an underprediction of about two to three times at C_2H_6- rich and C_2H_4- rich and stoichiometric air flames.

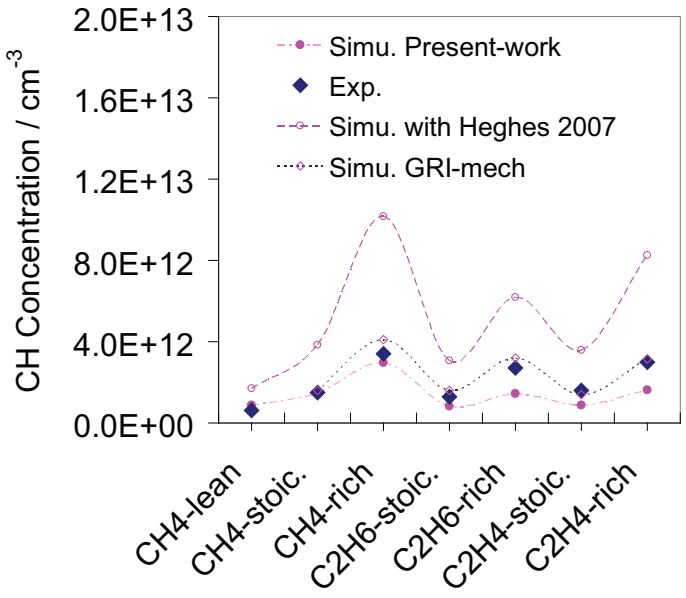

Figure 3.17: Comparison of measured and simulated absolute peak CH-concentrations for stoichiometric and rich ($\phi = 1.28$) CH_4-, C_2H_4-, C_2H_6-air flames. Experiments: Smith et al. [46].

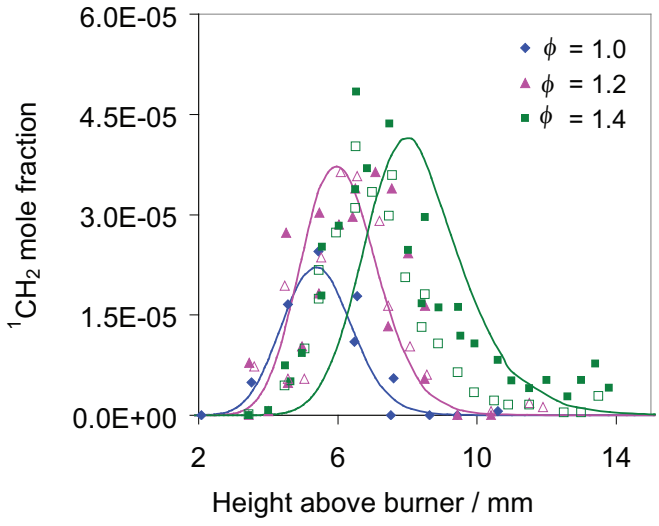

Figure 3.18: A simulation and a comparison with experimental results for singlet methylene ($^1CH_2$) concentration profiles is performed for three $CH_4/O_2/Ar$ flames ($\phi = 1.0, 1.2, 1.4$) as a function of height above the burner. The open and closed symbols for $\phi = 1.4$ corresponds to measurements at two different spectral lines ($^rQ_{0.7}$ and $^rQ_{0.4}$) and are described in Fig. 4 of [54]. Symbols: experiments by McIlroy [54], lines: simulations.

As seen earlier, the ground state species CH and C_2H are important for the description of OH*, CH* chemiluminescence. Similarly, the $^1CH_2$, C, and C_3 are important for the C_2* concentrations. The C_2* formation reactions suggested in literature are $^1CH_2$ + C and C_3 + O [1]. There are no measurements available for ground state C- and C_3-concentrations at flame conditions, however $^1CH_2$ is measured by McIlroy (1998) [54]. The concentrations of $^1CH_2$ are measured for four different fuel stoichiometries (ϕ = 1.0, 1.2, 1.4, and 1.6) of $CH_4/O_2/Ar$ mixtures. A comparison with simulations is shown in Fig. 3.18. All the four $^1CH_2$ concentrations are in excellent agreement with the measurement.

3.3 C_3-C_4 oxidation

The consumption of C_3 and C_4 species is observed by thermal decomposition reactions and by attack of H, O, and OH radicals where smaller alkyl radicals are formed. Higher alkanes are not formed and so the mechanism of smaller alkanes is relevant for the description of the C_3-C_4 oxidation which is discussed in the previous section.

$$(\text{R256}) : C_3H_8 \rightarrow CH_3 + C_2H_5,$$

$$\begin{aligned}(\text{R396}) - (\text{R398}) : C_4H_{10} &\rightarrow CH_3 + C_3H_7,\\ &\rightarrow tC_4H_9 + H,\\ &\rightarrow iC_4H_9 + H,\end{aligned}$$

$$(\text{R257}) - (\text{R262}) : C_3H_8 + H(/ + O/ + OH) \rightarrow nC_3H_7 + H_2(/ + OH + /H_2O),$$

$$\begin{aligned}(\text{R399}) - (\text{R404}) : C_4H_{10} + H(/ + O/ + OH) &\rightarrow iC_4H_9 + H_2(/ + OH + /H_2O),\\ &\rightarrow tC_4H_9 + H_2(/ + OH + /H_2O).\end{aligned}$$

The decomposition reactions of fuels such as C_3H_8 and C_4H_{10} are given by reactions (R256), (R396)-(R398). In these reactions smaller alkyls (CH_3, C_2H_5, and i-C_3H_7) are formed. The C_3H_8 fuel is attacked by H, O, and OH radicals forming alkyls (n-C_3H_7) as shown in reactions (R257)-(R262). Similarly in the reactions of C_4H_{10} with H, O, and OH forms i-C_4H_9 (and t-C_4H_9) given by reactions (R399)-(R404). The results of higher hydrocarbons are not presented here as they are similar to the one presented in [26].

4 Chemiluminescence Mechanism

The chemiluminescence reaction kinetics requires the knowledge of important reactions for the formation and consumption of excited species and their reaction rates. Different studies are dedicated to the identification of the formation pathways of excited species. The rate of consumption can be obtained from the lifetime of these species and are relatively known [55] compared to the formation rates. The first measurement and detailed kinetics studies were done in the 1970s by Gaydon [1] since then significant progress has been made in this field. However, the fundamental understanding on the relation between the measured intensity and the simulated concentrations of the chemiluminescent species is still lacking. Therefore, there exists still uncertainty about the important formation reactions forming these species, specifically for CH* and C_2* formation. In addition, very few studies have been done in N_2O environment, where there are additional channels for the formation of these excited species. The concentration of these excited species is much lower compared to the important ground state species (more than five orders of magnitude) and therefore their presence has nearly no impact on the overall oxidation process. Due to their low production rates and rapid removal rates, they are often assumed to be in quasi-steady state [10].

The reaction kinetics of excited species can be described by three different types of reactions. The formation reaction (4.1) and its subsequent consumption by radiative decay (4.2) and non-reactive collisional quenching reactions (4.3). The excited state X* formed is short lived and returns to the ground state via two channels. In the first channel, it emits its excess energy in form of light in a radiative decay reaction (4.2). In second channel, the excess energy of X* is transferred to the colliding molecule (4.3).

$$A + B \rightarrow C + X^*, \tag{4.1}$$

$$X^* \rightarrow X + h\nu, \tag{4.2}$$

$$X^* + M \rightarrow X + M. \tag{4.3}$$

4.1 Formation of OH*

The main formation reaction of OH* in hydrocarbon mixtures is:

$$(R414) : CH + O_2 \rightarrow CO + OH^*.$$

This reaction is initially proposed by Krishnamachari and Broida [56] who studied the emission spectra of oxygen-acetylene flames at low pressures. Becker et al. (1977) [57] find that the formation pathway suggested by Krishnamachari et al. does not explain all the OH* formed and distinguish between *hot* and *cold* OH* emission. The formation of OH* from the reaction of CH radical with molecular oxygen only accounts for the dominating *hot* chemiluminescence. However, they are unable to identify the reaction(s) responsible for the additional *cold* OH* emissions.

The rate of this reaction is found to be temperature independent in most literature studies (or very small dependence). The rate coefficient is first derived by Porter et al. (1967) [58] by correlating measured CH-, O_2-, and OH*-profiles in methane and acetylene flames between 800 and 2000 K. A rate of 6×10^{10} $cm^3mol^{-1}s^{-1}$ is proposed. Messing et al. [59] and Lichtin et al. [60] determine the reaction rate at room temperature via chemiluminescence detection. Berman et al. [61] study the temperature dependence of CH with O_2 in the temperature range from 297 to 679 K using two-laser photolysis techniques. They find very little temperature dependence of OH*. The rate given is 3.25×10^{13} $cm^3mol^{-1}s^{-1}$. This rate is two orders of magnitude higher than that obtained by Porter et al. [58]. Grebe and Homann [62] use a flow-reactor to study the C_2H_2/O/H-system at room temperature and calculate a rate coefficient of 4.8×10^{10} $cm^3mol^{-1}s^{-1}$, which is similar to the high temperature value of Porter et al. [58]. Among the recent studies, reaction rate data are available from Smith et al. [63], Carl et al. [64], and Hall et al. [65]. Smith and co-workers [63] study low pressure methane flames. The experimentally measured flame species profiles are compared with simulated profiles and a reaction rate of 1.8×10^{11} $cm^3mol^{-1}s^{-1}$ at flame temperature is indirectly recommended by providing a fit of the simulated OH* profile with experiments. This reaction rate is suggested by, Carl et al. [64], who investigate C_2H_2/O/H/O_2 atomic flames. A low

activation energy of 0.7 kJmol^{-1} has been estimated over the temperature range 296 to 511 K. At high temperatures (1000 - 2000 K), shock-tube studies are done by Hall et al. [65] where for the first time a temperature dependence of the reaction rate is shown with an activation energy of 17.38 kJmol^{-1}. The reaction rate coefficient from these authors is plotted in Fig. 4.1. The above reaction explain OH* formation in

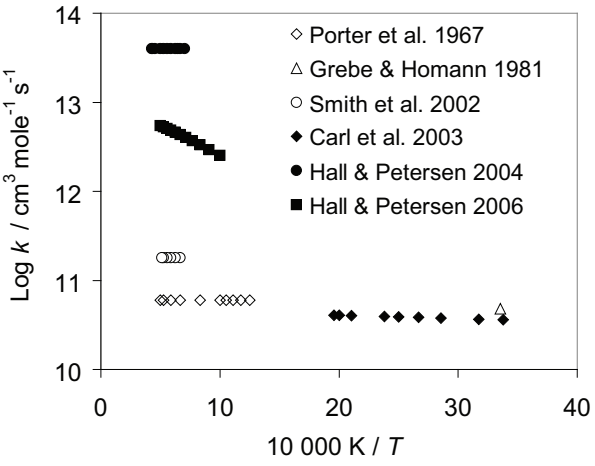

Figure 4.1: Arrhenius plot for the rate coefficients of reaction CH + O_2 forming OH*.

hydrocarbon combustion process. In hydrogen mixtures OH* is considered to be formed mainly by the reaction of atomic H with atomic O and a collision partner, as suggested by Charton and Gaydon [66] and Gaydon [1]:

$$(\mathrm{R413}) : \mathrm{H} + \mathrm{O} + \mathrm{M} \rightarrow \mathrm{M} + \mathrm{OH}^{*}.$$

This reaction is reported to be also important in hydrogen/methane -flames [67] where it can have important contribution to the OH* formation. The first suggestions for its rate are from Kaskan [68] who studied OH* emission in rich $H_2/O_2/N_2$-flames and later in 1982 from shock-tube studies of Hidaka et al. [69] and Koike et al. [70]. Hidaka et al. measured the rate coefficient of this reaction in the temperature range of 1200 - 3200 K for H_2/O_2 mixtures by studying the intensity and the temporal variation of OH* emission. Among recent studies, indirectly inferred rate data is from Smith et al. [34] who predict a reaction rate of $k_{(\mathrm{R413})} = 5.4{\times}10^{12}$ cm^{6}mol^{-2}s^{-1} obtained from a comparison of the GRI 3.0 [39] reaction mechanism and experimentally determined OH* flame emissions from hydrogen-air flames. Hall and Petersen [65] conduct shock-tube

experiments and correlate the peak emission and concentrations from their model and estimate an activation energy of about 42 kJmol^{-1}. The reaction rate recommended is $k = 3.1\times10^{14}$ cm^{3}mol^{-1}s^{-1} exp(-42 $R^{-1}T^{-1}$ kJmol^{-1}), which is higher than that from Smith et al. [34]. Very recently, based on the shock-tube experiments and numerical model comparison, a rate of this reaction is recommended in [27]. The details of this work is discussed later in the results. The reaction rate coefficient from different authors is plotted in Fig. 5.3.

In addition to this, there are few reactions recommended in the literature but are not widely accepted either due to their low energies to form OH*. For example, Haber and Vandsburger (2003) [2] argued that the formation path of OH* through the reaction between CH and molecular oxygen may not describe all OH* formed. They suggested a reaction between the formyl radical with atomic oxygen (HCO + O $\rightarrow$ CO + OH*). The only information on the rate coefficient of this reaction is given by them ($k = 2.89\times10^{11}$ cm^{3}mol^{-1}s^{-1} exp(-1.93 $R^{-1}T^{-1}$ kJmol^{-1})). However, it is seen that this has nearly no influence on OH* formation [63]. Marques et al. [71] in their simulations of acetylene combustion suggest H + O_2 $\rightarrow$ OH* + O to be forming about 90% of total OH*. In their work [71] the rate coefficient of this reaction is assumed to be identical to the rate coefficient of the ground state reaction H + O_2 $\rightarrow$ OH + O. They find through a production rate mechanism that their proposed OH* formation reaction is the principle path that contributes to about 90% of the total OH* formation and removing it from the mechanism would no longer match the experimental results. In the present work it is seen that an incorporation of this reaction in the kinetics model significantly alters the ground state chemistry. Therefore, this reaction is not added to our OH* sub-mechanism. Also recently Skrebkov et al. [72] suggested H_2 + HO_2 $\rightarrow$ H_2O + OH* to be important reaction forming OH*. However, as discussed in [27], the OH* profile with this reaction in the mechanism predicts the OH* peak too early in time compared to the measurement, ruling out the possibility of this reaction.

The consumption of OH* is given by reactions:

$$(\text{R416}) : \text{OH}^* \rightarrow \text{OH} + h\nu,$$

$$(\text{R417}) - (\text{R426}) : \text{OH}^* + \text{M} \rightarrow \text{OH} + \text{M}.$$

The rate of the radiative decay reaction is proposed by several authors (Gaydon 1974 [1];

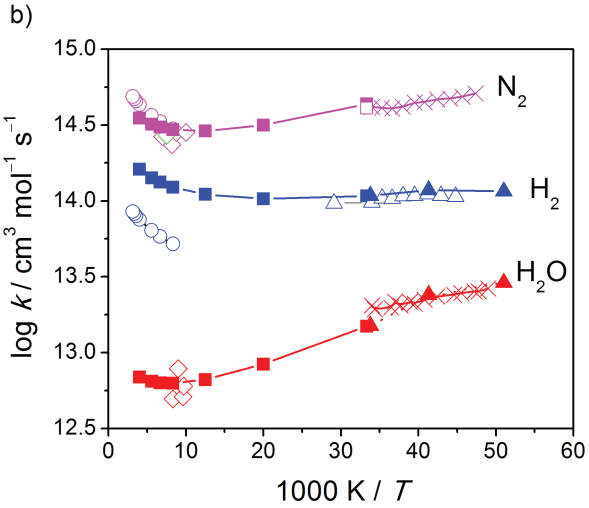

Figure 4.2: Arrhenius plot for the OH* quenching reactions with third partner M = N_2, H_2, and H_2O. Symbols: ♢ Fairchild et al. [73]; ■ Tamura et al. [55]; × Bailey et al. [74]; □ Hemming et al. [75]; ▲ Hemming et al. [76]; ○ Hidaka et al. [69]; △ Heard and Henderson [77].

Hidaka et al. 1982 [69]; Paul et al. 1995 [78]). In the non-reactive collisional quenching reactions (R417)-(R426) the OH* exchanges excess energy with colliding molecules. The ratio of the rates of (R416) to quenching reaction determines the quantum yield of the chemiluminescence. At typical conditions in atmospheric pressure flames this value is in the order of 10^{-3} or less. The collision partners M = O_2, H_2, H_2O, CO, CO_2, N_2, CH_4, H, OH, and Ar are studied at various temperatures ranging from room temperature to flame temperature by several authors [57, 73–77, 79]. Becker et al. [57] provide quenching rate constants for M = H_2, H, and Ar at room temperature. Fluorescence excitation by a dye-laser is applied to measure the OH* lifetime in the presence of H_2, H, and Ar. Fairchild et al. [73] measure thermally-averaged collisional quenching with CH_4, CO_2, CO, H_2O, O_2, and H_2 by laser-induced fluorescence (LIF) at about 1100 K. The OH* quenching with H_2O and atomic H is studied by Jeffries et al. [79] in low-pressure stoichiometric $H_2/O_2/N_2O$-flames also using LIF. A recent study of Bailey et al. [74] investigates the temperature dependence of OH* quenching for collision partners such as N_2, CO_2, and O_2 at room temperature. Hemming et al. [75, 76] study the influence of N_2, O_2, and H_2 at and below room temperature. Heard et al. [77] determined the H_2 quenching rate at low temperatures (200 - 344 K) in a flash-photolysis system. All these quenching rate data are in good agreement with each other from room to flame temperature. For

collision partners such as M = H, O, and OH few information is available due to the complexity of their measurement. The compilation of all such published data of major colliding partners is given by Tamura et al. [55] and the recommendations are for the range of 300 - 2500 K. Fig. 4.2 provides information on the major OH* quenching rates in an Arrhenius plot.

4.2 Formation of CH*

CH* chemiluminescence is seen at 431 nm CH(A-X), 390 nm CH(B-X) and at 314 nm CH(C-X) in flame spectra. About 80% of CH* seen in flames is from the CH(A-X) transition whereas only 20% from the other two transitions, mainly from CH(B-X) [63]. Since the CH(C-X) transitions are very weak, they are not studied. Although all the three states can be measured, due to lack of any rate data for CH(B) and CH(C) states, total CH is modeled in present work. Three different reactions forming CH* are proposed in the literature. CH* emission in hydrocarbon flame is first proposed by Gaydon [1] from the reaction of C_2 with OH, and is also supported by Bulewicz [80]:

$$(\text{R429}) : C_2 + OH \rightarrow CO_2 + CH^*.$$

However, this hypothesis is later rejected by Brenig [81] who finds no CH* in systems containing C_2-, CH-, and OH- radicals in absence of oxygen atoms. Hand and Kistiakowsky (1962) [82] study acetylene-oxygen reactions in shock waves and propose the reactions of C_2H with molecular and atomic oxygen:

$$(\text{R427}) : C_2H + O_2 \rightarrow CO_2 + CH^*,$$

$$(\text{R428}) : C_2H + O \rightarrow CO + CH^*.$$

Bowman [83] studied the high temperature oxidation of methane in a shock-tube and proposes that only reactions (R429) and (R427) are sufficiently exothermic to form CH*. Matsuda [84] supports the reaction (R427) and proposes this reaction to be responsible for the emission of CH* in all its three states ($A^2\Delta$, $B^2\Sigma^-$, $C^2\Sigma^+$).

However, different experimental and modeling work supports one or the other reaction

and it is not clearly established which reaction is an important source of CH*. Several suggestions on the rate coefficient of the reaction (R427) are made in the literature. Hwang et al. (1987) [85] estimate the rate of this reaction to be $k_{(R427)} = 4.5\times10^{15}$ $cm^3mol^{-1}s^{-1}$ exp(-105 $R^{-1}T^{-1}$ $kJmol^{-1}$) with the activation energy derived from Matsuda et al. [84] and the A-factor adjusted to match the experimental emission intensity from shock-tube experiments. Eraslan and Brown (1988) [86] compare computational model results for flames with different experimental values published in the literature. Among recent works, Devriendt et al. (1996) [87] give the room temperature reaction rate where C_2H and oxygen atoms are created, simultaneously, by pulse laser photolysis and the resulting CH* chemiluminescence is measured. Later they in Elsamra et al. (2005) [88] determine the temperature dependence in the range of 316 to 837 K using the same techniques as Devriendt et al. [87]. Smith and co-workers [34] extrapolate the reaction rate given by Devriendt et al. [87] to flame temperatures (Fig. 4.3).

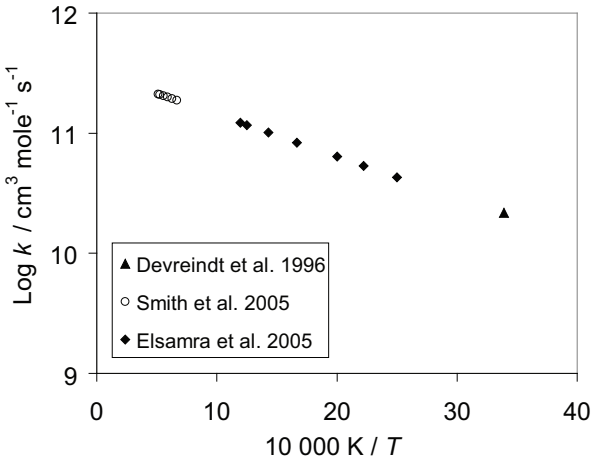

Figure 4.3: Arrhenius diagram for the CH* formation reaction $C_2H + O_2$.

Among earlier studies on the rate coefficient of the reaction $C_2H + O \rightarrow CO + CH^*$ (R428), the rate data suggested by Grebe and Homann [62] is $k_{(R428)} = 6.6\times10^{11}$ $cm^3mol^{-1}s^{-1}$ at room temperature and the one by Eraslan et al. [86] is $k_{(R428)} = 7.0\times10^{11}$ $cm^3mol^{-1}s^{-1}$ at higher temperature (1600 - 1800 K). Among recent studies, Devriendt et al. [87], by using sophisticated sampling techniques, are able to provide the room temperature reaction rate to be $k_{(R428)} = 1.08\times10^{13}$ $cm^3mol^{-1}s^{-1}$ (Fig. 4.4) which is much higher than the previous values. They provide the first direct identification of

reaction (R428) as a source of CH* in C_2H_2/O/H-flames at room temperature and over the temperature range (300 - 1000 K) [49]. Smith et al. (2002) [63] recommend a rate of $k_{(R428)} = 6.2\times10^{12}$ cm^{3}mol^{-1}s^{-1} by comparing low pressure methane/air flame data with GRI-mech 3.0 [39] results. This reaction rate is later (Smith et al. (2005) [34]) refined to a lower value where the experiments are performed with methane/nitrous oxide flames to avoid the ambiguity over the C_2H + O and C_2H + O_2 reaction forming CH*.

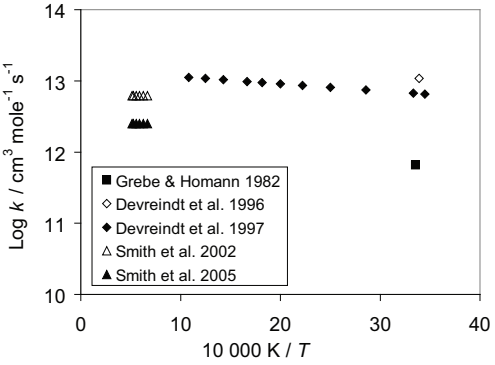

Figure 4.4: Arrhenius diagram for the CH* formation reaction C_2H + O.

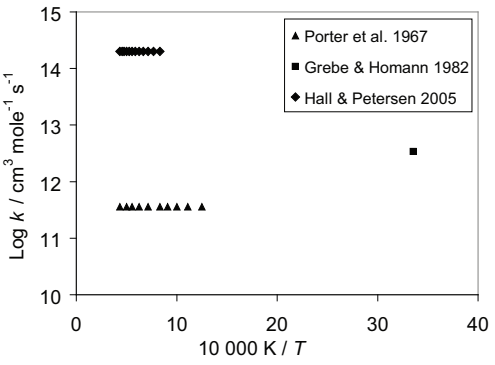

Figure 4.5: Arrhenius diagram for the CH* formation reaction C_2 + OH.

Among previous studies, the rate of the C_2 + OH reaction (R429) is proposed by Porter et al. (1967) [58], Grebe and Homann [62], and Eraslan et al. [86]. Recently, Hall et al. [89] study high temperature (1200 - 2300 K), atmospheric pressure shock-tube experiments and compare the maximum intensity at various temperatures and equivalence ratios. They find the formation of CH* in the reaction C_2 + OH to be the most sensitive reaction towards CH*-formation. They obtain a reaction rate of $k_{(R429)} = 2.0\times10^{14}$ cm^{3}mol^{-1}s^{-1} (Fig. 4.5). Few studies are dedicated to the rate recommendation of reaction forming CH* from C_2 + OH (R429). Among these, Mertens [90] studied CH* in methane and acetylene mixtures in shock-tubes. The find that CH* in both mixtures is produced from reactions (R427) and (R428) whereas they are unable to conclude the role of reaction (R429) on CH* formation. On other hand, Hall et al. [89] in their studies find reaction (R429) to be sensitive to the CH* formation in CH_4/H_2 mixtures. The quenching reaction rates of CH* consumption are compiled in Tamura et al. [55] in temperature range of 300 - 2500 K.

4.3 Formation of C_2*

The chemiluminescence from the C_2(d-a) Swan band are mainly found between 470-550 nm of flame spectra. Few reactions are proposed for the formation of C_2* among which the reaction of CH_2 with C and C_2H with H are originally proposed by Gaydon (1974) [1]:

$$(\text{R441}) : CH_2 + C \rightarrow H_2 + C_2^*,$$

$$(\text{R442}) : C_3 + O \rightarrow CO + C_2^*.$$

The reaction of C_2H with H is also studied by Ferguson (1955) [91] where the author mentions that it contributes only little to C_2* chemiluminescence in acetylene flames. Another candidate reaction supported by him is CH + CH $\rightarrow$ H_2 + C_2^*. However, this reaction is not seen to be contributing significantly to the C_2* formation [62, 80]. Reaction (R441) is considered to be exothermic enough to produce C_2*. This reaction is also supported by Grebe and Homann [62] as an important reaction forming C_2* who investigated the C_2H_2/O/H-system. The emission of C_2* is also observed by Savadatti and Broida (1966) who study atomic carbon flames in atomic oxygen. They suggest the reaction of C_3 with atomic oxygen and find the C_2* swan band in atomic oxygen and molecular oxygen flame. They show that since atomic oxygen is more reactive than molecular oxygen, it is likely that reaction (R442) is the possible source of C_2*.

Information on the reaction rate coefficient forming C_2* is scarcely available. Only Grebe and Homann [62] and very recently Smith et al. (2005) [46] propose the value for the rate of the CH_2 + C reaction to be $k_{(\text{R441})} = 7.5\times10^{13}$ cm^{3}mol^{-1}s^{-1} at room temperature and 2.4×10^{12} cm^{3}mol^{-1}s^{-1} at high temperatures (1500 - 1950 K), respectively. The rate of the C_3 + O reaction is only available from Smith et al. (2005) [46], $k_{(\text{R442})} = 4.2\times10^{11}$ cm^{3}mol^{-1}s^{-1}, in the high temperature range of 1500 to 1950 K where low pressure flat premixed flames with methane, ethane and ethylene fuel are studied using LIF.

The consumption rate of C_2* by radiative decay and collisional quenching of major quenchers are estimated and only given by Smith et al. [46]. The radiative decay rate is $k_{(\text{R441})} = 1.0\times10^{7}$ cm^{3}mol^{-1}s^{-1} and the rate of quenching reactions are given in Appendix.

4.4 Additional sub-mechanism of C, C_2, C_3, C_2O, C_3H and C_3H_2

The formation of CH* and C_2* are linked to C_2, C_3 species via reactions $C_2 + OH \rightarrow CO_2 + CH^*$ (R429) and $C_3 + O \rightarrow CO + C_2^*$ (R442) respectively. Although these species are reactive in nature, a detailed study of these species is still unavailable. Therefore these species are not part of existing combustion reaction mechanisms as their role in combustion remains relatively unclear. They are included in the present work due to their importance in the CH* and C_2* formation chemistry. There is very few information available on the reactions forming and consuming these species and so they are not part of the most reaction mechanism databases. The measurement of the absolute C_2 is difficult due to its low concentration (ppb levels) which requires highly specialized equipment. The chemistry of these species is closely linked to the C_2H_2 chemistry.

4.4.1 Reactions of C

The information on atomic C reacting with other radicals and species is sparse and rate data available are limited. The important reactions of C, that are suggested in literature, are with OH, O_2, H_2O, CH, C_2H, CH_2, and CH_4. The rate of these reactions available in the CODATA [42] are only available at room temperature. The important reaction for the formation of C is $CH + H \rightarrow H_2 + C$. Thus the chemistry of C is linked to the CH chemistry. The products of the C consuming reactions are mainly C_2 and C_3. The rate of these reactions are summarized in the Appendix.

4.4.2 Reactions of C_2

The dicarbon molecule C_2 is found in its triplet $a(^3\Pi)$ and its singlet $X(^1\Sigma_g^+)$ state. At flame temperatures, the triplet state, due to its higher degeneracy, is considered to be more populated (about 80%) [92]. Since few information is available on the formation and consumption reaction rates of these two states separately, we have considered the total C_2 from both states. Very recently a few studies have discussed the C_2 measurement and its mechanism in flames [46, 92, 93]. The main formation path of C_2 is through the

reaction of C_3 with atomic and molecular oxygen. In addition the reaction of C_2H with O also leads to C_2. The important reactions consuming C_2 are with H_2, O_2, OH, O, CH, and CH_4. At very high temperatures (2500 - 3500 K) C_2O is formed from the above reactions.

4.4.3 Reactions of C_3

The chemistry of C_3 is important as it leads to the formation of important C_2 species. The C_3 is formed from the reactions of C with other carbon containing radicals (CH, C_2H, or C_2H_2). The important C_3 consumption channels are via C_3 + O and C_3 + O_2 forming C_2. Thus the chemistry of C_2 and C_3 is closely interlinked.

4.4.4 Reactions of C_2O, C_3H, and C_3H_2

C_2O formation occurs in the high temperature range, at about 2500 to 3500 K. It is mainly formed from C_2 molecules. The consumption of C_2O mainly leads to CO formation. In addition to this, few reactions of C_3H and C_3H_2 are added to the mechanism. The C_3H is formed from the reaction of C_3H_2 with H atoms. The C_3H formed is the important channel to the C_3 formation. As shown in Fig. 4.6, the formation of C_3H_2

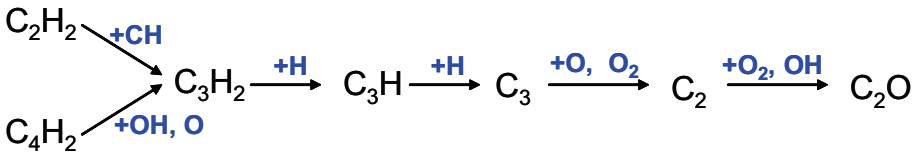

Figure 4.6: Reaction flow schematic of the C_2 formation pathway. The diagram shows how the C_2 formation is linked to the acetylene chemistry.

is due to the reaction of C_2H_2 + CH and C_4H_2 + OH (or O) which explains the direct link of acetylene chemistry to the formation chemistry of C_2. The C_2 is produced from the subsequent decomposition reactions of C_3H, C_3, and C_2. Therefore all this inter-connected species become an important part of the C_2 chemistry.

4.5 Validation of the C_2 chemistry

Only few studies are dedicated to the measurement of absolute concentration of C_2 in flames due to its low concentrations which makes it difficult to measure [46, 92, 93].

Among recent studies, Smith et al. [46] measured C_2 concentrations in ground and excited state in methane-, ethane-, and ethylene- air flames. The absolute values of measured C_2 are in the ppb range and a relative comparison shows that C_2 concentrations increases from CH_4 over C_2H_6 to C_2H_4 flames. The C_2 concentration in given flames are relative to the C_2 concentrations in CH_4-air rich flame.

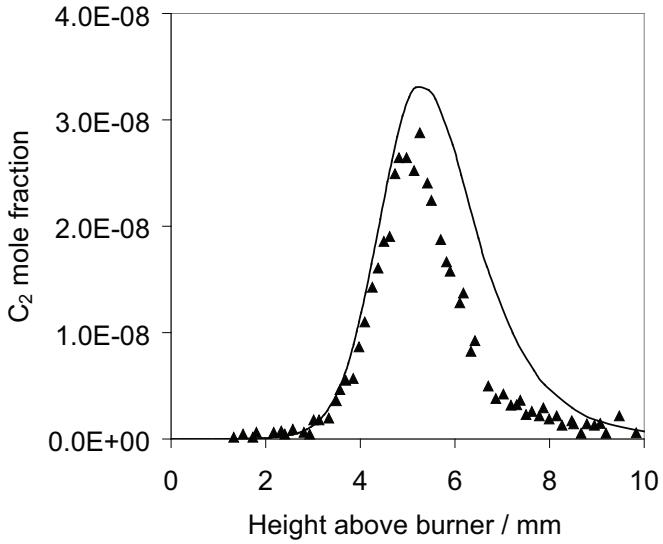

Figure 4.7: A comparison of measured and simulated C_2 concentrations in a low pressure (0.04 bar) laminar premixed CH_4 -air flame ($\phi = 1.28$) measured by Smith et al., [46]. Symbol: experiment, line: simulation with mechanism from present work. Note that the simulated profile is divided by factor of 2.

In Fig. 4.7, the comparison of measured and simulated C_2 concentrations is shown for the rich ($\phi = 1.28$) methane-air flame. Many of the rate of the C_2 reactions are estimates from similar reactions or are available only at room temperatures. Extrapolation of room temperature rate to the flame temperature is not always applicable. Therefore, overprediction of factor of two is seen in the simulated C_2 concentration. However, the peak position and the shape of the profile is well predicted. As shown in Fig. 4.8, when

compared to the CH_4-air rich flame ($\phi = 1.28$), the simulation of the stoichiometric C_2H_6- and C_2H_4 -air flame fairly reproduces the experimental C_2 peak concentrations. However, their concentrations at rich conditions are underpredicted by about 50 and 65% respectively.

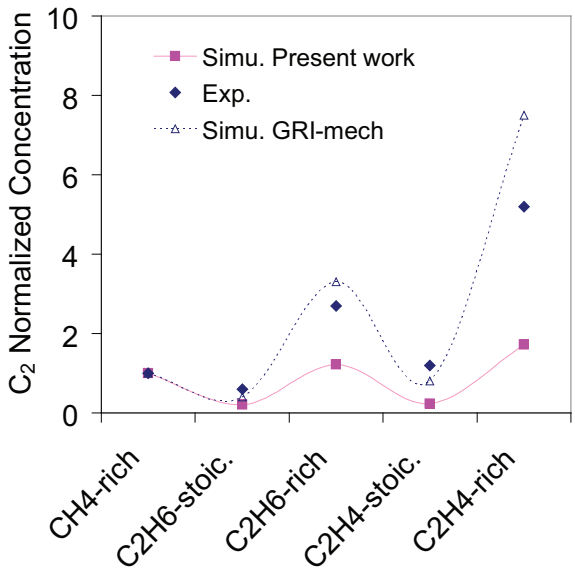

Figure 4.8: A comparison of measured and simulated C_2 concentrations for six different stoichiometric and rich hydrocarbon-air flames. The experiments are performed at low pressure (0.33-0.4 bar) laminar premixed flame condition [46].

Schofield and Steinberg [92] measure C_2 in series of acetylene flame ($\phi = 1.2$ - 2.0). The measured C_2 is given as a function of time. Very recently, Köhler et al. [93] study CH and C_2 concentrations in propene and cyclopentene flames. The simulated results of the propene flame at five different stoichiometries ($\phi = 1.2$, 1.5, 1.8, 2.1, and 2.3) are presented in Fig. 4.9. For the fuel stoichiometry of 1.2 and 1.5, the C_2 concentrations are overpredicted by factor of 6 and 3 respectively. Whereas at higher ϕ they are 2 times higher than the measurements. Although the concentrations of C_2 are higher in case of $\phi = 1.2$ and $\phi = 1.5$, the shape of the profile is in very good agreement compared to the simulations presented in Köhler et al. [93]. In [93], the consumption of C_2 is faster in the measurements compared to the simulations. The concentration of C_2 increases with an increase in fuel stoichiometry as more carbon is available with increase of C/O ratio. The important formation and consumption pathway at this condition is shown in Fig. 4.10.

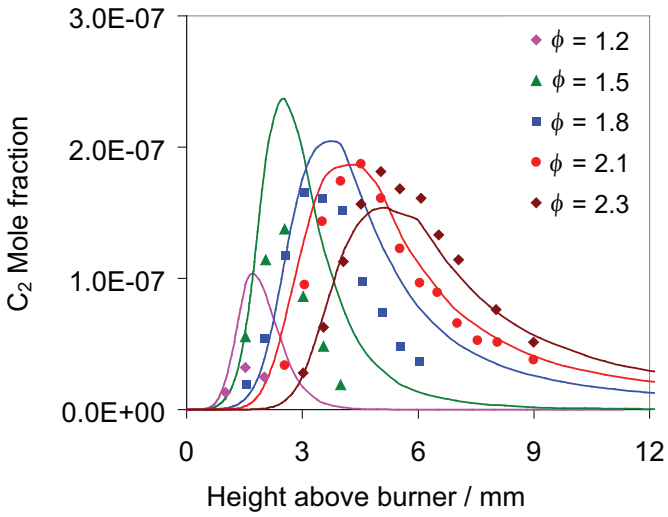

Figure 4.9: The measured and simulated absolute C_2 mole fractions at different propene-O_2-Ar flames at 0.05 bar pressure. Symbols: experiments [93], lines: simulations from the present work (divided by factor of 2).

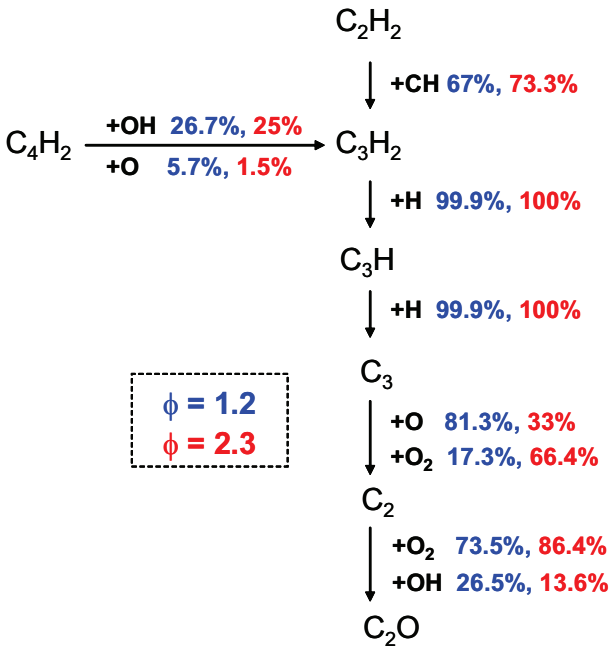

Figure 4.10: Reaction flow analysis of C_2 formation and consumption in a propene-O_2-Ar flame $\phi = 1.2$ and $\phi = 2.3$ presented in Fig. 4.9. The analysis is performed at the distance from burner where the C_2 concentration peaks i.e. 0.174 cm for $\phi = 1.2$ and 0.51 cm for $\phi = 2.3$.

The reaction pathways are presented for two cases, $\phi = 1.2$ and $\phi = 2.3$ in propene flames at the position where C_2 peaks (0.174 cm, $\phi = 1.2$ and 0.51 cm, $\phi = 2.3$). This analysis gives information on reactions important for the C_2 peak. The decomposition of C_2H_2 leads to C_2 formation as discussed earlier. Here the major difference at stoichiometric and rich condition is the formation of C_2 from atomic or molecular oxygen. At stoichiometric condition the reaction of C_3 with atomic oxygen is the dominant source whereas at $\phi = 2.3$ the reaction of $C_3 + O_2$ is the main path to C_2.

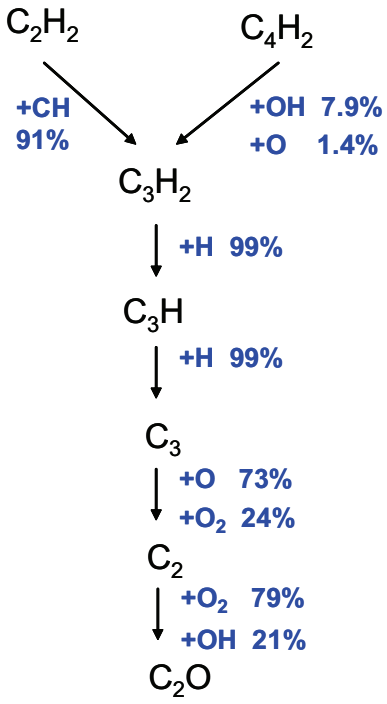

Figure 4.11: Reaction flow analysis for the formation of C_2 in a rich ($\phi = 1.28$) methane-air-flame for the experimental conditions of Smith et al. [46].

The formation paths of C_2 in propene and methane flame are similar, however, its consumption channel slightly varies (Fig. 4.11). In the propene flames, at $\phi = 1.2$ and $\phi = 2.3$, the C_2 is formed from reaction of C_3 with O and O_2. Here the O-channel is dominant in $\phi = 1.2$ and in methane flame (about 70-80%) whereas the O_2-channel is important at richer conditions (about 65%). The C_3 is completely formed from the $C_3H + H \rightarrow C_3 + H_2$ reaction. The C_3H_2 is formed from $C_3H_2 + H \rightarrow C_3H + H_2$. Thus C_3H_2 is an important precursor to the C_2 formation. This C_3H_2 is formed mainly from the reaction of $C_2H_2 + CH$, i.e. about 70% at $\phi = 1.2$, 73% at $\phi = 2.3$ and about 90% in the CH_4-air rich case. Thereby, C_2 formation is connected to the C_2H_2 chemistry. At ϕ

= 1.2 about 20% of C_2 is consumed by C_2O via its reaction with OH and O_2. In addition 60% of it is consumed to form C_2H. A small channel (8%) forms CH in the reaction C_2 + OH. But at richer case ($\phi = 2.3$), only 4% forms C_2O. A larger channel (90%) forms C_2H through its reaction with H_2 and C_2H_2. The consumption of C_3H is dominated by its reaction with O_2 and H to form HCCO and C_3 respectively. Therefore the chemistry of C_2 is linked with the C_2H_2 chemistry. However the influence of C_2 chemistry on C_2H_2 is very small as the concentration of C_2 is in ppb-range which is about two to three orders of magnitude lower than the important species in the C_2H_2 channel.

In present work and all the above reported studies of C_2 ([46], [93]), the addition of the C_2 sub-mechanism does not alter the validation of the ground state chemistry.

5 Validation of the Chemiluminescence Mechanism

The validation of the chemiluminescence mechanism is a challenging task as it involves the validation of its ground state formation chemistry and in addition it requires the validation of its very low concentration species. There are certain experimental difficulties in measurement of such species which leads to an only small number of available experimental data for validation. In this chapter, the validation of CL mechanism is presented where the simulated results are compared to the measurements obtained for shock-heated mixtures and for one-dimensional laminar flame systems. The similations are performed with program HOMREA [94] and INSFLA [94, 95] respectively.

5.1 Simulations of shock-tube measurements

Different groups in literature have discussed the measurement of ignition delay time by following the appearance of electronically excited species. Although due to its low concentrations, the ignition delay times of excited species profile are not dependent on the formation kinetics of these species itself but they provide information on the ground state chemistry. Thereby, it helps in giving an extra check on ground state chemistry. However, following the concentration of excited species as a function of temperature, mixture stoichiometry shall give information on the formation kinetics of the excited species. So far only OH* and CH* are measured at shock-tube conditions. The measurement of C_2* is unavailable in the literature as the shock-heated mixtures are studied mainly in lean conditions where its formation is less likely.

5.1.1 $H_2/O_2/Ar/N_2$ mixtures

OH* formation in hydrogen oxygen mixtures is due to the three body reaction of H+O+M. The temporal variation of OH* in hydrogen mixture is studied in a shock-tube at temperatures of 1400 - 3300 K and at a pressure of 1 bar [27]. The results of the prediction of OH* in the mechanism is validated with the measurements. The OH* intensity measured under the shock-tube conditions cannot be directly related to the computed concentrations as the link between the intensity and concentration is not known. Its comparison requires a calibration factor which can convert the measured intensity to the calculated concentrations. The role of thermal excitation in high temperature chemistry is well-known. In hydrogen-oxygen mixtures, Hidaka et al. [69] and Koike et al. [70] mentioned that the OH* above 2800 K is formed due to the thermal excitation reaction (reverse quenching) and is independent of the formation reactions (H+O+M). This information is used to derive the calibration factor by comparing the measured intensity to the computed concentration. However, before relying on this strategy, three important points need to be clarified [27]:

(i) Additional reactions (example, collisional induced decomposition of OH*) should have a negligible effect only. As discussed in [27] the dissociation of OH* from the reverse reaction $-$(R413) is thermodynamically accessible and the sensitivity analysis shows that it contributes 5% to the OH* peak concentration compared to the 95% due to the quenching reaction. Therefore it can be neglected.

(ii) The measured peak intensity should not suffer from insufficient temporal resolution of the detectors. It is seen that the time resolution of experiments is short enough to not influence the signal traces

(iii) The influence of radiation trapping due to ground state OH must be negligible. The signal emitted from OH* chemiluminescence is partially trapped by ground state OH which is abundant in gases after ignition. It is deduced, from simple analytical approach to quantify signal trapping [27], that this effect is covered by the calibration. The error caused by signal trapping due to the slight variations between calibration and measurement and due to variations in the time profile is estimated to be within the $\pm$3% range.

Table 5.1: Mixture composition, temperature and pressure of the shock-tube experiment [27].

Mixture	ϕ	Composition	T_5 range (K)	p_5 range (bar)
A	0.5	1% H_2 + 1% O_2 in Ar	1400-3300	0.85-1.50
B	1.0	2% H_2 + 1% O_2 in Ar	1440-3180	0.90-1.40
C	0.5	1% H_2 + 1% O_2 + 5% N_2 in Ar	1400-3200	0.90-1.40
D	1.0	2% H_2 + 1% O_2 + 5% N_2 in Ar	1450-3200	0.90-1.45

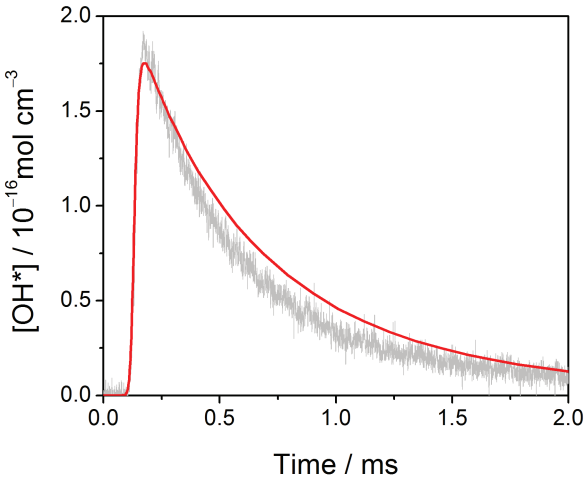

Figure 5.1: Comparison of the temporal variation of the measured OH* intensity with the simulated concentration. The experimental absolute concentration is obtained by the calibration factor discussed in Kathrotia et al. [27]. The composition of the mixture is 1% H_2, 1% O_2 diluted in argon. The initial temperatures and pressures are $T_5 = 1592$ K and $p_5 = 1.27$ bar respectively.

Thus considering this facts, the calibration of the measured OH*-signal to the calculated concentration is obtained at T > 3000 K. A calibration factor of 2.62×10^{-18} $cm^3mol^{-1}mV^{-1}$ is deduced.

Four different mixtures, with Ar and Ar+N_2 as bath gases with fuel stoichiometry $\phi = 0.5$ and 1.0 are studied as shown in Table 5.1. A comparison of temporal variation of measured and calculated OH* is shown in Fig. 5.1, at 1592 K initial temperature and 1.27 bar pressure behind the reflected shock wave (p_5). The shape of the profile and its position on time axis is well reproduced when compared to the experiment. The

measured absolute OH* concentration obtained from the calibration factor described earlier is in the good agreement with the simulations over a wide temperature range of 1400 - 3000 K (Fig. 5.2). The OH* concentrations predicted from different k_{R413} values are compared to the measured converted concentrations at different temperatures. In the first stage of the data evaluation, the reaction rate coefficient k_{R413} is varied by different literature values given in [34,65,69]. Later to obtain better agreement with the experiments, the k_{R413} is varied by keeping values of either A or E fixed. A rate equal to 1.5×10^{-13} cm^{6}mol^{-2}s^{-1} with an activation energy of 25 kJ mol^{-1} is found to give the best representation of the experimental data (Fig. 5.2).

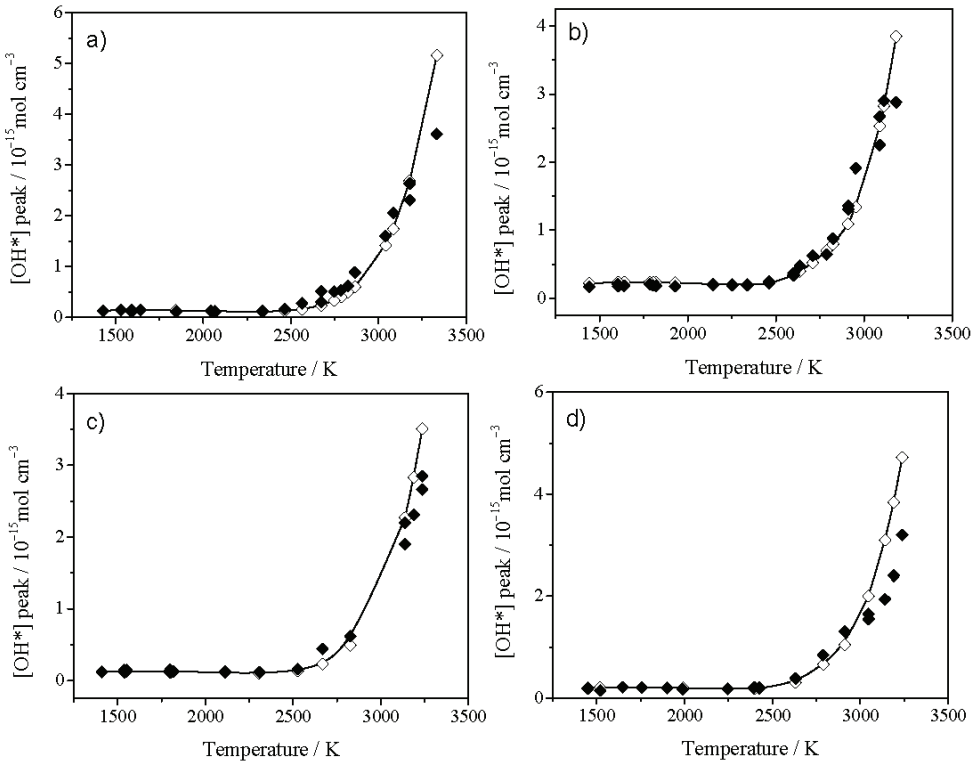

Figure 5.2: Measured and simulated peak OH* concentration at different temperatures. a) mixture A, b) mixture B, c) mixture C, d) mixture D as given in Table 5.1. Closed symbols: experiments, open symbols with line: simulations (see also [27]).

As shown in Fig. 5.3, literature value of k_{R413} differ by about two orders of magnitude from each other. The OH* concentration predicted from the works of Hidaka et al. [69] is about 70% lower than our prediction. This is due to the difference in the quenching rate coefficient of the major collider in their work. Recalculating the rate for the quencher

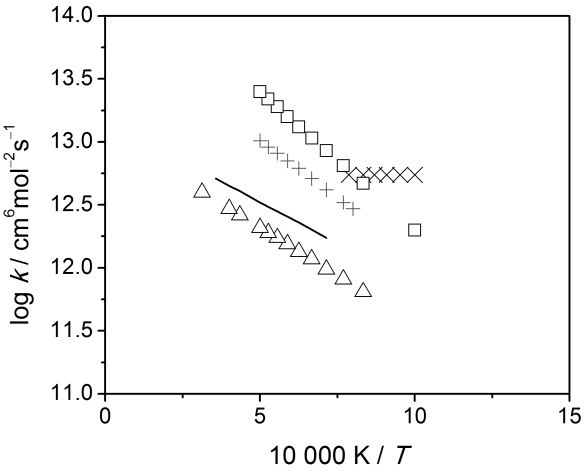

Figure 5.3: Arrhenius plot for the reaction H + O + M forming OH* (R413) Symbols: + Koike et al. [70], △ Hidaka et al. [69], × Smith et al. [34], □ Hall et al. [65], line present work (see also [27]).

correction gives a rate closer to our prediction. With the k_{R413} from Hall and Petersen [65] and Smith et al. [34] the calculated OH* are about eight and four times higher than the OH* measured respectively. The deviation of OH* at intermediate temperatures from [34] is likely due to the fact that it is derived by fitting flame measurements at about 1000 K. When Petersen et al [96] measure k_{R413} at 1000-1800 K, an increase in k_{R413} by one order of magnitude is required to fit the OH* measurements compared to their later study at the temperature range of 1200-2200 K. Therefore, a lower rate is required at higher temperatures compared to the one near 1000 K.

5.1.2 H_2/CO/air mixtures

Kalitan et al. [97] measure OH* in lean 20/80% H_2/CO mixtures at intermediate temperatures (890-1300 K) and three different pressures (1.2, 2.6, and 15.4 bar). They measured ignition delay times using the onset of the OH* emission.

At atmospheric pressures, the prediction of calculated ignition delays at high temperatures are in very good agreement with the measurements. There is disagreement at temperatures below 950 K, where the measured ignition delay times are about one to

two orders of magnitude shorter than the calculations. The trend of the ignition curve at different temperature is however reproduced by the mechanism. The shorter ignition times below 950 K, according to Kalitan et al. [97], is due to the early reaction and subsequent strong detonation waves which cannot be explained by the zero-dimensional calculations done at other temperatures. Figure 5.4 presents the comparison of measured and simulated ignition delay times at three different pressures. All mixtures are 20/80% H_2/CO in air.

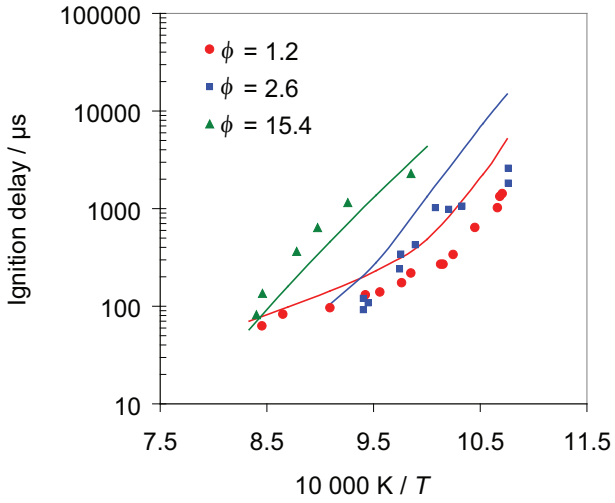

Figure 5.4: Measured and simulated ignition delay times for the 20/80% H_2/CO mixture in air at three different initial pressure. The experimental and simulated ignition delay times are obtained from the onset of the OH* profile. Symbols: experiments, Kalitan et al. [97], line: simulations.

The sensitivity analysis shows that the ignition delay times at given pressure and temperatures are not dependent on chemiluminescence reaction rates, which is apparent. The most sensitive reaction at high and low temperature is the basic chain branching reaction $O_2 + H \rightarrow O + OH$. So although the comparison of measured and simulated ignition delay time would not provide information on the chemiluminescence sub-mechanism, the information provides an additional check on the ground state chemistry. Two different mixtures are tested for the sensitivity, one with high H_2 content (20% CO + 80% H_2) and another mixture which is high in CO content (80% CO + 20% H_2). The reaction which has highest sensitivity to both mixtures at low temperature (915 K) and high temperature (1200 K) is the basic chain branching reaction $O_2 + H \rightarrow O + OH$. The other reactions of secondary importance are $H_2 + O \rightarrow H + OH$ (R2), $HO_2 + H \rightarrow OH$

+ OH (R9), and CO + HO_2 → CO_2 + OH (R23).

Thus, underlying mechanism is well capable of predicting ignition delay times at low temperatures and high pressure.

5.1.3 $H_2/CH_4/O_2$/Ar mixtures

In the hydrocarbon oxidation, the reaction CH + O_2 (R414) is about 99% source of OH*, and a very minor amount of OH* is produced due to the three body reaction (R413). However in order to see the effect of both reactions, a combination of H_2-CH_4 mixture is selected such that both reactions can have an important role in the OH* formation. Therefore, 2% of H_2 is mixed with 0.025% CH_4 and the resulting OH* due to the oxidation is measured under shock-tube conditions [98]. The experiments with $H_2/CH_4/O_2$ diluted in argon mixtures are performed in the temperature range of 1400 - 2200 K and at pressures in range of 1.2 - 1.5 bars.

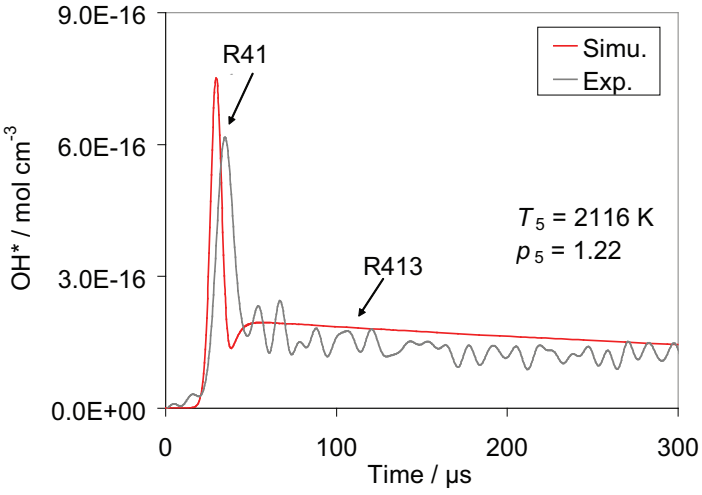

Figure 5.5: OH* concentration profile at 2116 K and 1.22 bar in 0.025% CH_4+2% H_2+1% O_2 + Ar mixture obtained with rate of reaction CH + O_2 from Smith et al. [63]. The experimental OH* intensity is converted to the absolute concentration by the calibration factor discussed in Kathrotia et al. [27]. The experiments are from [98]. The first sharp peak is due to the reaction (R414) and second part of profile is due to the third body reaction H + O + M (R413).

As a result of this the OH* profile shows two distinct peaks arising due to both reactions forming OH*. As shown in Fig. 5.5, the first peak is due to the reaction of CH + O_2 (R414) forming OH*, whereas the second peak arises from the three body reaction (R413). The calibration factor derived from H_2/O_2/Ar mixtures, in [27], is applied to convert the measured intensity to absolute concentration in this mixture. Figure 5.5 shows OH* profile at temperature of 2116 K. The shape of both parts of the OH* curve is very well reproduced by the simulation when the rate of reaction (CH + O_2) recommended by Smith et al. [63] is used in the simulation.

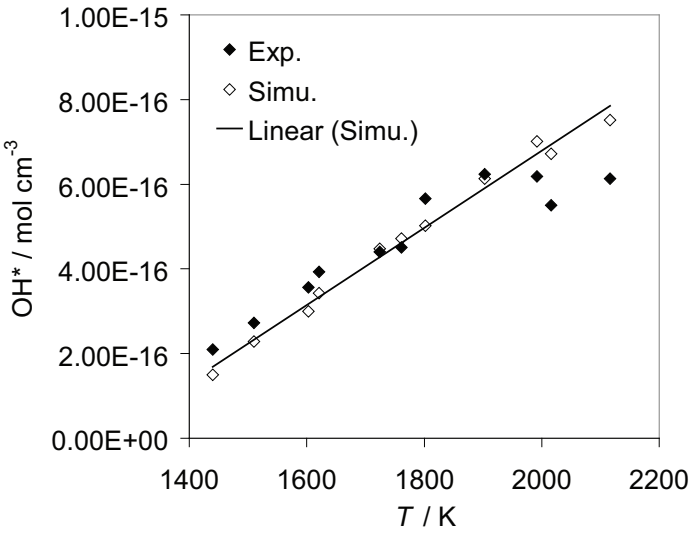

Figure 5.6: Peak OH* concentration in the 0.025% CH_4+2% H_2+1% O_2 + Ar mixture obtained with rate of reaction CH + O_2 from Smith et al [63]. The experimental OH* intensity is converted to the absolute concentration by the calibration factor discussed in Kathrotia et al. [27]. The experiments are from [98].

In Fig. 5.6, comparison of the maximum OH* concentration due to the first peak is made over the temperature range of 1400 to 2200 K. In the calculation the rate of the reaction CH + O_2 is from the recommendation of Smith et al. [63] and the rate of H + O + M is the one recommended in the present work. The results support that the reaction rate $k_{(R414)}$ recommended by Smith et al. reproduces the measured OH* concentrations (Fig. 5.6). The other literature value of reaction rates either under- or over- predicts the OH* concentration from the reaction (R414).

Hall et al. [65] also study methane-hydrogen mixtures under shock-tube conditions. They

recommend a rate for the reaction CH + O_2 as well as for the three body reaction H + O + M forming OH* in hydrogen mixtures. They perform the calibration of OH* in $H_2/O_2/Ar$ and use the calibration to derive the rate of reaction CH + O_2 in $H_2/O_2/Ar$ mixtures diluted with CH_4. The ignition delay time obtained from the onset of measured OH* profile is compared with simulations in Fig. 5.7. The simulation reproduces the measured ignition delay time providing a further validation of the base mechanism.

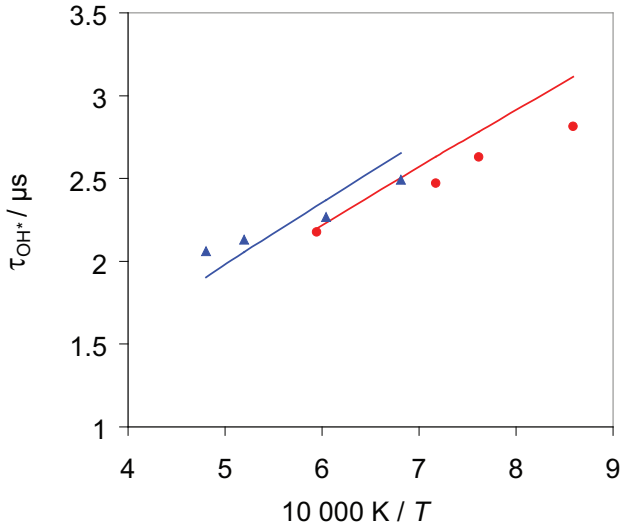

Figure 5.7: A comparison of measured and simulated ignition delay time obtained from the onset of OH* profile. The measurements are done by Hall et al. [65] in a shock-tube with hydrogen mixtures with traces of methane added. The mixture composition is: (1) Red: 0.8% H_2 + 0.01% CH_4 + 0.42% O_2 + Ar and at 1.2 bar (2) Blue: 0.633% H_2 + 0.00187% CH_4 + 0.32% O_2 + Ar and at 1.1 bar.

5.1.4 $C_2H_2/O_2/Ar$ and $C_2H_2/N_2O/Ar$ mixtures

Acetylene oxidation is studied by Rickard et al. [99] who measure CH* and OH* ignition delay times and CL peak times to monitor the reaction progress. They perform experiments in the temperature range 1040 to 2320 K and at atmospheric pressure for different stoichiometries (ϕ = 0.5, 1.0, and 1.53). In addition to the major chain branching reaction H + O_2 → OH + O, they found that the characteristic time of the CH* emission is dependent on the C_2H_2 chemistry and the major reactions important at high (1600 K)

and low (1100 K) temperature conditions are HCCO + H → $^1CH_2$ + CO, HCCO + O_2 → CHO + CO + O, C_2H_2 + O_2 → HCCO + OH, and C_2H_2 + OH → C_2H + H_2O.

Although the ignition delay time comparison does not provide information on the formation kinetics of CH* chemiluminescence, it provide insight into the acetylene chemistry which is important in case of excited species formation kinetics. It also helps in understanding the ignition behavior of fuels by following it with the help of relatively simple optical equipment.

The reaction kinetics of CH* is also studied by Mertens et al. [90]. They measure CH* in methane and acetylene -oxygen mixtures diluted in argon in order to identify the major reaction(s) forming CH*. However, they are unable to conclude on the formation of CH* by the reaction C_2 + OH.

In order to obtain the absolute concentration of CH*, for comparison with the simulations, the measured CH* intensity at shock-tube conditions would require a calibration factor. The calibration of OH* is based on the H_2/O_2 model prediction which is a well validated mechanism. However, this cannot be done with C_2H_2/O_2 mechanism where the uncertainty from the model are very high. Among the three recommended reactions, it is unclear which reaction is important to CH* formation since there are too many degrees of freedom. In addition, the recommended rate of these reactions varies from two to three orders of magnitude. The uncertainty of the ground state C_2H_2- and C_2- chemistry adds to the difficulty. Therefore only a relative comparison of measured intensities and calculated concentrations can be given where the CH* at different stoichiometry and temperatures can be compared. An experiment with C_2H_2/O_2/Ar is performed at three different fuel stoichiometries (ϕ = 0.5, 0.75, and 1.0) [98]. The measured CH* intensity profile normalized to maximum intensity is shown in Fig. 5.8. The figure shows the CH* profile of a C_2H_2(0.1%)-O_2(0.25%)-Ar(99.65%) mixture at ϕ = 1.0 and T_5 = 1961 K initial temperature at pressure 1.28 bar. For comparison, the simulated CH* concentration profile is also plotted which shows very good reproduction of the CH* profile shape and the peak position. Here, the CH* concentration is normalized to its maximum value. In addition the measurement of C_2H_2 with N_2O mixtures is performed in order to possibly isolate the C_2H + O reaction as the O-atom concentration will be in abundance. Whereas in C_2H_2/O_2 mixtures the reaction of C_2H+O_2 could be dominant due to availability of O_2 from the oxidizer. However, the role of the third reaction C_2 + OH is difficult to estimate.

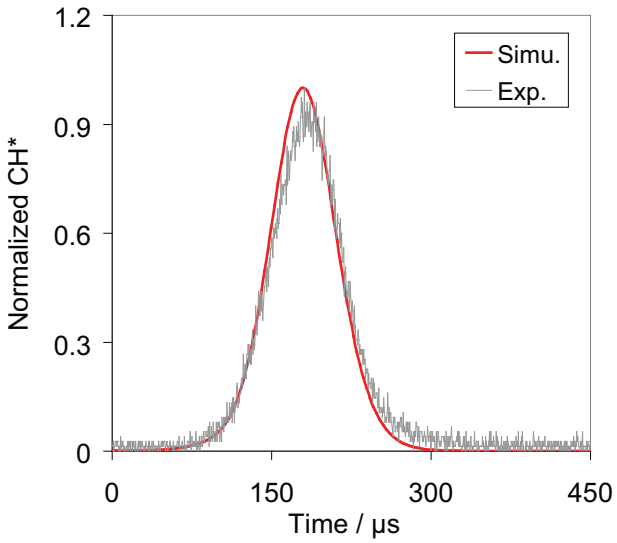

Figure 5.8: A comparison of the measured CH* intensity profile with the calculated concentration profile normalized at its respective maximum value (75 mV, 6.6×10^{-14} mol cm^{-3}). The mixture composition is C_2H_2(0.1%)-O_2(0.25%)-Ar(99.65%) for the fuel stoichiometry of $\phi = 1.0$. The initial mixture is at $T_5 = 1961$ K and at pressure of 1.28 bar.

In lean mixtures and in lower hydrocarbon fuels the amount of ground state C_2 is much less compared to fuel-rich mixtures. Therefore it is possible that the existence of the reaction (R429) is more visible in fuel-rich mixtures where C_2 is in abundance. In the present work, based on the shock-tube experiments performed by [98] in $C_2H_2/O_2/Ar$ and $C_2H_2/N_2O/Ar$ mixtures at different stoichiometries, it is found that the ratio of peak O/O_2 at peak C_2H is low and nearly constant ($\sim$0.01) at different temperatures for the O_2 containing mixtures (Fig. 5.9). Therefore, the possibility of CH* formation from C_2H with O_2 reaction (R427) is likely due to presence of the high amount of O_2 compared to the O-atom concentration at the C_2H peak. However, in N_2O containing mixtures the ratio is much higher (as much as 15) which implies the presence of high amount of O-atoms compared to O_2 at the C_2H peak (Fig. 5.10). Therefore, in this case it is possible to isolate the reaction (R428) from reaction (R427). The peak O/O_2 ratio in $C_2H_2/N_2O/Ar$ mixture has a temperature dependence.

It is possible that in N_2O- containing mixture some more reactions may be responsible for CH* formation e.g. reaction of NH with CO leading to CH* cannot be ruled out. However, no such recommendations have been made so far in the literature. This study,

although it is possible to isolate the two reactions (R427) and (R428) from the O/O_2 ratios by using N_2O and O_2 as oxidizers, is not conclusive to identify the role of reaction (R429).

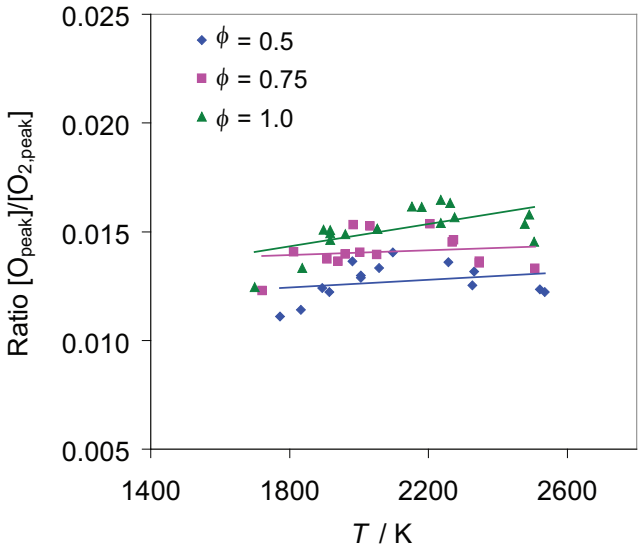

Figure 5.9: Numerical comparison of ratios of the peak values of the O to O_2 concentration for $C_2H_2/O_2/Ar$ mixtures at various temperatures. The simulations are performed for $\phi = 0.5$, 0.75, and 1.0. Lines are linear fit to the data points.

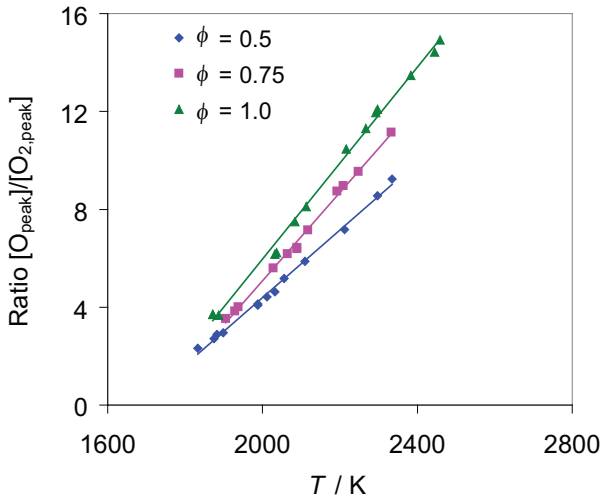

Figure 5.10: Numerical comparison of ratios of the peak values of the O to O_2 concentration for $C_2H_2/N_2O/Ar$ mixtures at various temperatures. The simulations are performed for $\phi = 0.5$, 0.75, and 1.0. Lines are linear fit to the data points.

Based on this shock-tube study it is seen that, the reaction of C_2H with O_2 is important at lean mixture conditions whereas the reaction of C_2H with atomic oxygen is important at stoichiometric and fuel rich conditions were the amount of O_2 at the C_2H peak is much less compared to O. The reaction (R429) is unimportant at lean conditions, and its role at stoichiometric and rich conditions remains unclear.

5.2 Simulations of laminar one-dimensional flame

Laminar flames in premixed and non-premixed conditions are widely studied in the literature. However, there are only few studies dedicated to the measurement of excited species. Among these are the premixed flame studies of Smith et al. [34, 46, 63] who measure the three species OH*, CH*, and C_2* in methane-air flames of varying stoichiometry. Excited species are also measured at non-premixed conditions by De Leo et al. [22]. They measure OH* and CH* in methane and oxygen-enriched air mixtures at varying strain rates. Very recently, Panoutsos et al. [4] study partially premixed and non-premixed methane-air flames and evaluated the equivalence ratio using OH* and CH* chemiluminescence.

5.2.1 Simulations of laminar premixed flame

Prediction of the OH* concentrations

The only measurement of OH* in hydrogen-air premixed flames available in the literature is done by Smith et al. [34]. With our recommended rate coefficient k_{R413} in the mechanism [27], and using experimental temperature profiles as input, the OH* profile shown in Fig. 5.11 is obtained. The shape of the profile is very well predicted by the mechanism. The peak of OH* is 0.9 mm displaced compared to the measurement. It also very well predicts the decay of the OH*-signal. The absolute concentration is about 2.5 times lower than the measurement owing to the fact that the recommended rate is in the range of 1400-2800 K whereas the flame temperature peaks at about 1000 K. As seen earlier, a higher rate would be required at these temperatures.

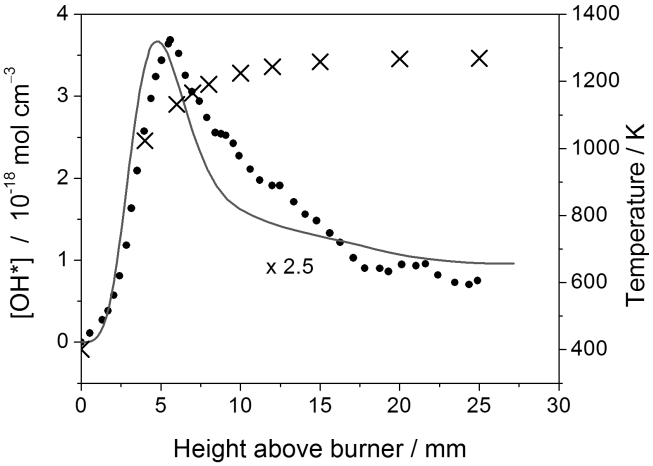

Figure 5.11: Absolute OH* concentration profile as a function of the height above the burner. Conditions: $\phi = 1.54$, pressure 0.05 bar, laminar premixed H_2-air flame. Symbols: experiment from [34] where • is OH* profile and × is temperature profile, line: OH* simulated profile, scaled by a factor of 2.5 [27].

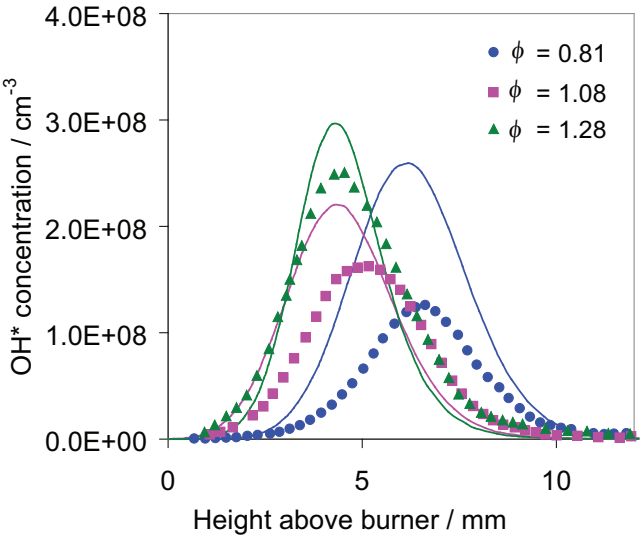

Figure 5.12: The OH* prediction of mechanism with the OH* absolute concentration measured by Smith et al. [63] in methane-air premixed flames. The experiments are performed at three flame conditions ($\phi = 0.81$, 1.08, and 1.28) with measured temperatures as input to the simulation. Symbols: experiment, line: simulation.

Table 5.2: Numerical investigation of OH* formation channel.

Model 1	Model 2	Reaction number	Rate coefficient
H + O + M	H + O + M	(R413)	[27]
$CH + O_2$	$CH + O_2$	(R414)	[63]
CHO + O		(R415)	[2]

Measurement of OH* is also performed in a series of methane-air lean ($\phi = 0.81$), stoichiometric ($\phi = 1.08$) and at rich flames ($\phi = 1.28$) by Smith et al. [46, 63]. In hydrocarbons the major path to OH* is the $CH + O_2$ reaction which leads to OH* formation. The shape and the peak position of OH* profile is well captured by the simulations. As shown in Fig. 5.12, the measured OH* intensities appears to be function of fuel stoichiometry, where OH* increases with an increase in ϕ. However, the simulated profile appears to be different in the lean case.

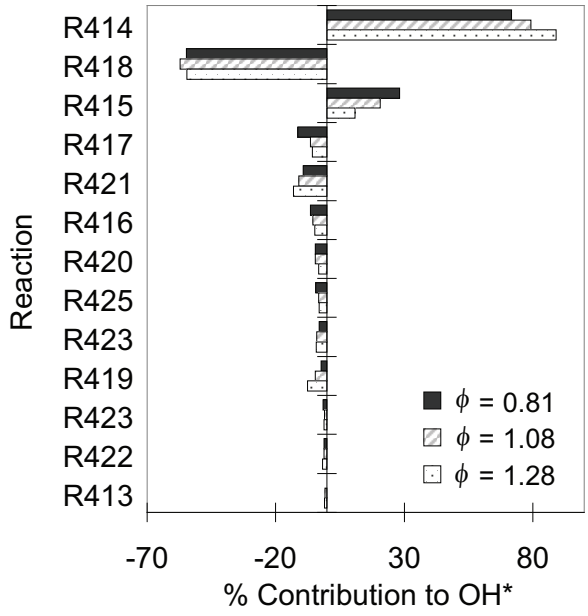

Figure 5.13: A reaction flow analysis of OH* formation and consumption for premixed flame conditions calculated with the three different fuel stoichiometries ($\phi = 0.81$, 1.08, and 1.28) shown in Fig. 5.12. The analysis is performed at peak OH* concentration (6.25 mm ($\phi = 0.81$), 4.5 mm ($\phi = 1.08$), and 4.38 mm ($\phi = 1.28$)).

The proposed reaction of OH* formation in hydrocarbon combustion, is $CH + O_2$ (R414)

but recently the reaction of CHO with O (R415) is proposed [2]. However, its importance to OH* formation has never been discussed. Numerical investigation is performed for CH_4-air flames to reproduce the OH* profiles measured in [63]. Two models are compared, as shown in Table 5.2, with respect to the influence of reaction (R415) on OH* formation. The reaction flow analysis, in Fig. 5.13 shows that at the given rate of reaction recommended in literature, the contribution of reaction (R415) is more in lean condition compared to rich condition. The formation of OH* in lean and stoichiometric condition is 72% and 79% from reaction (R414) and 28% and 21% from reaction (R415) respectively. At rich condition, the formation of OH* from reaction (R414) dominates at 89% and only 11% is formed from reaction (R415). In all cases, the contribution of reaction (R413) is negligible.

The comparison of the OH* profile shape and its peak position obtained with model 1 and model 2 is presented in Fig. 5.14. The OH* profiles resulting from model 1 are narrower than those from model 2. Since the maximum contribution of reaction (R415) to OH* formation is seen at lean condition, the difference in both model profile shape and peak position is prominently seen in Fig. 5.14a. The OH* profile is broader with addition of reaction (R415) to the mechanism and is closer to the experiment. The effect of reaction (R415) is less visible in stoichiometric and rich condition as its contribution reduces. This shows that, with reaction (R414) the only formation reaction in the mechanism (model 1), the peak positions in lean to stoichiometric cases are not reproduced by the simulations when compared to the measurements. As shown in Fig. 5.14 they peak closer to the burner surface. At lean condition, the OH* in the simulation is 0.7 mm away from the experimental peak and is consumed faster than the experimental profile. The profile peaks closer to the experiment with addition of reaction (R415) to the mechanism.

The above investigation supports the contribution of reaction (R415) to the OH* formation and the rate coefficients of reaction (R414) and (R415) need to be reinvestigated.

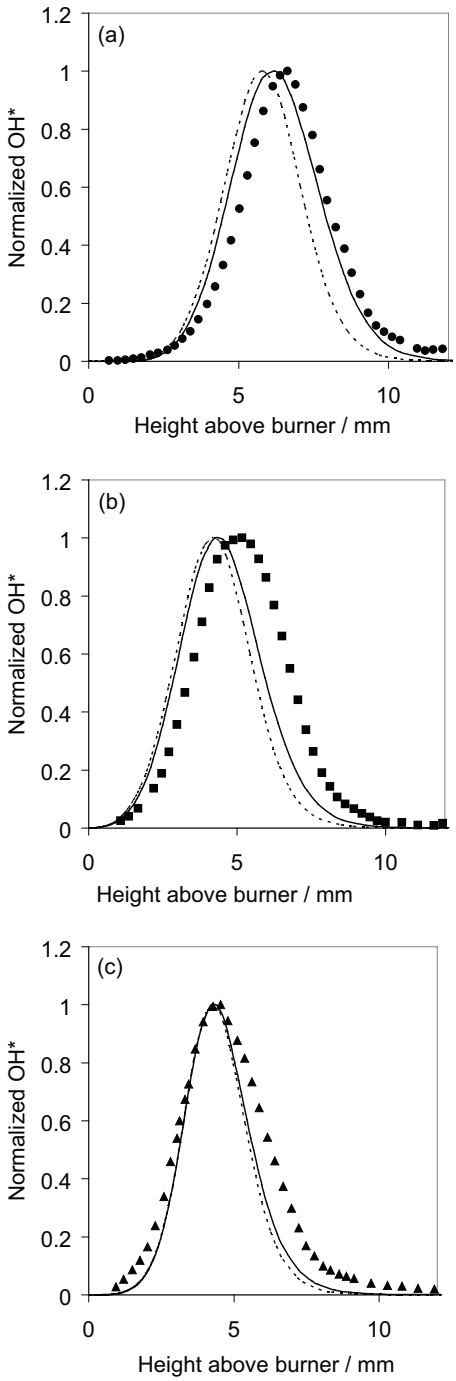

Figure 5.14: A comparison of OH* absolute concentration with reactions CH + O_2 (R414) (dashed line), and CH + O_2 (R414) plus CHO + O (R415) (continuous line) in the simulations. The experiments are performed at (a) lean (ϕ = 0.81), (b) stoichiometric (ϕ = 1.08), and (c) rich flame condition (ϕ = 1.28). Symbols: experiment.

A sensitivity analysis is performed at the position from burner axis where the concentration of OH* reaches its maximum (Fig. 5.15). The respective profile is shown in Fig. 5.12. For $\phi = 0.81$, 1.08, and 1.28 at distance from burner surface 6.25 mm, 4.5 mm, and 4.38 mm respectively. As expected the maximum positive sensitivity is from the OH* formation reactions (R414) and (R415). The major OH* consumption channel is OH* + $H_2O \rightarrow$ OH + H_2O (R418) and OH* + $O_2 \rightarrow$ OH + O_2 (R417) and it therefore has maximum negative sensitivity. In addition to this, the reactions which are involved in the production (/consumption) of the precursors of OH* (ie. CH, CHO) have positive (/negative) sensitivity. Reactions that have a high positive sensitivity are: CH_3 + OH $\rightarrow {}^1CH_2 + H_2O$ (R68), ${}^1CH_2$ + M $\rightarrow {}^3CH_2$ + M (R49), ${}^3CH_2$ + H $\rightarrow$ CH + H_2 (R41), and CH + $H_2O \rightarrow {}^3CH_2$ + OH (R33) which are reaction channels of CH and CHO. The reactions CH + H $\rightarrow$ C + H_2 (R25), CH_3 + O $\rightarrow CH_2O$ + H (R66) , CH + $O_2 \rightarrow$ CHO + O (R29), ${}^1CH_2 + O_2 \rightarrow$ CO + OH + H (R51), and CHO + M $\rightarrow$ CO + OH + H (R34) have negative sensitivity.

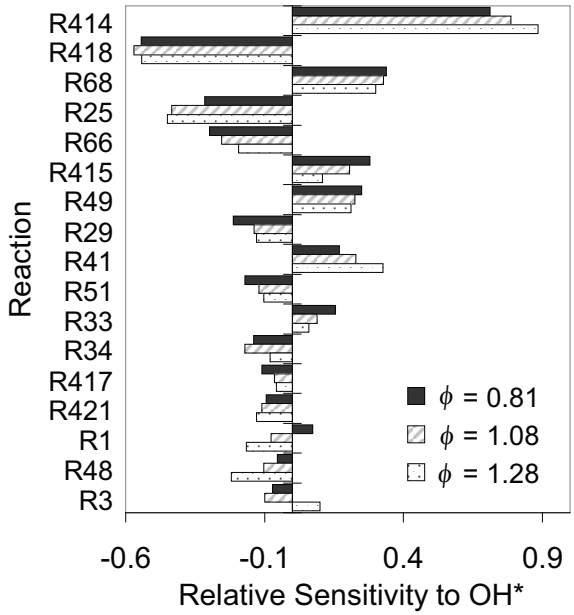

Figure 5.15: A sensitivity analysis with respect to the OH* formation and consumption for three different fuel stoichiometry ($\phi = 0.81$, 1.08, and 1.28) is performed for the premixed flame shown in figure 5.12. The analysis is performed at peak OH* concentration (6.25 mm ($\phi = 0.81$), 4.5 mm ($\phi = 1.08$), 4.38 mm ($\phi = 1.28$)).

Very recent experiments measuring excited species such as OH*, CH(A), CH(B) and C_2* are performed in [100] for laminar premixed CH_4-O_2-Ar flames. The flame is measured

at six different fuel stoichiometries (see Table 5.3). The lean to rich (ϕ = 0.5, 1.0, 1.2, 1.4, 1.5, and 1.6) methane flames are measured at a low pressure of 0.05 bar stabilized on a Mckenna burner (burner diameter 63 mm). In addition to this, these flames are diluted with additional H_2 to see its effect on chemiluminescence. The inlet flows of these CH_4-H_2-O_2-Ar flames are summarized in Table 5.4. The CH_4-H_2-O_2-Ar flames are measured for stoichiometric (ϕ = 1.0) and rich (ϕ = 1.5) flame condition with H_2 dilution ranging from 10 to 50%. The flame temperatures are measured via NO-LIF and are input to the simulations.

Table 5.3: Experimental condition of CH_4-O_2-Ar flame measured at 0.05 bar on a Mckenna burner [100]. The measured flowrate is given in Standard Liters per Minute (slm).

ϕ	CH_4 (slm)	O_2 (slm)	Ar (slm)
0.5	0.66	2.65	1.1
1.0	1.10	2.21	1.1
1.2	1.24	2.07	1.1
1.4	1.36	1.95	1.1
1.5	1.42	1.89	1.1
1.6	1.47	1.84	1.1

Table 5.4: Experimental condition of CH_4-H_2-O_2-Ar flame measured at 0.05 bar on a Mckenna burner [100]. The measured flowrate is given in Standard Liters per Minute (slm).

ϕ	H_2 (%)	CH_4 (slm)	H_2 (slm)	O_2 (slm)	Ar (slm)
1.0	10	1.04	0.12	2.15	1.1
	20	0.98	0.25	2.08	1.1
	30	0.91	0.39	2.01	1.1
	50	0.74	0.74	1.84	1.1
1.5	10	1.33	0.15	1.83	1.1
	20	1.24	0.31	1.76	1.1
	30	1.14	0.49	1.68	1.1
	50	0.90	0.90	1.50	1.1

The measured excited species intensities are compared with the simulated mole fractions. Although a direct comparison is not possible, the relative comparison of OH* peak intensity at different stoichiometry can be done with relative peak OH* mole fraction.

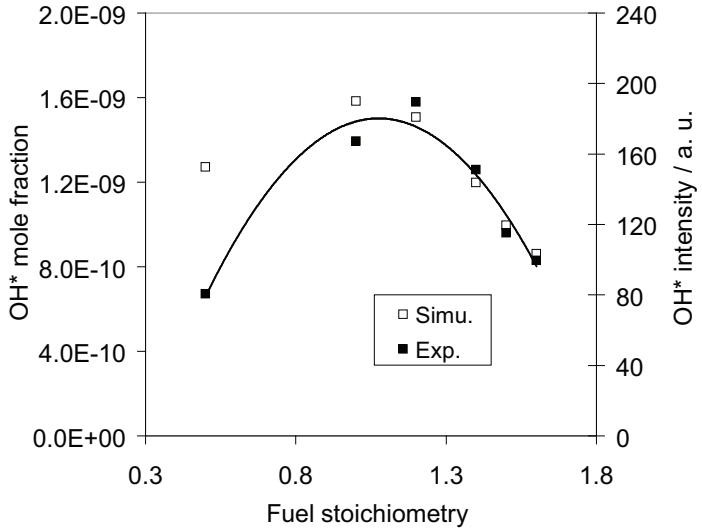

Figure 5.16: Relative comparison of the measured OH* peak intensity and calculated OH* peak mole fraction at different fuel stoichiometries. The premixed CH_4-O_2-Ar flame conditions are listed in Table 5.3. Open symbols: experiments, closed symbols: simulations, and line: polynomial fit to the experimental data points.

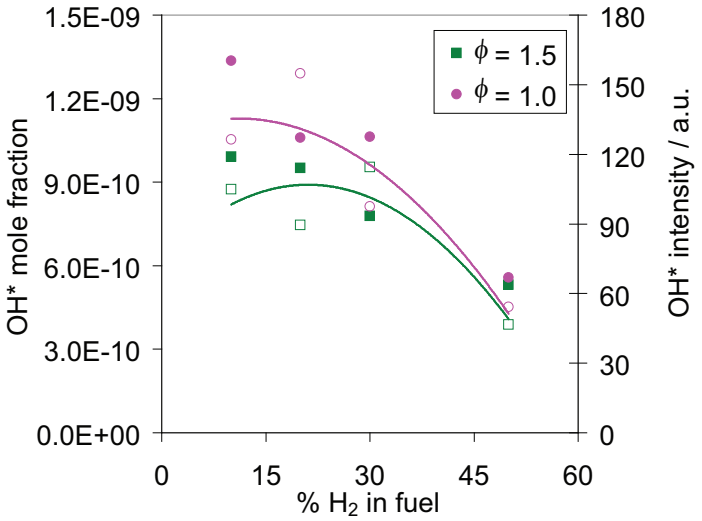

Figure 5.17: The measured OH* peak intensity and calculated OH* peak mole fraction compared at different H_2 content in fuel for $\phi = 1.0$ and 1.5. The premixed CH_4-H_2-O_2-Ar flame conditions are listed in Table 5.4. Open symbols: experiment, closed symbols: simulations, lines: polynomial fit to the experimental data points.

As shown in Fig. 5.16, except at $\phi = 0.5$, the relative intensities are in very good agreement with the calculated mole fractions.

The results from the four different flames measured for CH_4-H_2-O_2-Ar flames at $\phi =$ 1.0 and 1.5 are shown in Fig 5.17. At both fuel stoichiometries, the OH* concentration decreases with an increase in the H_2 content from 10 to 50 %. By looking at CH concentration at OH* peak, it is seen that the CH peak concentration decreases with increase in H_2% in fuel. Since CH is the direct precursor to the OH* formation, its decrease in concentration directly influences the OH* concentration.

Prediction of CH* concentrations

The only CH* measurement done in laminar premixed flame conditions are from Smith et al. [63]. As discussed earlier, the simulations of CH* formation and consumption are rather difficult as it is unclear through which reaction it is formed. They measure CH* in methane-air flames at lean, stoichiometric and rich condition. The measured CH* intensity increases as the flame gets richer. The major species forming CH* is C_2H (R427), (R428) and as mentioned in [63] its model uncertainty can be more than $\pm$50%. This uncertainty directly translates to uncertainties in the prediction of CH*. In addition to this, there is a channel which forms CH* from C_2 (R429). So far there are only few mechanisms which are capable of predicting C_2 concentration [46,93]. Therefore the accurate prediction of CH* is very challenging.

A reaction flow analysis is performed for the above condition of Smith et al. with all the three formation reactions of CH* in the mechanism. Figure 5.18 shows such comparison at lean, stoichiometric and rich flame conditions at the distance from the burner where CH* peaks i.e., at z = 7.25 mm, 5.75 mm and 5.25 mm respectively. The CH* in lean condition is formed about 40% in the reactions (R427) and (R428) and with a minor contribution from (R429). In stoichiometric and rich condition the later reaction (R429) becomes important with the other two reactions having only a limited contribution. The major consumption channels are reactions of OH* with N_2 and H_2O at all three conditions.

A sensitivity analysis with respect to CH* formation and consumption is performed for the premixed flame condition shown in Fig. 5.20. The analysis is presented in Fig.

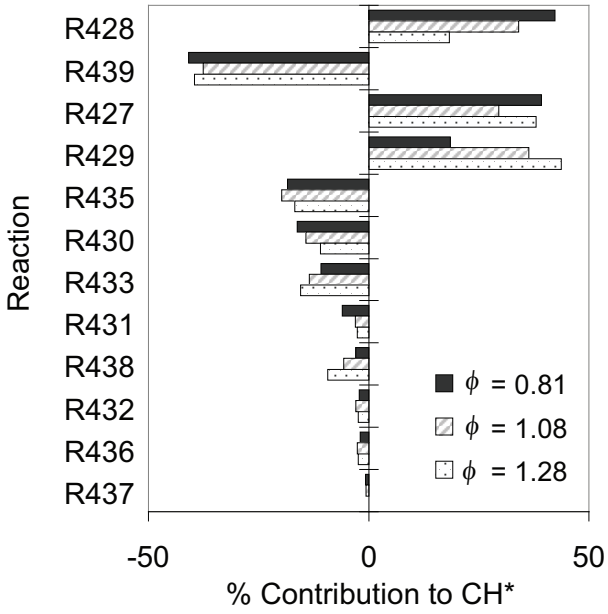

Figure 5.18: A reaction flow analysis of CH* formation and consumption for the premixed flame condition calculated with three different fuel stoichiometries (ϕ = 0.81, 1.08, and 1.28) shown in Fig. 5.20. The analysis is performed at the peak CH* concentration: 7.25 mm (ϕ = 0.81), 5.75 mm (ϕ = 1.08), 5.25 mm (ϕ = 1.28).

5.19, where the normalized sensitivity coefficients are calculated at CH* peak position of 7.25 mm (ϕ = 0.81), 5.75 mm (ϕ = 1.08), 5.25 mm (ϕ = 1.28). The major sensitive reactions, apart from the CH* formation and consumption reactions which is apparent, are the ones that plays important role in C_2H_2 consumption channel. The maximum negative sensitivity is from the most important chain branching reaction $O_2 + H \rightarrow OH + O$ (R1) which is an important source of O atoms in reaction (R428). However, (R1) is not as sensitive under rich condition as it is with lean and stoichiometric cases. This is due to the fact that (R428) is not a key reaction at rich condition (see Fig. 5.18). Another important reaction with negative sensitivity is $C_2H_2 + O \rightarrow HCCO + H$ (R128) for all three fuel conditions. Other than the CH* formation reactions, the reaction $C_2H_4 + M \rightarrow C_2H_2 + H_2 + M$ and other acetylene consumption reactions have positive sensitivity. In addition to the acetylene sub-mechanism, reactions consuming C_3 to form C_2 and C_2H have little sensitivity.

However, these analysis is highly dependent on the reaction rates of these formation channels and does therefore not give any information on important CH* reaction.

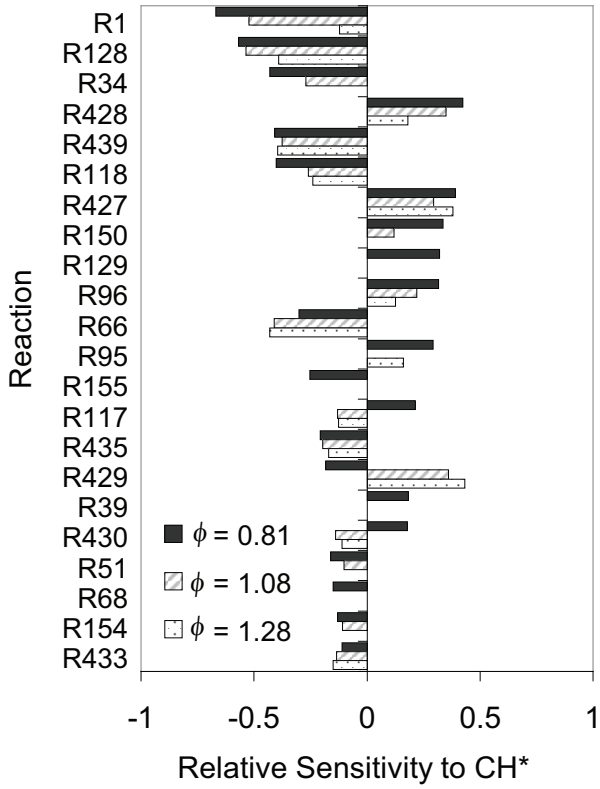

Figure 5.19: A sensitivity analysis with respect to CH* formation and consumption for three different fuel stoichiometries (ϕ = 0.81, 1.08, 1.28) is performed for the premixed flame shown in Fig. 5.20. The analysis is performed at the peak CH* concentration: 7.25 mm (ϕ = 0.81), 5.75 mm (ϕ = 1.08), 5.25 mm (ϕ = 1.28).

When the reaction of $C_2H + O_2$ is in the mechanism, the CH* in lean flames is predicted very well with respect to the absolute concentration, peak position, and shape of the profile. However, in stoichiometric and rich case it is underpredicted by a factor of about 0.5. Therefore, in the later two cases, the other two reactions are also important. Taking only C_2 + OH (R429) reaction into account, results in an underprediction of the CH* concentration by a factor of 3.5 to 6.5 when fuel composition is varied from lean to rich condition. And with this reaction in the mechanism, the profile of the calculated CH* appears much later than measured CH* (lean condition) whereas in rich case it precedes the measurement. This explains that CH* at lean condition is formed much earlier than C_2 is formed and therefore reactions (R427) and (R428) are the likely source of CH* in

addition to the fact that C_2 concentrations are very little in lean mixtures. An analysis with these three reactions and their rate coefficients showed that better agreement with measured absolute concentration, shape of profile, and distance from burner is obtained when (R427) is the only formation reaction in lean case whereas in stoichiometric and rich conditions both reaction (R428) and (R429) are included in the mechanism. The reported estimated measurement uncertainty of the CH* absolute concentration is about 35%.

At lean conditions, a good fit to the measurements is obtained when it is assumed that only reaction $C_2H + O_2$ is forming OH*. The rate coefficient suggested by Elsamra [88] ($k = 6.02\times10^{-4}T^{4.4}$ $cm^3mol^{-1}s^{-1}$ $\exp(9.6\ R^{-1}T^{-1}$ $kJmol^{-1})$ overpredicts CH* by factor of eight and therefore a good fit is obtained with k lowered by factor of eight. Otherwise with (R428) and (R429) in the mechanism, the shape and peak position of CH* profile no longer fits the measurements. In addition, it is seen that at CH* peak there is more O_2 available to react via (R427) compared to O atoms which is formed later in the flame. This supports that the reaction (R427) is a major source of CH* as the CH* profile obtained by (R428) is shifted away from the burner compared to the measurement. And since there is nearly no C_2 formed in lean flames, it rules out the possibility of reaction (R429) as a possible source of CH* in lean methane-air flames.

At stoichiometric condition, the amount of fuel increases compared to the amount of oxidizer in lean case, therefore it is naturally assumed that less O_2 is available for CH* via reaction (R427). On the other hand, at the position where CH* peaks, sufficient amount of O-atoms has been formed (60% of total O-atoms formed) whereas O_2 is 80% consumed. The amount of C_2 is about an order less compared to the rich case. Therefore, the most likely source of CH* in stoichiometric mixtures is reaction (R428). It is seen that the shape of CH* profile fits to the measurement very well. With the reaction rate suggested by [63] in the mechanism, CH* is overpredicted by a factor of 2.

In rich flames, only 10% of the O_2 is left in the reaction mixture at the position of the CH* peak. However sufficient amount of O atoms and C_2 concentrations are available to react and form CH*. With reaction (R428) in the mechanism, the CH* peak concentration is underpredicted by factor of 1.3. Therefore, it is assumed that the rest of the CH* is formed in the reaction (R429). It is seen that with these two reactions in the mechanism, the shape and position of the CH* profile is very well reproduced compared to the experiments. The reaction rates of these two reactions suggested by [63] are modified,

Table 5.5: Reaction channels of CH* formation and their rate coefficient that best fits the experiments from [63].

CH*-model	Reaction no.	Rate coefficient k	Reference (×factor multiplied to k)
Lean	(R427)	$7.5{\cdot}10^{-5}\,T^{4.4}\exp(9.6/RT)$	[88](×1/8)
Stoic	(R428)	$6.25{\cdot}10^{11}$	[34] (×1/4)
	(R429)	$4.4{\cdot}10^{13}$	[63] (×4)
Rich	(R428)	$6.25{\cdot}10^{11}$	[34] (×1/4)
	(R429)	$4.4{\cdot}10^{13}$	[63] (×4)

where (R428) is reduced and (R429) is increased by factor of 4, to obtain a better agreement of the CH* concentrations in the stoichiometric and rich flame. Table 5.5 summarizes information on the CH* formation reactions and their rate which provide best fit to the CH* experiments shown in Fig. 5.20.

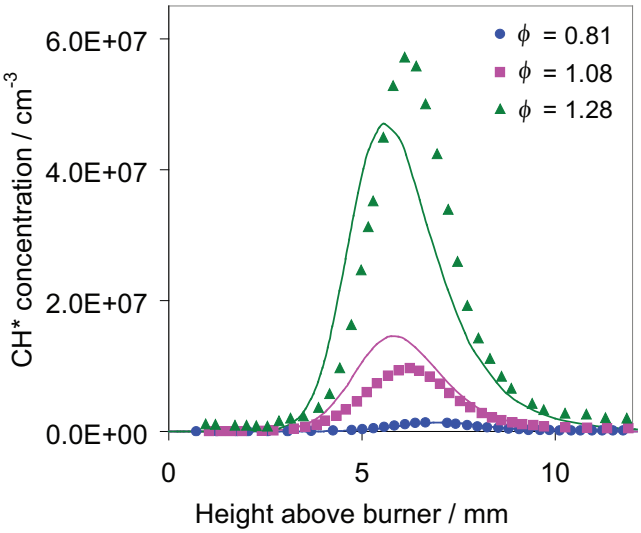

Figure 5.20: A burner stabilized premixed flame calculated with three different fuel stoichiometries. The simulated CH* concentrations are compared with the measurements done by [63] at low pressures (0.33 bar ($\phi = 0.81$, 1.08) and 0.04 bar ($\phi = 1.28$)).

The measurement of CH(A) and for the first time CH(B) is performed by [100] for the conditions presented in Table 5.3. A relative comparison of peak CH* intensities and simulated CH* mole fractions at six fuel stoichiometries is presented in Figs. 5.21-5.24.

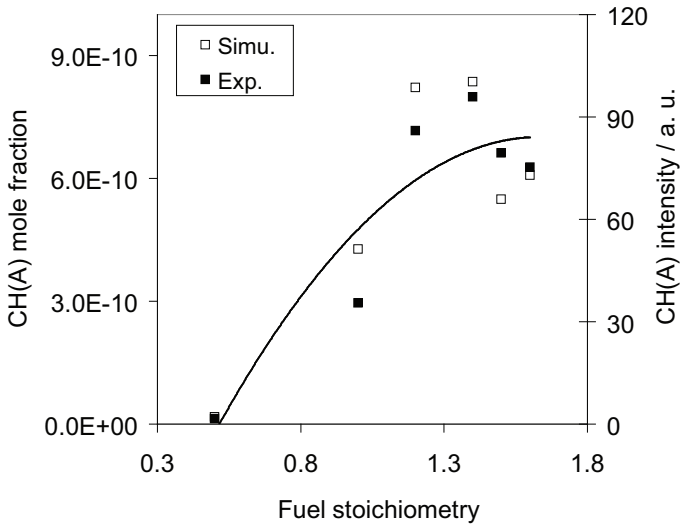

Figure 5.21: Relative comparison of CH(A) peak measured intensity and CH(A) peak mole fraction at different fuel stoichiometries. The premixed CH_4-O_2-Ar flame conditions are as presented in Table 5.3. Open symbols: experiments, closed symbols: simulations, and line: polynomial fit to the experiments.

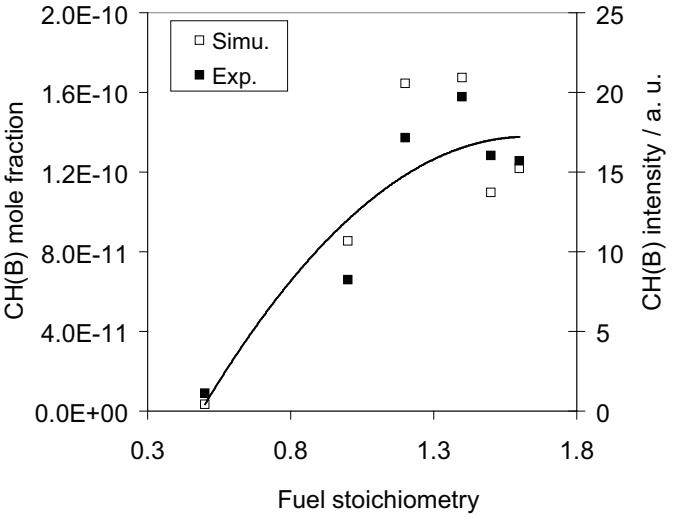

Figure 5.22: Relative comparison of CH(B) peak measured intensity and CH(B) peak mole fraction at different fuel stoichiometries. The premixed CH_4-O_2-Ar flame conditions are as presented in Table 5.3. Open symbols: experiments, closed symbols: simulations, and line: polynomial fit to the experimental data point.

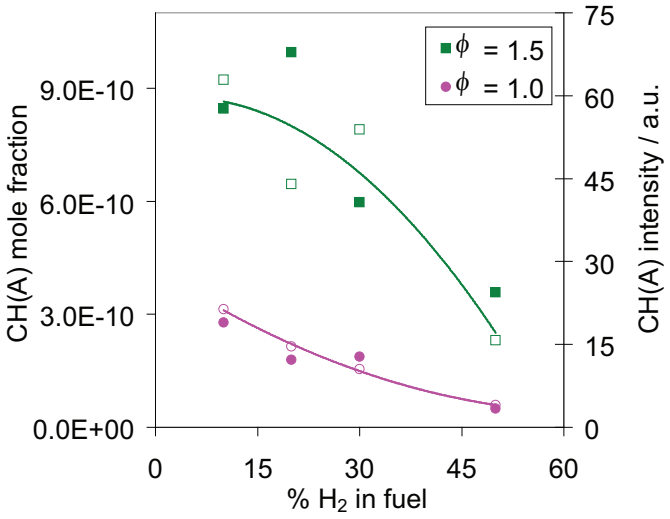

Figure 5.23: The measured CH(A) peak intensity and calculated CH(A) peak mole fraction compared at different H_2 percentage in fuel and at $\phi = 1.0$ and 1.5. The premixed CH_4-H_2-O_2-Ar flame conditions are listed in Table 5.4. Open symbols: experiments, closed symbols: simulations and lines: polynomial fit to the experiments.

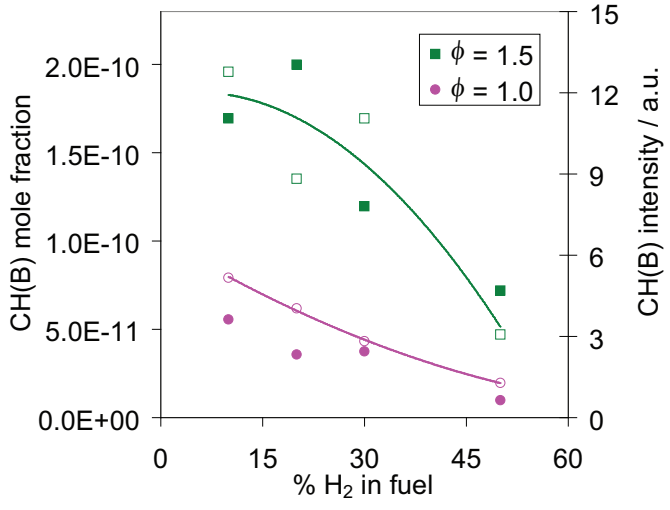

Figure 5.24: The measured CH(B) peak intensity and calculated CH(B) peak mole fraction compared at different H_2 content in fuel and at $\phi = 1.0$ and 1.5. The premixed CH_4-H_2-O_2-Ar flame conditions are listed in Table 5.4. Open symbols: experiments, closed symbols: simulation, and lines: polynomial fit to the experimental data points.

About 80% of total CH* chemiluminescence seen in the flames is from CH(A) state whereas rest 20% is from CH(B) state. This is apparent from the measured CH* intensities (Figs. 5.21 and 5.22), where at given stoichiometry, the measured CH(B) intensity is 5 times lower than the CH(A) states.

There is no recommendation of CH(B) state reaction rates in literature. Therefore for CH(B) state, 20% of k used for CH* is considered in the simulations. Also the information on radiative decay and quenching reaction rates is still unknown and therefore, the rate same as CH(A) are considered in the mechanism. As seen in Figs. 5.21 and 5.22, the general trend of measured intensity at different ϕ is reproduced by the simulations in both cases. However, the CH(B) state reaction rates shall require further improvement with respect to its consumption channel.

In addition, the measurement done for CH_4-O_2-Ar flame diluted with hydrogen is shown in Fig. 5.24. Here, the H_2 content in flame varies from 10 to 50 % in the fuel (see Table. 5.4). CH(A) concentrations at $\phi = 1.5$ are about 3 times higher than at stoichiometric condition (Fig. 5.24). With increase in H_2 content, the CH* (-A and -B states) intensities decrease as the carbon content in the fuel decreases. For both CH(A) and CH(B) cases, this experimental trend of the CH* intensity against H_2 content is reproduced by the calculated concentrations.

Prediction of C_2* concentrations

Only few measurements on C_2* chemiluminescence have been done. This includes the measurement of a premixed methane-air laminar flame by [63]. Later the same group studied stoichiometric and rich ethane- and ethylene- air flames [46]. The profiles of C_2* for the stoichiometric and rich methane-air flame, as shown in Fig. 5.25, are in good agreement with the measurement. The shape of the simulated rich profile matches very well with the measurement. However, in the stoichiometric case it slightly precedes the measurement. With the recommended reactions and their rates in the mechanism, the absolute value of C_2* in both stoichiometric and rich cases are in agreement with the measurements.

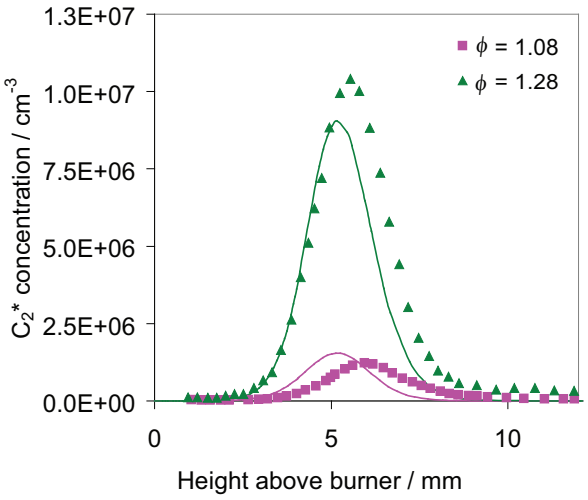

Figure 5.25: A comparison of C_2* absolute concentration measured by Smith et al. [63] with the simulations. The experiments are performed at stoichiometric ($\phi = 1.08$) and rich flame condition ($\phi = 1.28$). Symbols: experiment, line: simulation.

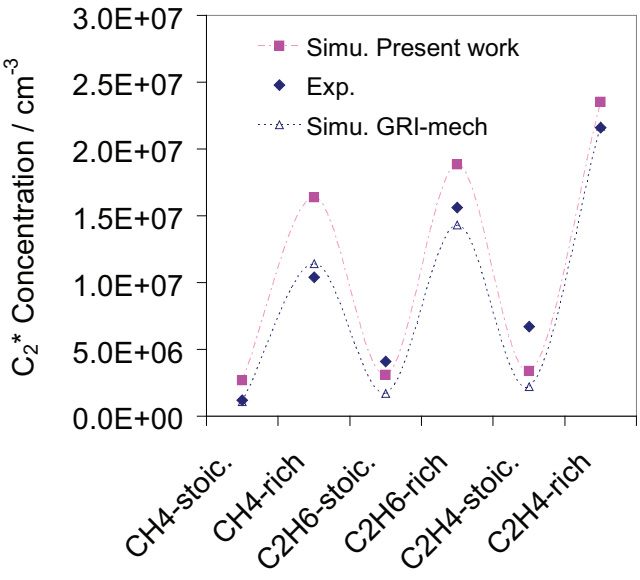

Figure 5.26: A comparison of peak C_2* absolute concentration measured by Smith et al. [63] with the simulations. The experiments are performed at stoichiometric ($\phi = 1.08$) and rich flame condition ($\phi = 1.28$). Symbols: experiment, line: simulation.

The peak C_2* measured in stoichiometric and rich ethane- and ethylene- flames are compared against the simulations in Fig. 5.26 where it shows that there is underprediction of C_2* in these flames by factor of two to three. However, in stoichiometric and rich methane-air flame, the predictions are comparable to the measurements.

In addition, the C_2* concentration in CH_4-O_2-Ar flames at 0.05 bar and $\phi = 0.5$ to 1.6 is measured (Table 5.3). The relative comparison of the peak C_2* measured intensity and the calculated mole fractions is shown in Fig. 5.27. As seen, the calculated mole fractions and measured intensities are in very good agreement at the given fuel stoichiometries. Similarly, for CH_4 mixtures containing H_2, the trend of measured intensity and calculated concentration at given H_2% in fuel is very well reproduced (shown in Fig. 5.28). The C_2* intensity decreases with fuel dilution with hydrogen. The C_2* concentrations at rich condition ($\phi = 1.5$) are about an order of magnitude larger than those found at stoichiometric condition ($\phi = 1.0$).

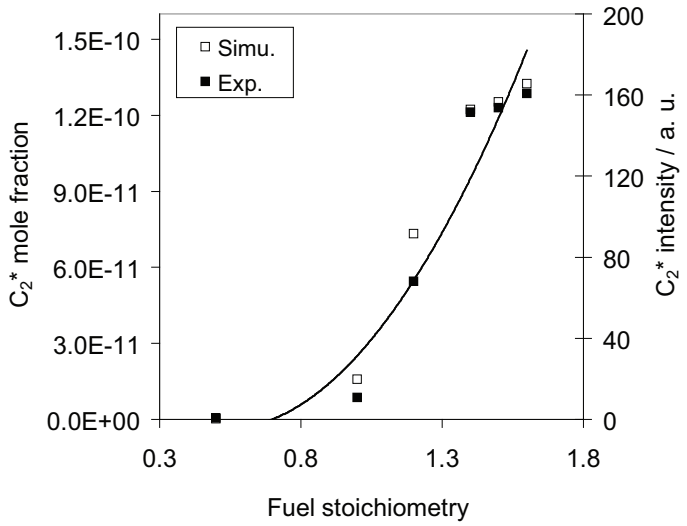

Figure 5.27: Relative comparison of C_2* peak measured intensity and C_2* peak mole fraction at different fuel stoichiometries. The premixed CH_4-O_2-Ar flame conditions are as presented in Table 5.3. Open symbols: experiments, closed symbols: simulations, and line: polynomial fit to the experimental data points.

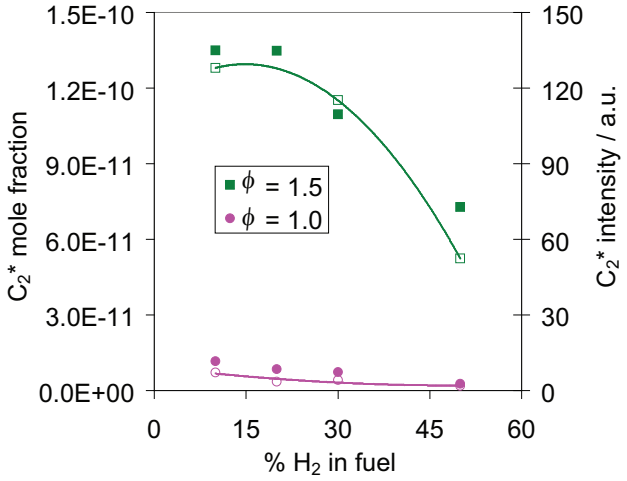

Figure 5.28: The measured C_2* peak intensity and calculated CH_2* peak mole fraction compared at different H_2 content in fuel and at $\phi = 1.0$ and 1.5. The premixed CH_4-H_2-O_2-Ar flame conditions are listed in Table 5.4. Open symbols: experiments, closed symbols: simulations, and lines: polynomial fit to the experimental data points.

5.2.2 Chemiluminescence as a heat release marker

Chemiluminating species are considered as important intermediates that characterize the reaction zone due to their appearance in the flame front and are a potential marker for the heat release and the reaction zone in combustion systems [4, 6, 11, 12]. So in order to get a more detailed picture on the potential of excited species as a heat release marker, a comparison of displacement of peak excited species location from the peak heat release location has been done [5]. A numerical experiment is performed in a premixed methane-air-flame with fuel stoichiometry from lean ($\phi = 0.5$) to rich ($\phi = 1.6$). The methane-air mixtures are at 298 K initial temperature and one bar pressure.

Figure 5.29 shows the location of the peak heat release and peak species mole fractions plotted for different fuel equivalence ratios of CH_4-air mixtures. It is known from the literature that the appearance of formaldehyde (CH_2O) is comparable to that of the peak heat release location. Its concentration product with OH ($[CH_2O][OH]$) is also considered as an important marker for the heat release [6]. Therefore, in Fig. 5.29, the location of CH_2O and $[CH_2O][OH]$ are also shown in addition to the peak location of excited species and heat release. The appearance of formaldehyde is found closest

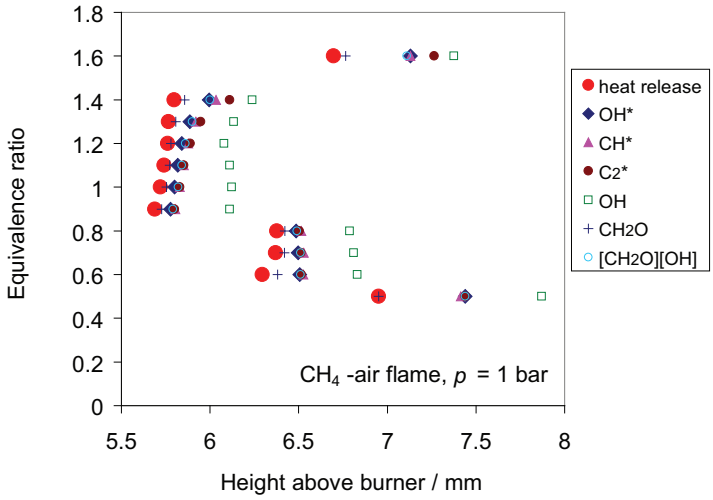

Figure 5.29: Comparison of the location of peak heat release with the location of peak excited species and important ground state species at different fuel stoichiometries. The calculation is done for CH_4/air flame at 1 bar.

to the heat release location. The location of peak CH_2O is closely followed by the OH* location. The appearance of $[CH_2O][OH]$ product concentration and CH* and C_2* chemiluminescence is found at the same displacement from the heat release location. The maximum deviation of species and heat release are found at very lean ($\phi = 0.5$) and rich ($\phi = 1.6$) fuel conditions. In the intermediate fuel stoichiometries ($\phi = 0.7$ to 1.3), the maximum deviation of excited species from the heat release location is about 0.13 mm (OH*), 0.16 mm (CH*), and 0.18 mm (C_2*).

The distance between the peak excited species and heat release location are plotted in Fig. 5.30. The displacement between heat release and excited species location is minimal at near stoichiometric flames. At lower ($\phi < 0.6$) and at higher ($\phi > 1.6$) equivalence ratios, the displacement increases. The maximum of which is ∼0.47 mm for OH* (also CH* and C_2*) at $\phi = 0.5$ and $\phi = 1.6$. The trend of such variation in displacement with fuel stoichiometry is due to the change in reaction zone thickness.

From this numerical study it can be seen that OH* is closest to the peak heat release location and gives results similar to the concentration product of $[CH_2O][OH]$. Although CH_2O is the species that is closer than the OH*, its online measurement will require sophisticated excitation techniques for detection. On the other hand, chemiluminescence emission can be detected by simple optical detection setup. The difference in location

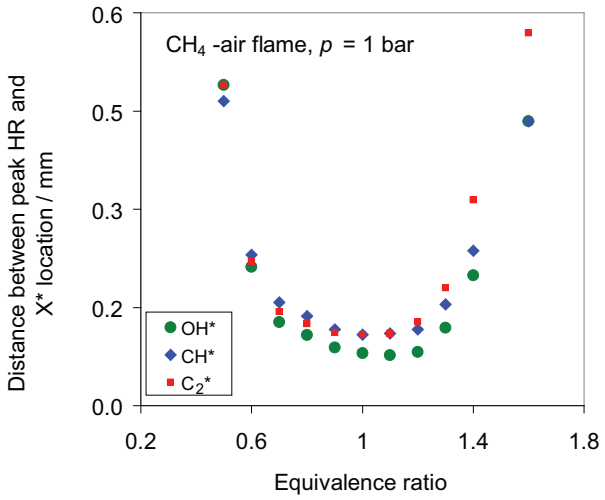

Figure 5.30: Distance between the peak X* (OH*, CH*, and C_2*) and the peak heat release (HR) location plotted against equivalence ratio in methane-air flames.

of CH* is not significant from OH* (about 0.03 mm) and therefore can also be used as heat release marker. The position of C_2* appears nearly at same location as CH* except at very lean ($\phi < 0.8$) condition and at $\phi > 1.3$ where C_2* appears much later in the flame. At lean conditions ($\phi < 0.8$) the concentration of C_2* is negligible ($< 10^{-16}$) at atmospheric and at high pressure. Therefore, C_2* peak position at such conditions is not suitable as heat release marker. The difference in OH* and CH* positions (and C_2* at intermediate stoichiometries) from the peak heat release location are relatively small compared to the resolution of measurement techniques (few mms for laboratory flame). This, results indicates OH* and CH* as important potential markers for the heat release zone.

5.2.3 Simulations of laminar non-premixed flames

In the counterflow diffusion flame, the mixture composition varies from pure oxidizer to pure fuel. Therefore, it provides the advantage of validating the reaction kinetics at varying mixture composition within a single experiment. De Leo et al. [22] studied chemiluminescence of OH* and CH* in opposed-flow methane oxygen-enriched air diffusion flames. They reported the comparison of measured absolute intensities to the numerical model results. The earlier works on diffusion flame were restricted to the

qualitative results however De Leo and coworkers provided for the first time the absolute concentrations of these species. They measured flames varying in O_2 content in oxidizer from 21 - 100%, with a global strain rate maintained in the range of 20 - 40 s^{-1}. The overall uncertainty to the concentration measurement is reported to be ±18%. The maximum temperature (translation temperature of reacting gas) in their flame is about 2900 K where thermal excitation plays important role in OH* and CH* formation rather than chemical excitation. Therefore the OH* and CH* concentrations are formed from the ground state OH and CH. In chemical excitation the ground state OH and CH are not involved rather the reactions (R414), (R415), (R427), (R428), and (R429) are important. The CH* is formed in the part of flame where the hydrocarbon concentration is high, whereas the OH* is formed in the lean (oxygen-rich) zone. With increased O_2-content of the air, the OH* profile becomes wider whereas CH* is unaffected.

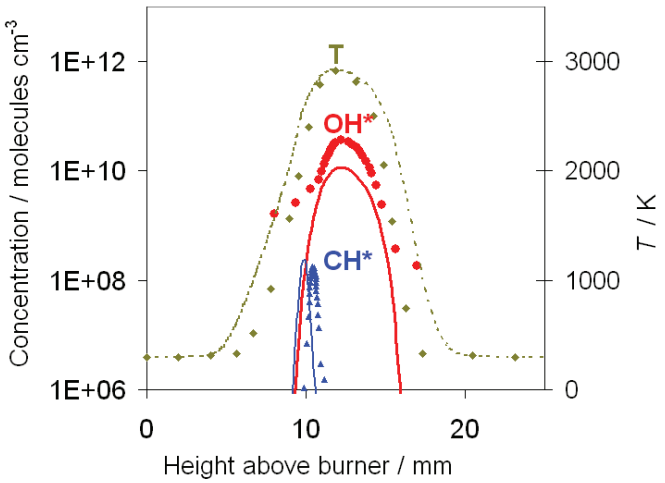

Figure 5.31: Comparison of experimental and simulated OH* and CH* concentrations in methane-oxy diffusion flames (O_2 = 20%). The experiments are performed at strain rate of 20 s^{-1} by De Leo et al. [22]. The temperature profiles are calculated from the energy balance equation. Symbols: experiments (except for temperature which are simulated profile presented in [22]), line: simulation.

Figure 5.31 shows comparison of measured and simulated OH* and CH* profiles and simulated temperatures. Since the flame temperature is about 2900 K, the OH* and CH* are formed from ground state OH and CH respectively and therefore provides validation of these ground state species.

6 Conclusion

In this work, a reaction mechanism to predict chemiluminescent species by modeling and numerical simulation has been developed. The developed mechanism is validated against experimental species profiles. Numerical simulations of chemiluminescent species concentrations in shock-tubes and in laminar flame conditions have been presented and compared to experiments.

This work is comprised of three parts. (1) Modification of a basic hydrocarbon mechanism, with respect to acetylene chemistry and important ground state species concentration (e.g. CH, and C_2H), (2) Addition of a sub-mechanism predicting ground state C_2, and (3) Addition of a chemiluminescence sub-mechanism.

A hydrocarbon reaction mechanism developed earlier that simulates the oxidation of C_1-C_4 hydrocarbon fuels is the starting point of this work. The major limitation of the base mechanism is its prediction of acetylene ignition delay times that are about two orders of magnitude lower than measurements. Acetylene is the main precursor to the formation of all chemiluminescent species. Therefore, the base mechanism is reinvestigated for its prediction of acetylene chemistry. The reactions sensitive to the C_2H_2 ignition delay time and flame velocity are identified and their rate coefficients are modified within the limits of rate data available in literature. In addition to this, it is seen that the prediction of the chemiluminescent species depends strongly on the species that are direct precursors to its formation (i.e. CH, C_2H, and $^1CH_2$). These species are not important for the global validation (e.g. ignition delay time, flame velocity) of the base mechanism, however they are important for chemiluminescence sub-model in the mechanism. Therefore necessary modifications in the base mechanism are done to achieve correct prediction of such precursors. Sufficient amount of experimental flame concentration measurement of CH, C_2H, and $^1CH_2$ is available in the literature. Validation of these species concentrations is done at different fuel stoichiometries and good agreement with measurements is found.

The formation of chemiluminescent species also depends on additional species such as C_2, C_3 which are not part of any existing reaction mechanisms predicting fuel oxidation. Therefore, a sub-mechanism predicting such C-containing species is added to the base mechanism in the second part. These species, due to their low concentration, are difficult to measure experimentally. For their validation not many experiments are available in literature until recently measured C_2 in methane and propene flames. This sub-mechanism is validated for its prediction of C_2 in methane and other hydrocarbon flames where the C_2 concentrations are about twice overpredicted compared to the measurements. The rate coefficients of most of reactions forming and consuming these species are estimates based on similar reactions. Therefore, the twice overprediction of C_2 is likely. However, a good agreement of simulated C_2 concentration with respect to peak position and profile shape is found compared to the measurements.

A chemiluminescence (CL) sub-mechanism is added to the validated base mechanism. The CL sub-mechanism consists of reactions leading to the formation and the consumption of the excited species. The mechanism of chemiluminescent species is based on an extensive literature review of reactions and rate coefficients responsible for their formation and consumption. The literature value of major formation reactions vary from two to four orders of magniture from each other and so selection of reaction rates is difficult. In addition, the major CL formation reactions are not clearly understood. The validation of the CL mechanism is done for shock-tube and for laminar flame conditions.

There is no direct relation available between the CL intensities measured in shock-tube and calculated CL concentrations. Therefore, a calibration factor is required for the conversion of the measured intensity to concentrations. In H_2/O_2 mixtures it is found that above 3000 K initial temperature, the OH* is formed due to thermal excitation rather than chemical excitation and so the OH* intensities are independent of rate of reactions forming OH*. So based on the simulated OH* concentrations, the measured intensities are converted to the concentrations. A rate coefficient of the reaction H + O + M $\rightarrow$ OH* + M is recommended in the present work. This is relatively easy with OH* measurements where the H_2 oxidation mechanism is relatively well known. However, the CH* formation is more complicated with three different reactions and many degrees of freedom arising from acetylene and C_2 chemistry. And therefore, a direct comparison of measured CH* intensities with simulated concentrations is not possible with shock-tube measurements. The absolute concentrations measured in flames provide a more stringent test for mechanism validation. The absolute species concentration of OH*, CH*, and C_2*

measured in laminar premixed flames is available in the literature and the mechanism prediction is validated against these measurements. For the very first time, the CH(B) state is measured in the literature and so a relative comparison of measured intensity and simulated concentration at different fuel stoichiometries is done. A good agreement with respect to peak concentration, position of flame along the burner axis and the profile shape are found for the OH*, CH*, and C_2* for lean to rich stoichiometry.

An attempt is made to investigate the potential of chemiluminescence as a heat release marker. It is seen that the peak of the OH* and CH* concentration is found close to the location of the heat release. The differences between the peak heat release and excited species location are relatively small compared to the resolution of most measurement techniques (few milimeters for laboratory flame). Therefore, OH* and CH* can be considered as potential heat release markers for heat release zone.

In the future, research can be extended to focus on identifying main formation pathways of CH*, as soon as new experiments become available. The chemiluminescence of CO_2* is also considered as a potential heat release marker. However, no absolute flame concentration measurements are available for the validation of the mechanism. Furthermore, the CL mechanism can be extended for such and other excited species. The CL mechanism can be further used to simulate larger combustion devices and investigate the relation of chemiluminescence as heat release and reaction zone marker not only for laminar but also for turbulent conditions.

Bibliography

[1] A. G. Gaydon. The spectroscopy of flames. *Wiley: New York*, 1974.

[2] L. C. Haber and U. Vandsburger. A global reaction model for OH* chemiluminescence applied to a laminar flat-flame burner. *Combustion Science and Technology*, 175:1859, 2003.

[3] Y. Hardalupas and M. Orain. Local measurement of the time-dependent heat release rate and equivalence ratio using chemiluminescent emission from a flame. *Combustion and Flame*, 139:188, 2004.

[4] C. S. Panoutsos, Y. Hardalupas, and A. M. K. P. Taylor. Numerical evaluation of equivalence ratio measurement using OH* and CH* chemiluminescence in premixed and non-premixed methane-air flames. *Combustion and Flame*, 156:273–291, 2009.

[5] T. Kathrotia, U. Riedel, and J. Warnatz. A numerical study on the relation of OH*, CH*, C_2* chemiluminescence and heat release in premixed methane flame. *Proceedings of the European Combustion Meeting*, 2009.

[6] H. Najm, O. Knio, P. Paul, and P. Wyckoff. A study of flame observables in premixed methane-air flames. *Combustion Science and Technology*, 140:369, 1998.

[7] J. M. Samaniego, F. N. Egolfopoulos, and C. T. Bowman. CO_2* chemiluminescence in premixed flames. *Combustion Science and Technology*, 109:183, 1995.

[8] L. C. Haber, U. Vandsburger, W. R. Saunders, and V. K. Khanna. An experimental examination of the relationship between chemiluminescent light emissions and heat release rate under non-adiabatic conditions. *Proceedings of International gas turbine institute*, 2000-GT-0121, 2000.

[9] V. Nori and J. M. Seitzman. Chemiluminescence measurements and modeling in Syngas, methane and Jet-A fueled Combustors. *45th AIAA Aerospace Sciences Meeting and Exhibit*, AIAA 2007-0466, 2007.

[10] V. N. Nori and J. M. Seitzman. CH* chemiluminescence modeling for combustion diagnostics. *Proceedings of the Combustion Institute*, 32:895, 2009.

[11] J. Kojima, Y. Ikeda, and T. Nakajima. Spatially resolved measurement of OH*, CH* and C_2* chemiluminescence in the reaction zone of laminar methane/air premixed flames. *Proceedings Combustion Institute*, 28:1757, 2000.

[12] H. Najm, P. Paul, C. Mueller, and P. Wyckoff. On the adequacy of certain experimental observables as measurements of flame burning rate. *Combustion and Flame*, 113:312, 1998.

[13] J. Warnatz, U. Maas, and R. Dibble. *Combustion - Physical and chemical fundamentals, modeling and simulation, experiments, pollutant formation.* Springer, 4th edition.

[14] L. Petzold. A description of *DASSL*. *Report SAND*, 82-8637, 1982.

[15] P. Deuflhard and U. Nowak. Extrapolation integrators for quasilinear implicit ODEs. *DFG-SFB-123: Tech. Rep., Heidelberg University*, 1985.

[16] H. Tsuji and I. Yamaoka. Structure analysis of counterflow diffusion flames in the forward stagnation region of a porous cylinder. *Proceedings of the Combustion Institute*, 13:723, 1971.

[17] M. W. Chase, C. A. Davies Jr., J. R. Downey, D. J. Frurip Jr., R. A. McDonald, and A. N. Syverud. JANAF thermochemical tables third edition. *Journal of Physical and Chemical Reference Data, Supplement No. 1*, page 14, 1985.

[18] E. Goos, A. Burcat, and B. Ruscic. *New NASA Thermodynamic Polynomials Database With Active Thermochemical Tables updates*, 2011.

[19] F. A. Lindemann. Discussion on the radiation theory of chemical action. *Transactions of Faraday Society*, 17:598, 1922.

[20] H. Carstensen and Dean A. M. Chapter 4: The kinetics of pressure-dependent reactions. *Comprehensive Chemical Kinetics*, 42:101, 2007.

[21] R. G. Gilbert, K. Luther, and J. Troe. Theory of thermal unimolecular reactions in the fall-off range. II. Weak collision rate constants. *Ber. Bunsenges. Phys. Chem.*, 87:169, 1983.

[22] M. De Leo, A. Saveliev, L. A. Kennedy, and S. A. Zelepouga. OH and CH luminescence in opposed flow methane oxy-flames. *Combustion and Flame*, 149:435, 2007.

[23] P. Atkins and J. Paula. *Physical Chemistry.* 8th edition.

[24] W. Demtroeder. *Laser Spectroscopy.* Springer Verlag, 3rd edition.

[25] J. Kojima, Y. Ikeda, and T. Nakajima. Basic aspects of OH(A), CH(A), and C_2(d) chemiluminescence in the reaction zone of laminar methane-air premixed flames. *Combustion and Flame*, 140:34, 2005.

[26] C. Heghes. C_1 to C_4 hydrocarbon oxidation mechanism. *PhD Thesis, Heidelberg*, 2007.

[27] T. Kathrotia, M. Fikri, M. Bozkurt, M. Hartmann, U. Riedel, and C. Schulz. Study of the H+O+M reaction forming OH*: Kinetics of OH* chemiluminescence in hydrgen combustion systems. *Combustion and Flame*, 157:1261, 2010.

[28] G. L. Schott and J. L. Kinsey. Kinetic studies of hydroxyl radicals in shock waves. II. Induction times in the hydrogen-oxygen reactions. *The Journal of Chemical Physics*, 29:1177, 1958.

[29] K. T. Aung, M. I. Hassen, and G. M. Faeth. Flame Stretch Interaction of Laminar Premixed Hydrogen/Air Flames at Normal Temperature and Pressure. *Combustion and Flame*, 109:1, 1997.

[30] S. C. Taylor. *PhD Thesis, University of Leeds*, 1991.

[31] C. M. Vagelopoulos, F. N. Egolfopoulos, and C. K. Law. Further considerations on the determination of laminar flame speeds with the counterflow twin-flame technique. *Proceedings of the Combustion Institute*, 25:1341, 1994.

[32] C. K. Wu and C. K. Law. On the determination of laminar flame speeds from stretched flames. *Proceedings of the Combustion Institute*, 20:1941, 1985.

[33] J. Warnatz. Calculation of the structure of laminar flat flames I: Flame velocity of freely propagating ozone decomposition flames. *Ber. Bunsenges. Phys. Chem.*, 82:193, 1978.

[34] G. P. Smith, C. Park, and J. Luque. A note on chemiluminescence in low-pressure hydrogen and methane-nitrous oxide flames. *Combustion and Flame*, 140:385, 2005.

[35] T. Vandooren and J. Bian. Validation of H_2/O_2 reaction mechanisms by comparison with the experimental structure of a rich hydrogen-oxygen flame. *Proceedings of the Combustion Institute*, 23:341, 1991.

[36] J. Warnatz. The structure of freely propagating and burner-stabilized flames in the H_2-CO-O_2 system. *Ber. Bunsenges. Phys. Chem.*, 83:950, 1979.

[37] D. F. Davidson and R. K. Hanson. Fundamental kinetics database utilizing shock-tube measurements. *Volume 1: Ignition delay time measurements*, page 12, 2005.

[38] E. L. Petersen, M. Rohrig, D. F. Davidson, R. K. Hanson, and C. T. Bowman. High-pressure methane oxidation behind reflected shock waves. *Proceedings of the Combustion Institute*, 26:799, 1996.

[39] G. P. Smith, D. M. Golden, M. Frenklach, N. W. Moriarty, B. Eiteneer, M. Goldenberg, C. T. Bowmann, R. K. Hanson, S. Song, W. C. Gardiner Jr., V. V. Lissianski, and Z. Qin. *GRI-mech 3.0, University of California, Berkeley, CA.*, 1999.

[40] J. B. Homer and G. B. Kistiakowsky. Oxidation and pyrolysis of ethylene in shock waves. *The Journal of Chemical Physics*, 47:5290, 1967.

[41] R. P. Lindstedt and G. Skevis. Chemistry of acetylene flames. *Combustion Science and Technology*, 125:73, 1997.

[42] D. L. Baulch, C. T. Bowman, C. J. Cobos, R. A. Cox, Th. Just, J. A. Kerr, M. J. Pilling, D. Stocker, J. Troe, W. Tsang, R. W. Walker, and J. Warnatz. Evaluated kinetic data for combustion modelling: Supplement II. *Journal of Physical Chemistry Reference Data*, 34:757, 2005.

[43] Miller J. A., Mitchell R. E., Smooke M. D., and Kee R. J. Toward a comprehensive chemical kinetic mechanism for the oxidation of acetylene: Comparison of model predictions with results from flame and shock tube experiments. *Proceedings of the Combustion Institute*, 19:181, 1982.

[44] S. Wagner and V. Ebert. *Personal communication*, 2010.

[45] S. Wagner, B. T. Fisher, J. W. Fleming, and V. Ebert. TDLAS-based *in situ* measurement of absolute acetylene concentrations in laminar 2D diffusion flames. *Proceedings Combustion Institute*, 32:839, 2009.

[46] G. P. Smith, C. Park, J. Schneiderman, and J. Luque. C_2 Swan band laser-induced fluorescence and chemiluminescence in low-pressure hydrocarbon flames. *Combustion and Flame*, 141:66, 2005.

[47] J. W. Thoman Jr. and A. McIlroy. Absolute CH radical concentrations in rich low-pressure methane-oxygen-argon flames via cavity ringdown spectroscopy of the $A^2\Delta$-$X^2\Pi$ transition. *Journal of Physical Chemistry A*, 104:4953, 2000.

[48] E. Bastin, J. L. Delfau, M. Reuillon, C. Vovelle, and J. Warnatz. Experimental and computational investigation of the structure of a sooting C_2H_2-O_2-Ar flame. *Proceedings Combustion Institute*, 22:313, 1988.

[49] K. Devriendt and J. Peeters. Direct identificationof the $C_2H(X^2\Sigma^+) + O(^3P) \rightarrow CH(A^2\Delta) + CO$ as the source of the $CH(A^2\Delta \rightarrow X^2\Pi)$ chemiluminescence in the C_2H_2/O/H atomic flames. *Journal of Physical Chemistry A*, 101:2546, 1997.

[50] C. Gibaud, J. Snyder, V. Sick, and R. P. Lindstedt. Laser-induced fluorescence measurements and modeling of absolute CH concentrations in strained laminar methane/air diffusion flames. *Proceedings of the Combustion Institute*, 30:455, 2005.

[51] S. V. Naik and N. M. Laurendeau. Measurements of absolute CH concentrations by cavity ring-down spectroscopy and linear laser-induced fluorescence in laminar, counterflow partially premixed and nonpremixed flames at atmospheric pressure. *Applied Optics*, 43:5116, 2004.

[52] W. Tsang and R. F. Hampson. Chemical kinetic data base for combustion chemistry. Part I. Methane and related compounds. *Journal of Physical Chemistry Reference Data*, 15:1087, 1986.

[53] P. A. Berg, D. A. Hill, A. R. Noble, G. P. Smith, J. B. Jeffries, and D. R. Crosley. Absolute CH concentration measurements in low-pressure methane flames: Comparisons with model results. *Combustion and Flame*, 121:223, 2000.

[54] A. McIlroy. Direct measurement of $^1CH_2$ in flames by cavity ringdown laser absorption spectroscopy. *Chemical Physics Letters*, 296:151, 1998.

[55] M. Tamura, P. A. Berg, J. E. Harrington, J. Luque, J. B. Jeffries, G. P. Smith, and D. R. Crosley. Collisional quenching of CH(A), OH(A) and NO(A) in low pressure hydrocarbon flames. *Combustion and Flame*, 114:502, 1998.

[56] S. L. N. G. Krishnamachari and H. P. Broida. Effect of molecular Oxygen on the emission spectra of atomic oxygen-acetylene flames. *The Journal of Chemical Physics*, 34:1709, 1961.

[57] K. Becker, D. Haaks, and T. Tatarczyk. The natural lifetime of OH ($2\Sigma^+$, v=0, N=2, J=3/2) and its quenching by atomic hydrogen. *Chemical Physics Letters*, 25:564, 1974.

[58] R. Porter, A. Clark, W. Kaskan, and W. Browne. A study of hydrocarbon flames. *Proceedings Combustion Institute*, 11:907, 1967.

[59] I. Messing, C. Sadowski, and S. Filseth. Absolute rate constant for the reaction of CH with O_2. *Chemical Physics Letters*, 66:95, 1979.

[60] D. A. Lichtin, M. R. Berman, and M. C. Lin. NH($A^3\Pi \rightarrow X^3\Sigma^-$) chemiluminescence from the CH($^2\Pi$) + NO reaction. *Chemical Physics Letters*, 108:18, 1984.

[61] M. R. Berman, J. W. Fleming, A. B. Harvey, and M. C. Lin. Temperature dependence of CH radical reactions with O_2, NO, CO and CO_2. *Proceedings Combustion Institute*, 19:73, 1982.

[62] J. Grebe and K. H. Homann. Blue-green chemiluminescence in the system C_2H_2/O/H. Formation of the emitters CH($A^2\Delta$), $C_2(d^3\Pi_g)$ and C_2H^*. *Ber. Bunsenges. Phys. Chem*, 86:587, 1982.

[63] G. P. Smith, J. Luque, C. Park, J. B. Jeffries, and D. R. Crosley. Low pressure flame determinations of rate constants for OH(A) and CH(A) chemiluminescence. *Combustion and Flame*, 131:59, 2002.

[64] S. A. Carl, M. V. Poppel, and J. Peeters. Identification of the CH + $O_2 \rightarrow$ OH(A) + CO reaction as the source of OH(A-X) chemiluminescence in $C_2H_2/O/H/O_2$ atomic flames and determination of its absolute rate constant over the range T = 296 to 511 K. *Journal of Physical Chemistry*, 107:11001, 2003.

[65] J. M. Hall and E. L. Petersen. An optimized kinetics model for OH chemiluminescence at high temperatures and atmospheric pressures. *International Journal of Chemical Kinetics*, 38:714, 2006.

[66] M. Charton and A. G. Gaydon. Excitation of spectra of OH in hydrogen flames and its relation to excess concentrations of free atoms. *Proceedings of the Royal Society of London A*, 245:84, 1958.

[67] S. W. Yoo, C. K. Law, and S. D. Tse. Chemiluminescent OH* and CH* flame structure and aerodynamic scaling of weakly buoyant, nearly spherical diffusion flames. *Proceedings of the Combusion Institute*, 29:1663, 2002.

[68] Kaskan W. E. Abnormal excitation of OH in $H_2/O_2/N_2$ flames. *The Journal of Chemical Physics*, 31:944, 1959.

[69] Y. Hidaka, S. Takahashi, H. Kawano, M. Suga, and W. C. Gardiner Jr. Shock-tube measurement of the rate constant for excited $OH(A^2\Sigma^+)$ formation in the hydrogen-oxygen reaction. *Journal of Physical Chemistry*, 86:1429, 1982.

[70] Koike T. and Morinaga K. Further studies of the rate constant for chemical excitation of OH in shock waves. *Bull. Chem. Soc. Jpn.*, 55:52, 1982.

[71] C. S. T. Marques, L. H. Benvenutti, and C. A. Bertran. Kinetic modeling for chemiluminescent radicals in acetylene combustion. *J. Braz. Chem. Soc.*, 17:302, 2006.

[72] O. V. Skrebkov, Yu. P. Myagkov, S. P. Karkach, V. M. Vasilev, and A. L. Smirnov. Formation mechanism of the excited $OH(^2\Sigma^+)$ radical during the ignition of the diluted H_2-O_2 mixture by shock waves. *Doklady Physical Chemistry*, 383:93, 2002.

[73] P. W. Fairchild, G. P. Smith, and D. R. Crosley. Collisional quenching of $A^2\Sigma^+$ OH at elevated temperatures. *The Journal of Chemical Physics*, 79:1795, 1983.

[74] A. E. Bailey, D. E. Heard, P. H. Paul, and M. J. Pilling. Collisional quenching of OH(A) by N_2, O_2 and CO_2 between 204 and 294 K. Implications for atmospheric measurements of OH by laser-induced fluorescence. *J. Chem. Soc., Faraday Trans.*, 93:2915, 1997.

[75] B. L. Hemming, D. R. Crosley, J. E. Harrington, and V. Sick. Collisional quenching of high rotational levels in $OH(A^2\Sigma^+)$. *Journal of Chemical Physics*, 115:3099, 2001.

[76] B. L. Hemming and D. R. Crosley. Rotational level dependence of OH($A^2\Sigma^+$) quenching at 242 and 196 K . *Journal of Physical Chemistry A*, 106:8992, 2002.

[77] D. E. Heard and D. A. Henderson. Quenching of OH ($A^2\Sigma^+$, v'=0) by several collision partners between 200 and 344 K. Cross-section measurements and model comparisons. *Physical Chemistry Chemical Physics*, 2:67, 2000.

[78] P. Paul, J. Durant, and J. Gray. Collisional electronic quenching of OH($A^2\Sigma$) measured at high temperature in a shock tube. *The Journal of Chemical Physics*, 102:8378, 1995.

[79] J. Jeffries, K. Kohse-Hoeinghaus, G. Smith, R. Copeland, and D. Crosley. Rotational-level-dependent quenching of OH($A^2\Sigma^+$) at flame temperatures. *Chemical Physics Letters*, 152:160, 1988.

[80] E. M. Bulewicz, P. J. Padley, and R. E. Smith. Spectroscopy studies of C_2, CH and OH radicals in low pressure acetylene+oxygen flames. *Proceedings of the Royal Society of London A*, 315:129, 1970.

[81] H. H. Brenig. *PhD Thesis, Wuppertal*, 1981.

[82] C. Hand and G. Kistiakowsky. Ionization cccompanying the ccetylene-oxygen reaction in shock waves. *The Journal of Chemical Physics*, 37:1239, 1962.

[83] C. T. Bowman and D. J. Seery. Chemiluminescence in the high-temperature oxidation of methane. *Combustion and Flame*, 12:611, 1968.

[84] S. Matsuda, I. Slagle, D. Fife, J. Marquart, and D. Gutman. Shock-tube study of acetylene-oxygen reaction. IV. Kinetic study of CH, C_2, and continuum chemiluminescence during the induction period. *Journal of Chemical Physics*, 57:5277, 1972.

[85] S. Hwang, W. C. Gardiner Jr., M. Frenklach, and Y. Hidaka. Induction zone exothermicity of acetylene ignition. *Combustion and Flame*, 67:65, 1987.

[86] A. N. Eraslan and R. C. Brown. Chemiionization and ion-molecule reactions in fuel-rich acetylene flames. *Combustion and Flame*, 74:19, 1988.

[87] K. Devriendt, H. Look, B. Ceursters, and J. Peeters. Kinetics of formation of chemiluminescent CH($A^2\Delta$) by the elementary reactions of $C_2H(X^2\Sigma^+)$ with $O(^3P)$

and $O_2(X^3\Sigma_g^-)$: A pulse laser photolysis study. *Chemical Physics Letters*, 261:450, 1996.

[88] R. Elsamra, S. Vranckx, and S. Carl. $CH(A^2\Delta)$ formation in hydrocarbon combustion: The temperature dependence of the rate constant of the reaction $C_2H + O_2 \rightarrow CH(A^2\Delta) + CO_2$. *Journal of Physical Chemistry A*, 109:10287, 2005.

[89] J. M. Hall, J. Vries, A. Amadio, and E. L. Petersen. Towards a kinetics model of CH chemiluminescence. *Aerospace Sciences Meeting and Exhibit*, 43:AIAA 2005–1318, 2005.

[90] J. Mertens. A shock tube study of CH* reaction kinetics in CH_4 and C_2H_2 oxidation. *22nd International Symposium on Shock Waves*, 22:171, 1999.

[91] R. E. Ferguson. On the origin of the electronically excited C_2* radical in hydrocarbon flames. *The Journal of Chemical Physics*, 23:2085, 1955.

[92] K. Schofield and M. Steinberg. CH and C_2 measurements imply a radical pool within a pool in acetylene flames. *Journal of Physical Chemistry A*, 111:2098, 2007.

[93] M. Koehler, A. Brockhinke, M. Braun-Unkhoff, and K. Kohse-Hoeinghaus. Quantitative laser diagnostic and modeling study of C_2 and CH chemistry in combustion. *Journal of Physical Chemistry A*, 114:4719, 2010.

[94] U. Maas and J. Warnatz. Ignition processes in hydrogen-oxygen mixtures. *Combustion and Flame*, 74:53, 1988.

[95] U. Maas. Coupling of chemical reaction with flow and molecular transport. *Applications of Mathematics*, 40:249, 1995.

[96] E. Petersen, D. Kalitan, and M. Rickard. Calibration and chemical kinetics modeling of an OH chemiluminescence diagnostic. *AIAA Joint Propulsion Conference and Exhibit*, 2003.

[97] D. M. Kalitan, J. D. Mertens, M. W. Crofton, and E. L. Petersen. Ignition and oxidation of lean CO/H_2 fuel blends in air. *Journal of Propulsion and Power*, 23:1291, 2007.

[98] M. Bozkurt, M. Fikri, and C. Schulz. *Personal communication*, 2010.

[99] M. J. Rickard, J. M. Hall, and E. L. Petersen. Effect of silane addition on acetylene ignition behind reflected shock waves. *Proceedings of the Combustion Institute*, 30:1915, 2005.

[100] A. Seipel, A. Brokhinke, and K. Kohse-Hoeinghaus. *Personal communication*, 2010.

A Reaction Mechanism

No.	Elementary reaction										A	n	E
1. H_2–CO oxidation													
1.1. H_2–O_2 reactions (no HO_2, H_2O_2)													
R1	O_2	+	H			=	OH	+	O		$2.06{\cdot}10^{14}$	-0.097	62.85
R2	H_2	+	O			=	OH	+	H		$3.82{\cdot}10^{12}$	0.0	33.26
	H_2	+	O			=	OH	+	H		$1.02{\cdot}10^{15}$	0.0	80.23
R3	H_2	+	OH			=	H_2O	+	H		$2.17{\cdot}10^{8}$	1.52	14.47
R4	OH	+	OH			=	H_2O	+	O		$3.35{\cdot}10^{4}$	2.42	-8.06
R5	H	+	H	+	M(1)	=	H_2	+	M(1)		$1.02{\cdot}10^{17}$	-0.6	0.0
R6	O	+	O	+	M(1)	=	O_2	+	M(1)		$5.40{\cdot}10^{13}$	0.0	-7.4
R7	H	+	OH	+	M(2)	=	H_2O	+	M(2)		$5.56{\cdot}10^{22}$	-2.0	0.0
1.2. HO_2 formation/consumption													
R8	H	+	O_2	+	M(3)	=	HO_2	+	M(3)		$1.75{\cdot}10^{17}$	0.0	0.0
										Low	$2.37{\cdot}10^{19}$	-1.2	0.0
										Troe	0.5 0.0	0.0	0.0
R9	HO_2	+	H			=	OH	+	OH		$4.46{\cdot}10^{14}$	0.0	5.82
R10	HO_2	+	H			=	H_2	+	O_2		$1.05{\cdot}10^{14}$	0.0	8.56
R11	HO_2	+	H			=	H_2O	+	O		$1.44{\cdot}10^{12}$	0.0	0.0
R12	HO_2	+	O			=	OH	+	O_2		$1.63{\cdot}10^{13}$	0.0	-1.86
R13	HO_2	+	OH			=	H_2O	+	O_2		$9.28{\cdot}10^{15}$	0.0	73.25
1.3. H_2O_2 formation/consumption													
R14	HO_2	+	HO_2			=	H_2O_2	+	O_2		$4.22{\cdot}10^{14}$	0.0	50.14
	HO_2	+	HO_2			=	H_2O_2	+	O_2		$1.32{\cdot}10^{11}$	0.0	-6.82
R15	OH	+	OH	+	M(1)	=	H_2O_2	+	M(1)		$1.57{\cdot}10^{13}$	0.0	0.0
										Low	$5.98{\cdot}10^{19}$	-0.8	0.0
										Troe	0.5 0.0	0.0	0.0
R16	H_2O_2	+	H			=	H_2	+	HO_2		$1.69{\cdot}10^{12}$	0.0	15.71
R17	H_2O_2	+	H			=	H_2O	+	OH		$1.02{\cdot}10^{13}$	0.0	14.97
R18	H_2O_2	+	O			=	OH	+	HO_2		$4.22{\cdot}10^{11}$	0.0	16.63
R19	H_2O_2	+	O			=	H_2O	+	O_2		$4.22{\cdot}10^{11}$	0.0	16.63
R20	H_2O_2	+	OH			=	H_2O	+	HO_2		$1.64{\cdot}10^{18}$	0.0	123.05
	H_2O_2	+	OH			=	H_2O	+	HO_2		$1.92{\cdot}10^{12}$	0.0	1.79
1.4. CO reactions													
R21	CO	+	O	+	M(1)	=	CO_2	+	M(1)		$1.54{\cdot}10^{15}$	0.0	12.56
R22	CO	+	OH			=	CO_2	+	H		$1.00{\cdot}10^{13}$	0.0	66.93
	CO	+	OH			=	CO_2	+	H		$9.03{\cdot}10^{11}$	0.0	19.12
	CO	+	OH			=	CO_2	+	H		$1.01{\cdot}10^{11}$	0.0	0.25
R23	CO	+	HO_2			=	CO_2	+	OH		$1.50{\cdot}10^{14}$	0.0	98.7
R24	CO	+	O_2			=	CO_2	+	O		$2.50{\cdot}10^{12}$	0.0	200.0
2. C1–hydrocarbons oxidation													
2.1. C reactions													
R25	CH	+	H			=	C	+	H_2		$5.00{\cdot}10^{14}$*	0.0	0.0
R26	C	+	O_2			=	CO	+	O		$6.02{\cdot}10^{13}$	0.0	2.66

2.2. CH reactions													
R27	CH	+	O			=	CO	+	H			$4.00 \cdot 10^{13}$	0.0	0.0
R28	CH	+	OH			=	CHO	+	H			$3.00 \cdot 10^{13}$	0.0	0.0
R29	CH	+	O_2			=	CHO	+	O			$1.69 \cdot 10^{13}$	0.0	0.0
R30	CH	+	CO	+	M(2)	=	HCCO	+	M(2)			$1.02 \cdot 10^{15}$*	-0.4	0.0
											Low	$3.79 \cdot 10^{0}$	-2.5	0.0
											Troe	0.6 0.0	0.0	0.0
R31	CH	+	CO_2			=	CHO	+	CO			$6.38 \cdot 10^{7}$	1.51	-2.99
R32	CH	+	H_2O			=	CH_2O	+	H			$4.58 \cdot 10^{16}$	-1.42	0.0
R33	CH	+	H_2O			=	$^3CH_2$	+	OH			$4.58 \cdot 10^{16}$	-1.42	0.0
2.3. CHO reactions														
R34	CHO	+	M(1)			=	CO	+	H	+	M(1)	$1.14 \cdot 10^{14}$	0.0	65.02
R35	CHO	+	H			=	CO	+	H_2			$9.03 \cdot 10^{13}$	0.0	0.0
R36	CHO	+	O			=	CO	+	OH			$3.01 \cdot 10^{13}$	0.0	0.0
R37	CHO	+	O			=	CO_2	+	H			$3.01 \cdot 10^{13}$	0.0	0.0
R38	CHO	+	OH			=	CO	+	H_2O			$1.08 \cdot 10^{14}$	0.0	0.0
R39	CHO	+	O_2			=	CO	+	HO_2			$7.59 \cdot 10^{12}$	0.0	1.7
R40	CHO	+	CHO			=	CH_2O	+	CO			$3.00 \cdot 10^{13}$	0.0	0.0
2.4. CH_2 reactions														
R41	$^3CH_2$	+	H			=	CH	+	H_2			$1.20 \cdot 10^{14}$	0.0	0.0
R42	$^3CH_2$	+	O			→	CO	+	H	+	H	$1.23 \cdot 10^{14}$	0.0	2.24
R43	$^3CH_2$	+	O			=	CO	+	H_2			$8.19 \cdot 10^{13}$	0.0	2.24
R44	$^3CH_2$	+	O_2			=	CO	+	OH	+	H	$1.81 \cdot 10^{12}$	0.0	0.0
R45	$^3CH_2$	+	O_2			=	CO_2	+	H_2			$1.81 \cdot 10^{12}$	0.0	0.0
R46	$^3CH_2$	+	$^3CH_2$			=	C_2H_2	+	H_2			$1.81 \cdot 10^{14}$	0.0	49.88
R47	$^3CH_2$	+	$^3CH_2$			=	C_2H_2	+	H	+	H	$1.63 \cdot 10^{15}$	0.0	49.88
R48	$^3CH_2$	+	CH_3			=	C_2H_4	+	H			$7.23 \cdot 10^{13}$	0.0	0.0
R49	$^1CH_2$	+	M(1)			=	$^3CH_2$	+	M(1)			$6.02 \cdot 10^{12}$	0.0	0.0
R50	$^1CH_2$	+	H_2			=	CH_3	+	H			$1.26 \cdot 10^{16}$	-0.56	66.5
R51	$^1CH_2$	+	O_2			=	CO	+	OH	+	H	$3.10 \cdot 10^{13}$	0.0	0.0
2.5. CH_2O reactions														
R52	CH_2O	+	M(1)			=	CHO	+	H	+	M(1)	$4.87 \cdot 10^{15}$	0.0	316.35
R53	CH_2O	+	M(1)			=	CO	+	H_2	+	M(1)	$2.83 \cdot 10^{15}$	0.0	266.96
R54	CH_2O	+	H			=	CHO	+	H_2			$4.10 \cdot 10^{8}$	1.47	10.23
R55	CH_2O	+	O			=	CHO	+	OH			$4.16 \cdot 10^{11}$	0.57	11.56
R56	CH_2O	+	OH			=	CHO	+	H_2O			$1.39 \cdot 10^{13}$	0.0	2.53
R57	CH_2O	+	HO_2			=	CHO	+	H_2O_2			$4.10 \cdot 10^{4}$	2.5	42.73
R58	CH_2O	+	O_2			=	CHO	+	HO_2			$2.44 \cdot 10^{5}$	2.5	152.56
R59	CH_2O	+	CH_3			=	CHO	+	CH_4			$3.19 \cdot 10^{1}$	3.36	18.04
2.6. CH_2OH reactions														
R60	CH_2OH	+	M(1)			=	CH_2O	+	H	+	M(1)	$2.80 \cdot 10^{14}$	-0.73	137.31
											Low	$1.50 \cdot 10^{34}$	-5.39	151.46
											Troe	0.96 67.2	1855.0	7543.0
R61	CH_2OH	+	H			=	CH_2O	+	H_2			$2.44 \cdot 10^{13}$	0.0	0.0
R62	CH_2OH	+	H			=	CH_3	+	OH			$1.05 \cdot 10^{13}$	0.0	0.0
R63	CH_2OH	+	O_2			=	CH_2O	+	HO_2			$2.89 \cdot 10^{16}$	-1.5	0.0
	CH_2OH	+	O_2			=	CH_2O	+	HO_2			$7.23 \cdot 10^{13}$	0.0	15.63
2.7. CH_3 reactions														
R64	CH_3	+	M(1)			=	$^3CH_2$	+	H	+	M(1)	$2.92 \cdot 10^{16}$	0.0	379.0
R65	CH_3	+	M(1)			=	CH	+	H_2	+	M(1)	$1.89 \cdot 10^{16}$	0.0	355.84
R66	CH_3	+	O			=	CH_2O	+	H			$6.74 \cdot 10^{13}$	0.0	0.0
R67	CH_3	+	OH			→	CH_3O	+	H			$1.20 \cdot 10^{10}$	0.0	58.11
R68	CH_3	+	OH			=	$^1CH_2$	+	H_2O			$3.00 \cdot 10^{13}$	0.0	11.64
R69	CH_3	+	OH	+	M(1)	=	CH_3OH	+	M(1)			$4.34 \cdot 10^{15}$	-0.79	0.0

											Low	$1.10{\cdot}10^{38}$	-6.21	5.58
											Troe	0.25 210	1434.0	0.0
R70	CH_3	+	HO_2			=	CH_3O	+	OH			$1.60{\cdot}10^{13}$	0.0	0.0
R71	CH_3	+	O_2			=	CH_2O	+	OH			$6.86{\cdot}10^{1}$	2.86	40.87
R72	CH_3	+	O_2			→	O	+	CH_3O			$1.99{\cdot}10^{18}$	1.57	122.3
R73	CH_3	+	O_2	+	M(1)	=	CH_3O_2	+	M(1)			$7.83{\cdot}10^{8}$	1.2	0.0
											Low	$1.55{\cdot}10^{26}$	-3.3	0.0
											Troe	0.36 0.0	0.0	0.0
R74	CH_3	+	CO	+	M(1)	=	CH_3CO	+	M(1)			$5.06{\cdot}10^{11}$	0.0	28.77
											Low	$3.11{\cdot}10^{14}$	0.0	15.88
											Troe	0.5 0.0	0.0	0.0
R75	CH_3	+	$^1CH_2$			=	C_2H_4	+	H			$7.23{\cdot}10^{13}$	0.0	0.0
R76	CH_3	+	CH_3	+	M(1)	=	C_2H_6	+	M(1)			$3.61{\cdot}10^{13}$	0.0	0.0
											Low	$3.63{\cdot}10^{41}$	-7.0	11.6
											Troe	0.62 73.0	1180.0	0.0
2.8. CH_3O reactions														
R77	CH_3O	+	M(1)			=	CH_2O	+	H	+	M(1)	$6.80{\cdot}10^{13}$	0.0	109.49
											Low	$4.66{\cdot}10^{25}$	-3.0	101.68
											Troe	0.45 0.0	0.0	0.0
R78	CH_3O	+	H			→	CH_3	+	OH			$1.63{\cdot}10^{13}$	0.0	2.49
R79	CH_3O	+	H			=	CH_2O	+	H_2			$3.79{\cdot}10^{13}$	0.0	2.49
R80	CH_3O	+	O			→	O_2	+	CH_3			$1.13{\cdot}10^{13}$	0.0	0.0
R81	CH_3O	+	O			=	OH	+	CH_2O			$3.76{\cdot}10^{12}$	0.0	0.0
R82	CH_3O	+	OH			=	CH_2O	+	H_2O			$1.81{\cdot}10^{13}$	0.0	0.0
R83	CH_3O	+	O_2			=	CH_2O	+	HO_2			$2.17{\cdot}10^{10}$	0.0	7.3
R84	CH_3O	+	CH_2O			=	CH_3OH	+	CHO			$1.15{\cdot}10^{11}$	0.0	5.2
2.9. CH_3O_2 reactions														
R85	CH_3O_2	+	HO_2			=	CH_3O_2H	+	O_2			$2.28{\cdot}10^{11}$	0.0	-6.24
R86	CH_3O_2	+	CH_3			=	CH_3O	+	CH_3O			$1.50{\cdot}10^{13}$	0.0	-5.0
R87	CH_3O_2	+	CH_3O_2			→	CH_2O	+	CH_3OH	+	O_2	$3.43{\cdot}10^{10}$	0.0	-3.24
R88	CH_3O_2	+	CH_3O_2			→	CH_3O	+	CH_3O	+	O_2	$2.29{\cdot}10^{10}$	0.0	-3.24
R89	CH_3O_2	+	H_2O_2			=	CH_3O_2H	+	HO_2			$2.40{\cdot}10^{12}$	0.0	41.8
R90	CH_3O_2	+	CH_2O			=	CH_3O_2H	+	CHO			$1.30{\cdot}10^{11}$	0.0	37.7
R91	CH_3O_2	+	CH_4			=	CH_3O_2H	+	CH_3			$1.81{\cdot}10^{11}$	0.0	77.8
R92	CH_3O_2	+	CH_3OH			=	CH_3O_2H	+	CH_2OH			$1.81{\cdot}10^{11}$	0.0	57.7
2.10. CH_4 reactions														
R93	CH_4	+	M(4)			=	CH_3	+	H	+	M(4)	$1.45{\cdot}10^{40}$	0.0	439.0
											Low	$4.70{\cdot}10^{47}$	-8.2	492.18
											Troe	0.0 1350	1.0	7834.0
R94	CH_4	+	H			=	H_2	+	CH_3			$6.14{\cdot}10^{5}$	2.5	40.12
R95	CH_4	+	O			=	OH	+	CH_3			$4.40{\cdot}10^{5}$	2.5	27.52
R96	CH_4	+	OH			=	H_2O	+	CH_3			$1.37{\cdot}10^{6}$	2.18	11.22
R97	CH_4	+	HO_2			=	H_2O_2	+	CH_3			$4.70{\cdot}10^{4}$	2.5	87.88
R98	CH_4	+	O_2			=	CH_3	+	HO_2			$4.88{\cdot}10^{5}$	2.5	219.24
R99	CH_4	+	CH			=	C_2H_4	+	H			$1.32{\cdot}10^{16}$	-0.94	0.24
R100	CH_4	+	$^3CH_2$			=	CH_3	+	CH_3			$8.40{\cdot}10^{12}$	0.0	-2.08
2.11. CH_3OH reactions														
R101	CH_3OH	+	H			=	CH_2OH	+	H_2			$2.75{\cdot}10^{9}$	1.24	18.79
R102	CH_3OH	+	H			=	CH_3O	+	H_2			$6.87{\cdot}10^{8}$	1.24	18.79
R103	CH_3OH	+	O			=	CH_2OH	+	OH			$1.98{\cdot}10^{13}$	0.0	22.2
R104	CH_3OH	+	O			=	CH_3O	+	OH			$4.94{\cdot}10^{12}$	0.0	22.2
R105	CH_3OH	+	OH			=	CH_2OH	+	H_2O			$5.27{\cdot}10^{6}$	1.92	-1.2
R106	CH_3OH	+	OH			=	CH_3O	+	H_2O			$9.30{\cdot}10^{5}$	1.92	-1.2
R107	CH_3OH	+	HO_2			=	CH_2OH	+	H_2O_2			$6.20{\cdot}10^{12}$	0.0	81.1

R108	CH_3OH	+	O_2	=	HO_2	+	CH_2OH			$2.05{\cdot}10^{13}$	0.0	189.1
R109	CH_3OH	+	CH_3	=	CH_4	+	CH_2OH			$9.94{\cdot}10^{0}$	3.45	33.42
R110	CH_3OH	+	CH_3	=	CH_4	+	CH_3O			$2.02{\cdot}10^{1}$	3.45	33.42
R111	CH_3OH	+	CH_3O	=	CH_2OH	+	CH_3OH			$1.50{\cdot}10^{12}$	0.0	29.3
R112	CH_3OH	+	CH_2O	→	CH_3O	+	CH_3O			$1.53{\cdot}10^{12}$	0.0	333.2
2.12. CH_3O_2H reactions												
R113	CH_3O_2H			=	CH_3O	+	OH			$6.00{\cdot}10^{14}$	0.0	177.1
R114	CH_3O_2H	+	O	=	OH	+	CH_3O_2			$2.47{\cdot}10^{13}$	0.0	19.95
R115	CH_3O_2H	+	OH	=	H_2O	+	CH_3O_2			$1.08{\cdot}10^{12}$	0.0	-1.83
3. C_2–hydrocarbons oxidation												
3.1. C_2H reactions												
R116	C_2H	+	O	=	CO	+	CH			$5.96{\cdot}10^{13}$	0.0	0.0
R117	C_2H	+	O_2	=	CHO	+	CO			$1.0{\cdot}10^{15}$*	-0.35	0.0
R118	C_2H	+	O_2	=	H	+	CO	+	CO	$1.92{\cdot}10^{15}$*	-0.35	0.0
R119	C_2H	+	O_2	=	CO_2	+	CH			$8.15{\cdot}10^{12}$*	-0.35	0.0
R120	C_2H	+	O_2	=	HCCO	+	O			$8.15{\cdot}10^{12}$*	-0.35	0.0
R121	C_2H	+	CH_4	=	C_2H_2	+	CH_3			$2.17{\cdot}10^{10}$	0.94	2.73
3.2. HCCO reactions												
R122	HCCO	+	H	=	$^3CH_2$	+	CO			$1.06{\cdot}10^{13}$	0.0	0.0
R123	HCCO	+	O	→	CO	+	CO	+	H	$1.53{\cdot}10^{14}$	0.0	0.0
R124	HCCO	+	$^3CH_2$	=	C_2H_3	+	CO			$3.00{\cdot}10^{13}$	0.0	0.0
3.3. C_2H_2 reactions												
R125	C_2H_2	+	M(1)	=	C_2H	+	H	+	M(1)	$3.60{\cdot}10^{16}$	0.0	446.0
R126	C_2H_2	+	H	=	C_2H	+	H_2			$5.01{\cdot}10^{10}$*	1.64	126.79
R127	C_2H_2	+	O	=	$^3CH_2$	+	CO			$1.48{\cdot}10^{8}$	1.4	9.23
R128	C_2H_2	+	O	=	HCCO	+	H			$9.40{\cdot}10^{8}$	1.4	9.23
R129	C_2H_2	+	OH	=	H_2O	+	C_2H			$2.42{\cdot}10^{14}$*	0.0	56.54
R130	C_2H_2	+	O_2	=	HCCO	+	OH			$5.00{\cdot}10^{7}$*	1.5	126.0
R131	C_2H_2	+	C_2H	=	C_4H_2	+	H			$7.83{\cdot}10^{13}$	0.0	0.0
3.4. CH_2CO reactions												
R132	CH_2CO	+	M(1)	=	$^3CH_2$	+	CO	+	M(1)	$1.00{\cdot}10^{16}$	0.0	248.0
R133	CH_2CO	+	H	=	CH_3	+	CO			$3.25{\cdot}10^{10}$	0.85	11.89
R134	CH_2CO	+	O	=	CH_2O	+	CO			$3.61{\cdot}10^{11}$	0.0	5.65
R135	CH_2CO	+	O	→	CHO	+	H	+	CO	$1.81{\cdot}10^{11}$	0.0	5.65
R136	CH_2CO	+	O	=	CHO	+	CHO			$1.81{\cdot}10^{11}$	0.0	5.65
R137	CH_2CO	+	OH	=	CH_3	+	CO_2			$6.24{\cdot}10^{11}$	0.0	4.24
R138	CH_2CO	+	OH	=	CH_2O	+	CHO			$3.37{\cdot}10^{10}$	0.0	4.24
3.5. C_2H_3 reactions												
R139	C_2H_3	+	M(1)	=	C_2H_2	+	H	+	M(1)	$7.80{\cdot}10^{8}$	1.62	155.06
									Low	$3.24{\cdot}10^{27}$	-3.4	149.82
									Troe	0.35 0.0	0.0	0.0
R140	C_2H_3	+	H	=	C_2H_2	+	H_2			$4.22{\cdot}10^{13}$	0.0	0.0
R141	C_2H_3	+	O	=	C_2H_2	+	OH			$3.01{\cdot}10^{13}$	0.0	0.0
R142	C_2H_3	+	O	=	CH_3	+	CO			$3.01{\cdot}10^{13}$	0.0	0.0
R143	C_2H_3	+	O	=	CHO	+	$^3CH_2$			$3.01{\cdot}10^{13}$	0.0	0.0
R144	C_2H_3	+	OH	=	C_2H_2	+	H_2O			$5.00{\cdot}10^{12}$	0.0	0.0
R145	C_2H_3	+	O_2	=	CH_2O	+	CHO			$7.71{\cdot}10^{12}$	0.0	-1.0
R146	C_2H_3	+	O_2	=	CH_2CHO	+	O			$8.15{\cdot}10^{12}$	0.0	-1.04
R147	C_2H_3	+	O_2	=	C_2H_2	+	HO_2			$4.65{\cdot}10^{11}$	0.0	-1.04
3.6. CH_3CO reactions												
R148	CH_3CO	+	H	=	CH_2CO	+	H_2			$2.00{\cdot}10^{13}$	0.0	0.0
3.7. CH_2CHO reactions												
R149	CH_2CHO	+	H	=	CH_2CO	+	H_2			$2.00{\cdot}10^{13}$	0.0	0.0
3.8. C_2H_4 reactions												

R150	C_2H_4	+	M(1)			=	C_2H_2	+	H_2	+	M(1)	$2.92{\cdot}10^{17}$	1.0	327.49
R151	C_2H_4	+	M(1)			=	C_2H_3	+	H	+	M(1)	$7.40{\cdot}10^{17}$	0.0	404.06
R152	C_2H_4	+	H	+	M(1)	→	C_2H_5	+	M(1)			$3.98{\cdot}10^{9}$	1.28	5.4
											Low	$1.18{\cdot}10^{19}$	0.0	3.2
											Troe	0.76 40.0	1025.0	0.0
R153	C_2H_4	+	H			=	C_2H_3	+	H_2			$2.35{\cdot}10^{2}$	3.62	47.14
R154	C_2H_4	+	O			=	CH_2CHO	+	H			$4.74{\cdot}10^{6}$	1.88	0.76
R155	C_2H_4	+	O			=	CHO	+	CH_3			$8.13{\cdot}10^{6}$	1.88	0.76
R156	C_2H_4	+	O			=	CH_2CO	+	H_2			$6.77{\cdot}10^{5}$	1.88	0.76
R157	C_2H_4	+	OH			=	C_2H_3	+	H_2O			$6.48{\cdot}10^{12}$	0.0	24.9
R158	C_2H_4	+	CH			=	C_3H_4	+	H			$1.32{\cdot}10^{14}$	0.0	-1.44
R159	C_2H_4	+	$^1CH_2$			=	C_3H_6					$7.24{\cdot}10^{13}$	0.0	0.0
R160	C_2H_4	+	CH_3			=	C_2H_3	+	CH_4			$6.02{\cdot}10^{7}$	1.56	69.6
3.9. CH_3CHO reactions														
R161	CH_3CHO	+	M(1)			=	CH_3	+	CHO	+	M(1)	$2.10{\cdot}10^{16}$	0.0	342.0
											Low	$7.83{\cdot}10^{17}$	0.0	342.0
											Troe	0.5 0.0	0.0	0.0
R162	CH_3CHO	+	H			=	CH_3CO	+	H_2			$2.05{\cdot}10^{9}$	1.16	10.06
R163	CH_3CHO	+	H			=	CH_2CHO	+	H_2			$2.05{\cdot}10^{9}$	1.16	10.06
R164	CH_3CHO	+	O			=	CH_3CO	+	OH			$5.26{\cdot}10^{12}$	0.0	7.6
R165	CH_3CHO	+	O			=	CH_2CHO	+	OH			$5.84{\cdot}10^{11}$	0.0	7.6
R166	CH_3CHO	+	OH			=	CH_3CO	+	H_2O			$2.69{\cdot}10^{8}$	1.35	-6.58
R167	CH_3CHO	+	OH			=	CH_2CHO	+	H_2O			$2.02{\cdot}10^{7}$	1.35	-6.58
R168	CH_3CHO	+	HO_2			=	CH_3CO	+	H_2O_2			$4.10{\cdot}10^{4}$	2.5	42.69
R169	CH_3CHO	+	O_2			=	CH_3CO	+	HO_2			$1.20{\cdot}10^{5}$	2.5	157.14
R170	CH_3CHO	+	$^3CH_2$			=	CH_3CO	+	CH_3			$2.50{\cdot}10^{12}$	0.0	15.9
R171	CH_3CHO	+	CH_3			=	CH_3CO	+	CH_4			$3.49{\cdot}10^{-10}$	6.21	6.82
3.10. C_2H_5 reactions														
R172	C_2H_5	+	M(1)			→	C_2H_4	+	H	+	M(1)	$4.10{\cdot}10^{13}$	0.0	166.8
											Low	$3.65{\cdot}10^{18}$	0.0	139.68
											Troe	0.75 97.0	1379.0	0.0
R173	C_2H_5	+	H			=	CH_3	+	CH_3			$4.22{\cdot}10^{13}$	0.0	0.0
R174	C_2H_5	+	O			=	CH_3CHO	+	H			$5.32{\cdot}10^{13}$	0.0	0.0
R175	C_2H_5	+	O			=	CH_2O	+	CH_3			$3.98{\cdot}10^{13}$	0.0	0.0
R176	C_2H_5	+	O_2			=	C_2H_4	+	HO_2			$2.41{\cdot}10^{10}$	0.0	0.0
R177	C_2H_5	+	CH_3			=	C_2H_4	+	CH_4			$9.03{\cdot}10^{11}$	0.0	0.0
R178	C_2H_5	+	C_2H_5			=	C_2H_4	+	C_2H_6			$1.40{\cdot}10^{12}$	0.0	0.0
3.11. C_2H_5O reactions														
R179	C_2H_5O					=	CH_3CHO	+	H			$2.00{\cdot}10^{14}$	0.0	97.0
R180	C_2H_5O					=	CH_2O	+	CH_3			$8.00{\cdot}10^{13}$	0.0	90.0
R181	C_2H_5O	+	H			=	CH_3CHO	+	H_2			$1.00{\cdot}10^{14}$	0.0	0.0
R182	C_2H_5O	+	O			=	CH_3CHO	+	OH			$1.21{\cdot}10^{14}$	0.0	0.0
R183	C_2H_5O	+	OH			=	CH_3CHO	+	H_2O			$1.00{\cdot}10^{14}$	0.0	0.0
R184	C_2H_5O	+	O_2			=	CH_3CHO	+	HO_2			$6.00{\cdot}10^{10}$	0.0	7.0
3.12. CH_3CHOH reactions														
R185	CH_3CHOH					=	CH_3CHO	+	H			$1.00{\cdot}10^{14}$	0.0	105.0
R186	CH_3CHOH	+	H			=	CH_3CHO	+	H_2			$3.00{\cdot}10^{13}$	0.0	0.0
R187	CH_3CHOH	+	O			=	CH_3CHO	+	OH			$1.20{\cdot}10^{14}$	0.0	0.0
R188	CH_3CHOH	+	OH			=	CH_3CHO	+	H_2O			$1.51{\cdot}10^{13}$	0.0	0.0
R189	CH_3CHOH	+	O_2			=	CH_3CHO	+	HO_2			$8.43{\cdot}10^{15}$	-1.2	0.0
	CH_3CHOH	+	O_2			=	CH_3CHO	+	HO_2			$4.82{\cdot}10^{14}$	0.0	20.1
3.13. CH_2CH_2OH reactions														
R190	CH_2CH_2OH					=	C_2H_4	+	OH			$1.00{\cdot}10^{14}$	0.0	140.0
R191	CH_2CH_2OH	+	H			=	CH_3CHO	+	H_2			$5.00{\cdot}10^{13}$	0.0	0.0

3.14. C_2H_5OH reactions												
R192	C_2H_5OH			=	CH_3	+	CH_2OH			$3.10{\cdot}10^{15}$	0.0	337.2
R193	C_2H_5OH			=	C_2H_5	+	OH			$5.00{\cdot}10^{16}$	0.0	381.6
R194	C_2H_5OH			=	C_2H_4	+	H_2O			$1.00{\cdot}10^{14}$	0.0	320.9
R195	C_2H_5OH	+	H	=	CH_3CHOH	+	H_2			$4.40{\cdot}10^{12}$	0.0	19.1
R196	C_2H_5OH	+	H	=	C_2H_5	+	H_2O			$5.90{\cdot}10^{11}$	0.0	14.4
R197	C_2H_5OH	+	O	=	CH_3CHOH	+	OH			$5.42{\cdot}10^{5}$	2.5	7.73
R198	C_2H_5OH	+	O	=	C_2H_5O	+	OH			$3.01{\cdot}10^{4}$	2.5	7.73
R199	C_2H_5OH	+	O	=	CH_2CH_2OH	+	OH			$3.01{\cdot}10^{4}$	2.5	7.73
R200	C_2H_5OH	+	OH	=	CH_3CHOH	+	H_2O			$2.14{\cdot}10^{7}$	1.78	-3.53
R201	C_2H_5OH	+	OH	=	C_2H_5O	+	H_2O			$9.03{\cdot}10^{5}$	1.78	-3.53
R202	C_2H_5OH	+	OH	=	CH_2CH_2OH	+	H_2O			$1.13{\cdot}10^{6}$	1.78	-3.53
R203	C_2H_5OH	+	HO_2	=	CH_3CHOH	+	H_2O_2			$6.30{\cdot}10^{12}$	0.0	81.1
R204	C_2H_5OH	+	CH_3	=	CH_3CHOH	+	CH_4			$4.70{\cdot}10^{11}$	0.0	40.57
R205	C_2H_5OH	+	CH_3	=	CH_2CH_2OH	+	CH_4			$3.61{\cdot}10^{10}$	0.0	39.91
R206	C_2H_5OH	+	CH_3	=	C_2H_5O	+	CH_4			$9.03{\cdot}10^{10}$	0.0	39.32
R207	C_2H_5OH	+	CH_3O	=	CH_3CHOH	+	CH_3OH			$2.00{\cdot}10^{11}$	0.0	29.3
R208	C_2H_5OH	+	CH_2O	=	C_2H_5O	+	CH_3O			$1.53{\cdot}10^{12}$	0.0	333.2
R209	C_2H_5OH	+	C_2H_5O	=	C_2H_5OH	+	CH_3CHOH			$2.00{\cdot}10^{11}$	0.0	29.3
3.15. C_2H_6 reactions												
R210	C_2H_6	+	H	=	C_2H_5	+	H_2			$9.82{\cdot}10^{13}$	0.0	38.58
R211	C_2H_6	+	O	=	C_2H_5	+	OH			$1.00{\cdot}10^{9}$	1.5	24.4
R212	C_2H_6	+	OH	=	C_2H_5	+	H_2O			$9.15{\cdot}10^{6}$	2.0	4.16
R213	C_2H_6	+	HO_2	=	C_2H_5	+	H_2O_2			$1.10{\cdot}10^{5}$	2.5	70.5
R214	C_2H_6	+	O_2	=	C_2H_5	+	HO_2			$7.29{\cdot}10^{5}$	2.5	205.69
R215	C_2H_6	+	$^3CH_2$	=	C_2H_5	+	CH_3			$2.20{\cdot}10^{13}$	0.0	36.3
R216	C_2H_6	+	CH_3	=	C_2H_5	+	CH_4			$5.60{\cdot}10^{10}$	0.0	39.41
	C_2H_6	+	CH_3	=	C_2H_5	+	CH_4			$8.43{\cdot}10^{14}$	0.0	93.12
R217	C_2H_6	+	CH	=	C_2H_4	+	CH_3			$1.08{\cdot}10^{14}$	0.0	-1.1
4. C_3–hydrocarbons oxidation												
4.1. C_3H_2 reactions												
R218	C_3H_2	+	O_2	=	CHO	+	HCCO			$1.00{\cdot}10^{13}$	0.0	0.0
R219	C_3H_3	+	OH	=	C_3H_2	+	H_2O			$2.00{\cdot}10^{13}$	0.0	0.0
4.2. C_3H_3 reactions												
R220	C_3H_3	+	O	→	CO	+	C_2H_3			$3.80{\cdot}10^{13}$	0.0	0.0
R221	C_3H_3	+	O_2	→	HCCO	+	CH_2O			$6.00{\cdot}10^{12}$	0.0	0.0
4.3. C_3H_4 reactions												
R222	C_3H_4	+	O	=	CH_2O	+	C_2H_2			$1.00{\cdot}10^{12}$	0.0	0.0
R223	C_3H_4	+	O	=	CHO	+	C_2H_3			$1.00{\cdot}10^{12}$	0.0	0.0
R224	C_3H_4	+	OH	=	CH_2O	+	C_2H_3			$1.00{\cdot}10^{12}$	0.0	0.0
R225	C_3H_4	+	OH	=	CHO	+	C_2H_4			$1.00{\cdot}10^{12}$	0.0	0.0
R226	C_3H_4	+	M(1)	=	H	+	C_3H_3	+	M(1)	$1.00{\cdot}10^{17}$	0.0	293.0
R227	C_3H_4	+	H	=	CH_3	+	C_2H_2			$2.00{\cdot}10^{13}$	0.0	10.0
R228	C_3H_4	+	H	=	H_2	+	C_3H_3			$1.00{\cdot}10^{12}$	0.0	6.3
R229	C_3H_4	+	C_2H	=	C_2H_2	+	C_3H_3			$1.00{\cdot}10^{13}$	0.0	0.0
R230	C_3H_4	+	CH_3	=	C_3H_3	+	CH_4			$2.00{\cdot}10^{12}$	0.0	32.2
4.4. C_3H_5 reactions												
R231	C_3H_5			=	C_3H_4	+	H			$3.98{\cdot}10^{13}$	0.0	293.1
R232	C_3H_5	+	H	=	C_3H_4	+	H_2			$1.81{\cdot}10^{13}$	0.0	0.0
R233	C_3H_5	+	O_2	=	C_3H_4	+	HO_2			$1.02{\cdot}10^{12}$	0.0	94.78
R234	C_3H_5	+	OH	=	C_3H_4	+	H_2O			$6.02{\cdot}10^{12}$	0.0	0.0
R235	C_3H_6	+	O_2	=	C_3H_5	+	HO_2			$1.90{\cdot}10^{12}$	0.0	163.8
R236	C_3H_5	+	CH_3	=	C_3H_4	+	CH_4			$3.61{\cdot}10^{11}$	0.0	0.0
R237	C_3H_5	+	C_3H_5	=	C_3H_6	+	C_3H_4			$6.02{\cdot}10^{10}$	0.0	0.0

R238	CH_3	+	C_2H_2	=	C_3H_5					$6.00{\cdot}10^{11}$	0.0	32.4
4.5. C_3H_6 reactions												
R239	C_3H_6			=	C_3H_5	+	H			$1.00{\cdot}10^{13}$	0.0	326.0
R240	C_3H_6			=	C_2H_3	+	CH_3			$1.10{\cdot}10^{21}$	-1.2	408.8
R241	C_3H_6	+	H	=	C_3H_5	+	H_2			$5.00{\cdot}10^{12}$	0.0	6.3
R242	C_3H_6	+	O	=	C_2H_4	+	CH_2O			$5.90{\cdot}10^{13}$	0.0	21.0
R243	C_3H_6	+	O	=	C_2H_5	+	CHO			$3.60{\cdot}10^{12}$	0.0	0.0
R244	C_3H_6	+	O	=	CH_3	+	CH_3CO			$5.00{\cdot}10^{12}$	0.0	2.5
R245	C_3H_6	+	OH	=	C_2H_5	+	CH_2O			$7.90{\cdot}10^{12}$	0.0	0.0
R246	C_3H_6	+	OH	=	CH_3	+	CH_3CHO			$5.10{\cdot}10^{12}$	0.0	0.0
R247	C_3H_6	+	OH	=	C_3H_5	+	H_2O			$4.00{\cdot}10^{12}$	0.0	0.0
R248	C_3H_6	+	CH_3	=	CH_4	+	C_3H_5			$8.91{\cdot}10^{10}$	0.0	35.6
R249	C_3H_6	+	C_2H_5	=	C_3H_5	+	C_2H_6			$1.00{\cdot}10^{11}$	0.0	38.5
4.6. n-C_3H_7 reactions												
R250	n-C_3H_7			=	CH_3	+	C_2H_4			$9.60{\cdot}10^{13}$	0.0	129.8
R251	n-C_3H_7			=	H	+	C_3H_6			$1.25{\cdot}10^{14}$	0.0	154.9
R252	n-C_3H_7	+	O_2	=	C_3H_6	+	HO_2			$1.00{\cdot}10^{12}$	0.0	20.9
4.7. i-C_3H_7 reactions												
R253	i-C_3H_7			=	H	+	C_3H_6			$6.30{\cdot}10^{13}$	0.0	154.5
R254	i-C_3H_7			=	CH_3	+	C_2H_4			$2.00{\cdot}10^{10}$	0.0	123.5
R255	i-C_3H_7	+	O_2	=	C_3H_6	+	HO_2			$1.99{\cdot}10^{10}$	0.0	-10.72
4.8. C_3H_8 reactions												
R256	C_3H_8	+	M(1)	=	CH_3	+	C_2H_5	+	M(1)	$4.00{\cdot}10^{23}$	-1.87	377.41
									Low	$2.24{\cdot}10^{19}$	0.0	271.87
									Troe	0.76 1946.0	38.0	0.0
R257	C_3H_8	+	H	=	H_2	+	n-C_3H_7			$1.30{\cdot}10^{14}$	0.0	40.6
R258	C_3H_8	+	H	=	H_2	+	i-C_3H_7			$1.00{\cdot}10^{14}$	0.0	34.9
R259	C_3H_8	+	O	=	n-C_3H_7	+	OH			$3.00{\cdot}10^{13}$	0.0	24.1
R260	C_3H_8	+	O	=	i-C_3H_7	+	OH			$2.60{\cdot}10^{13}$	0.0	18.7
R261	C_3H_8	+	OH	=	n-C_3H_7	+	H_2O			$3.70{\cdot}10^{12}$	0.0	6.9
R262	C_3H_8	+	OH	=	i-C_3H_7	+	H_2O			$2.80{\cdot}10^{12}$	0.0	3.6
R263	C_3H_8	+	HO_2	→	n-C_3H_7	+	H_2O_2			$1.14{\cdot}10^{13}$	0.0	81.2
R264	n-C_3H_7	+	H_2O_2	→	C_3H_8	+	HO_2			$2.33{\cdot}10^{12}$	0.0	41.1
R265	C_3H_8	+	HO_2	→	i-C_3H_7	+	H_2O_2			$3.40{\cdot}10^{12}$	0.0	71.2
R266	i-C_3H_7	+	H_2O_2	→	C_3H_8	+	HO_2			$4.16{\cdot}10^{11}$	0.0	31.1
R267	C_3H_8	+	CH_3	→	CH_4	+	n-C_3H_7			$4.00{\cdot}10^{11}$	0.0	39.8
R268	n-C_3H_7	+	CH_4	→	CH_3	+	C_3H_8			$3.12{\cdot}10^{12}$	0.0	68.9
R269	C_3H_8	+	CH_3	→	CH_4	+	i-C_3H_7			$1.30{\cdot}10^{12}$	0.0	48.6
R270	i-C_3H_7	+	CH_4	→	CH_3	+	C_3H_8			$1.01{\cdot}10^{13}$	0.0	77.7
R271	C_3H_8	+	O_2	→	n-C_3H_7	+	HO_2			$2.52{\cdot}10^{13}$	0.0	205.2
R272	n-C_3H_7	+	HO_2	→	C_3H_8	+	O_2			$2.08{\cdot}10^{12}$	0.0	0.0
R273	C_3H_8	+	O_2	→	i-C_3H_7	+	HO_2			$2.00{\cdot}10^{13}$	0.0	199.3
R274	i-C_3H_7	+	HO_2	→	C_3H_8	+	O_2			$2.08{\cdot}10^{12}$	0.0	0.0
R275	C_3H_8	+	CH_3O	→	n-C_3H_7	+	CH_3OH			$3.00{\cdot}10^{11}$	0.0	29.3
R276	n-C_3H_7	+	CH_3OH	→	C_3H_8	+	CH_3O			$1.22{\cdot}10^{10}$	0.0	38.5
R277	C_3H_8	+	CH_3O	→	i-C_3H_7	+	CH_3OH			$3.00{\cdot}10^{11}$	0.0	29.3
R278	i-C_3H_7	+	CH_3OH	→	C_3H_8	+	CH_3O			$1.22{\cdot}10^{10}$	0.0	38.5
5. C_4–hydrocarbons oxidation												
5.1. C_4H_2 reactions												
R279	C_4H_2	+	O	=	C_3H_2	+	CO			$7.89{\cdot}10^{12}$	0.0	5.64
R280	C_4H_2	+	OH	=	C_3H_2	+	CHO			$6.68{\cdot}10^{12}$	0.0	-1.71
5.2. C_4H_6 reactions												
R281	C_4H_6			=	C_2H_3	+	C_2H_3			$4.03{\cdot}10^{19}$	-1.0	411.0
R282	C_2H_3	+	C_2H_4	=	C_4H_6	+	H			$7.83{\cdot}10^{10}$	0.0	0.0

R283	C_4H_6	+	O	=	C_2H_4	+	CH_2CO			$1.00 \cdot 10^{12}$	0.0	0.0
R284	C_4H_6	+	O	=	CH_2O	+	C_3H_4			$1.00 \cdot 10^{12}$	0.0	0.0
R285	C_4H_6	+	OH	=	C_2H_5	+	CH_2CO			$1.00 \cdot 10^{12}$	0.0	0.0
R286	C_4H_6	+	OH	=	CH_2O	+	C_3H_5			$2.00 \cdot 10^{12}$	0.0	0.0
R287	C_4H_6	+	OH	=	C_2H_3	+	CH_3CHO			$5.00 \cdot 10^{12}$	0.0	0.0
5.3. C_4H_7 reactions												
R288	C_4H_7			=	C_4H_6	+	H			$1.20 \cdot 10^{14}$	0.0	206.4
R289	C_4H_7			=	C_2H_4	+	C_2H_3			$1.00 \cdot 10^{11}$	0.0	154.9
R290	C_4H_7	+	H	=	C_4H_6	+	H_2			$3.16 \cdot 10^{12}$	0.0	0.0
R291	C_4H_7	+	O_2	=	C_4H_6	+	HO_2			$1.00 \cdot 10^{11}$	0.0	0.0
R292	C_4H_7	+	C_4H_7	=	C_4H_6	+	1-C_4H_8			$3.16 \cdot 10^{12}$	0.0	0.0
R293	C_4H_7	+	CH_3	=	C_4H_6	+	CH_4			$1.00 \cdot 10^{13}$	0.0	0.0
R294	C_4H_7	+	C_2H_3	=	C_4H_6	+	C_2H_4			$4.00 \cdot 10^{12}$	0.0	0.0
R295	C_4H_7	+	C_2H_5	=	C_4H_6	+	C_2H_6			$4.00 \cdot 10^{12}$	0.0	0.0
R296	C_4H_7	+	C_2H_5	=	1-C_4H_8	+	C_2H_4			$5.00 \cdot 10^{11}$	0.0	0.0
R297	C_4H_7	+	C_2H_5	=	trans-2-C_4H_8	+	C_2H_4			$5.00 \cdot 10^{11}$	0.0	0.0
R298	C_4H_7	+	C_2H_5	=	cis-2-C_4H_8	+	C_2H_4			$5.00 \cdot 10^{11}$	0.0	0.0
R299	C_4H_7	+	C_3H_5	=	C_4H_6	+	C_3H_6			$4.00 \cdot 10^{13}$	0.0	0.0
5.4. 1-C_4H_8 reactions												
R300	1-C_4H_8			=	trans-2-C_4H_8					$4.00 \cdot 10^{11}$	0.0	251.0
R301	1-C_4H_8			=	cis-2-C_4H_8					$4.00 \cdot 10^{11}$	0.0	251.0
R302	1-C_4H_8			=	C_3H_5	+	CH_3			$8.00 \cdot 10^{16}$	0.0	307.4
R303	1-C_4H_8			=	C_2H_3	+	C_2H_5			$2.00 \cdot 10^{18}$	-1.0	405.2
R304	1-C_4H_8			=	H	+	C_4H_7			$4.11 \cdot 10^{18}$	-1.0	407.7
R305	1-C_4H_8	+	H	=	C_4H_7	+	H_2			$5.00 \cdot 10^{13}$	0.0	16.3
R306	1-C_4H_8	+	O	=	CH_3CHO	+	C_2H_4			$1.26 \cdot 10^{12}$	0.0	3.6
R307	1-C_4H_8	+	O	=	CH_3	+	C_2H_5	+	CO	$1.62 \cdot 10^{13}$	0.0	3.6
R308	1-C_4H_8	+	O	=	C_3H_6	+	CH_2O			$2.50 \cdot 10^{12}$	0.0	0.0
R309	1-C_4H_8	+	O	=	C_4H_7	+	OH			$1.30 \cdot 10^{13}$	0.0	18.8
R310	1-C_4H_8	+	OH	=	CH_3CHO	+	C_2H_5			$1.00 \cdot 10^{11}$	0.0	0.0
R311	1-C_4H_8	+	OH	=	CH_3	+	C_2H_6	+	CO	$1.00 \cdot 10^{10}$	0.0	0.0
R312	1-C_4H_8	+	OH	=	n-C_3H_7	+	CH_2O			$6.50 \cdot 10^{12}$	0.0	0.0
R313	1-C_4H_8	+	OH	=	C_4H_7	+	H_2O			$1.75 \cdot 10^{13}$	0.0	29.1
R314	1-C_4H_8	+	CH_3	=	C_4H_7	+	CH_4			$1.00 \cdot 10^{11}$	0.0	30.6
R315	1-C_4H_8	+	O_2	=	C_4H_7	+	HO_2			$4.00 \cdot 10^{12}$	0.0	167.4
R316	1-C_4H_8	+	HO_2	=	C_4H_7	+	H_2O_2			$1.00 \cdot 10^{11}$	0.0	71.4
R317	1-C_4H_8	+	C_2H_5	=	C_4H_7	+	C_2H_6			$1.00 \cdot 10^{11}$	0.0	33.5
R318	1-C_4H_8	+	C_3H_5	=	C_4H_7	+	C_3H_6			$8.00 \cdot 10^{10}$	0.0	51.9
R319	1-C_4H_8	+	C_4H_7	=	C_4H_7	+	trans-2-C_4H_8			$3.98 \cdot 10^{10}$	0.0	51.9
R320	1-C_4H_8	+	C_4H_7	=	C_4H_7	+	cis-2-C_4H_8			$3.98 \cdot 10^{10}$	0.0	51.9
5.5. trans-2-C_4H_8 reactions												
R321	trans-2-C_4H_8			=	H	+	C_4H_7			$4.11 \cdot 10^{18}$	-1.0	407.7
R322	trans-2-C_4H_8			=	CH_3	+	C_3H_5			$6.50 \cdot 10^{14}$	0.0	298.3
R323	trans-2-C_4H_8	+	H	=	C_4H_7	+	H_2			$5.00 \cdot 10^{12}$	0.0	14.6
R324	trans-2-C_4H_8	+	O	=	C_2H_4	+	CH_3CHO			$1.00 \cdot 10^{12}$	0.0	0.0
R325	trans-2-C_4H_8	+	O	=	i-C_3H_7	+	CHO			$6.03 \cdot 10^{12}$	0.0	0.0
R326	trans-2-C_4H_8	+	OH	=	C_4H_7	+	H_2O			$1.01 \cdot 10^{14}$	0.0	12.8
R327	trans-2-C_4H_8	+	OH	=	C_2H_5	+	CH_3CHO			$1.51 \cdot 10^{13}$	0.0	0.0
R328	trans-2-C_4H_8	+	CH_3	=	C_4H_7	+	CH_4			$1.00 \cdot 10^{11}$	0.0	34.3
5.6. c-2-C_4H_8 reactions												
R329	cis-2-C_4H_8			=	trans-2-C_4H_8					$1.00 \cdot 10^{13}$	0.0	259.4
R330	cis-2-C_4H_8			=	C_4H_6	+	H_2			$1.00 \cdot 10^{13}$	0.0	274.1
R331	cis-2-C_4H_8			=	C_4H_7	+	H			$4.07 \cdot 10^{18}$	-1.0	407.3
R332	cis-2-C_4H_8			=	C_3H_5	+	CH_3			$1.25 \cdot 10^{15}$	0.0	298.3

R333	cis-2-C_4H_8	+	H	=	C_4H_7	+	H_2	$1.00 \cdot 10^{12}$	0.0	14.6
R334	cis-2-C_4H_8	+	OH	=	C_4H_7	+	H_2O	$1.26 \cdot 10^{14}$	0.0	12.8
R335	cis-2-C_4H_8	+	OH	=	C_2H_5	+	CH_3CHO	$1.40 \cdot 10^{13}$	0.0	0.0
R336	cis-2-C_4H_8	+	O	=	i-C_3H_7	+	CHO	$6.03 \cdot 10^{12}$	0.0	0.0
R337	cis-2-C_4H_8	+	O	=	C_2H_4	+	CH_3CHO	$1.00 \cdot 10^{12}$	0.0	0.0
R338	cis-2-C_4H_8	+	CH_3	=	C_4H_7	+	CH_4	$1.00 \cdot 10^{11}$	0.0	34.3
5.7. p-C_4H_9 reactions										
R339	p-C_4H_9			=	C_2H_5	+	C_2H_4	$2.50 \cdot 10^{13}$	0.0	120.6
R340	p-C_4H_9			=	1-C_4H_8	+	H	$1.26 \cdot 10^{13}$	0.0	161.6
R341	p-C_4H_9	+	O_2	=	1-C_4H_8	+	HO_2	$1.00 \cdot 10^{12}$	0.0	8.4
5.8. s-C_4H_9 reactions										
R342	s-C_4H_9			=	1-C_4H_8	+	H	$2.00 \cdot 10^{13}$	0.0	169.2
R343	s-C_4H_9			=	trans-2-C_4H_8	+	H	$5.00 \cdot 10^{13}$	0.0	158.7
R344	s-C_4H_9			=	cis-2-C_4H_8	+	H	$5.00 \cdot 10^{13}$	0.0	158.7
R345	s-C_4H_9			=	C_3H_6	+	CH_3	$4.00 \cdot 10^{14}$	0.0	139.0
R346	s-C_4H_9	+	O_2	=	1-C_4H_8	+	HO_2	$2.00 \cdot 10^{12}$	0.0	18.8
R347	s-C_4H_9	+	O_2	=	trans-2-C_4H_8	+	HO_2	$2.00 \cdot 10^{13}$	0.0	17.8
R348	s-C_4H_9	+	O_2	=	cis-2-C_4H_8	+	HO_2	$2.00 \cdot 10^{13}$	0.0	17.8
5.9. C_4H_{10} reactions										
R349	C_2H_5	+	C_2H_5	=	C_4H_{10}			$8.00 \cdot 10^{12}$	0.0	0.0
R350	C_4H_{10}			→	n-C_3H_7	+	CH_3	$1.00 \cdot 10^{17}$	0.0	357.6
R351	n-C_3H_7	+	CH_3	→	C_4H_{10}			$2.00 \cdot 10^{13}$	0.0	0.0
R352	C_4H_{10}	+	H	→	p-C_4H_9	+	H_2	$5.63 \cdot 10^{7}$	2.0	32.2
R353	p-C_4H_9	+	H_2	→	C_4H_{10}	+	H	$9.12 \cdot 10^{12}$	0.0	60.6
R354	C_4H_{10}	+	H	→	s-C_4H_9	+	H_2	$1.75 \cdot 10^{7}$	2.0	20.9
R355	s-C_4H_9	+	H_2	→	C_4H_{10}	+	H	$1.54 \cdot 10^{13}$	0.0	66.5
R356	C_4H_{10}	+	O	→	p-C_4H_9	+	OH	$1.13 \cdot 10^{14}$	0.0	32.9
R357	p-C_4H_9	+	OH	→	C_4H_{10}	+	O	$1.48 \cdot 10^{13}$	0.0	51.3
R358	C_4H_{10}	+	O	→	s-C_4H_9	+	OH	$5.62 \cdot 10^{13}$	0.0	21.8
R359	s-C_4H_9	+	OH	→	C_4H_{10}	+	O	$7.35 \cdot 10^{12}$	0.0	40.2
R360	C_4H_{10}	+	OH	→	p-C_4H_9	+	H_2O	$4.13 \cdot 10^{7}$	1.7	3.2
R361	p-C_4H_9	+	H_2O	→	C_4H_{10}	+	OH	$7.17 \cdot 10^{7}$	1.7	93.3
R362	C_4H_{10}	+	OH	→	s-C_4H_9	+	H_2O	$7.23 \cdot 10^{7}$	1.6	-1.0
R363	s-C_4H_9	+	H_2O	→	C_4H_{10}	+	OH	$1.28 \cdot 10^{8}$	1.6	89.1
R364	C_4H_{10}	+	HO_2	→	p-C_4H_9	+	H_2O_2	$1.14 \cdot 10^{13}$	0.0	81.2
R365	p-C_4H_9	+	H_2O_2	→	C_4H_{10}	+	HO_2	$4.58 \cdot 10^{12}$	0.0	41.1
R366	C_4H_{10}	+	HO_2	→	s-C_4H_9	+	H_2O_2	$6.80 \cdot 10^{12}$	0.0	71.2
R367	s-C_4H_9	+	H_2O_2	→	C_4H_{10}	+	HO_2	$1.63 \cdot 10^{12}$	0.0	31.0
R368	C_4H_{10}	+	CH_3	→	p-C_4H_9	+	CH_4	$1.30 \cdot 10^{12}$	0.0	48.6
R369	p-C_4H_9	+	CH_4	→	C_4H_{10}	+	CH_3	$1.01 \cdot 10^{13}$	0.0	77.7
R370	C_4H_{10}	+	CH_3	→	s-C_4H_9	+	CH_4	$8.00 \cdot 10^{11}$	0.0	39.8
R371	s-C_4H_9	+	CH_4	→	C_4H_{10}	+	CH_3	$6.24 \cdot 10^{12}$	0.0	68.9
R372	C_4H_{10}	+	O_2	→	p-C_4H_9	+	HO_2	$2.50 \cdot 10^{13}$	0.0	205.2
R373	p-C_4H_9	+	HO_2	→	C_4H_{10}	+	O_2	$2.50 \cdot 10^{12}$	0.0	-9.2
R374	C_4H_{10}	+	O_2	→	s-C_4H_9	+	HO_2	$4.00 \cdot 10^{13}$	0.0	199.3
R375	s-C_4H_9	+	HO_2	→	C_4H_{10}	+	O_2	$4.07 \cdot 10^{12}$	0.0	-15.2
R376	C_4H_{10}	+	CH_3O	→	p-C_4H_9	+	CH_3OH	$3.00 \cdot 10^{11}$	0.0	29.3
R377	p-C_4H_9	+	CH_3OH	→	C_4H_{10}	+	CH_3O	$1.22 \cdot 10^{10}$	0.0	209.4
R378	C_4H_{10}	+	CH_3O	→	s-C_4H_9	+	CH_3OH	$6.00 \cdot 10^{11}$	0.0	29.3
R379	s-C_4H_9	+	CH_3OH	→	C_4H_{10}	+	CH_3O	$2.44 \cdot 10^{10}$	0.0	209.4
6. Iso mechanism										
6.1. i-C_4H_7 reactions										
R380	i-C_4H_7			=	C_3H_4	+	CH_3	$1.00 \cdot 10^{13}$	0.0	213.6
6.2. i-C_4H_8 reactions										

R381	i-C_4H_8					=	C_3H_5	+	CH_3	$5.00{\cdot}10^{18}$	-1.0	307.4
R382	i-C_4H_8					=	i-C_4H_7	+	H	$1.00{\cdot}10^{17}$	0.0	368.5
R383	i-C_4H_8	+	H			=	i-C_4H_7	+	H_2	$1.00{\cdot}10^{13}$	0.0	15.9
R384	i-C_4H_8	+	O			=	i-C_4H_7	+	OH	$2.50{\cdot}10^{5}$	2.6	-4.7
R385	i-C_4H_8	+	O			=	i-C_3H_7	+	CHO	$7.23{\cdot}10^{5}$	2.3	-4.4
R386	i-C_4H_8	+	OH			=	i-C_4H_7	+	H_2O	$9.60{\cdot}10^{12}$	0.0	5.2
R387	i-C_4H_8	+	OH			=	i-C_3H_7	+	CH_2O	$1.50{\cdot}10^{12}$	0.0	0.0
R388	i-C_4H_8	+	CH_3			=	i-C_4H_7	+	CH_4	$6.03{\cdot}10^{11}$	0.0	37.23
6.3. i-C_4H_9 reactions												
R389	i-C_4H_9					=	C_3H_6	+	CH_3	$2.00{\cdot}10^{13}$	0.0	125.34
R390	i-C_4H_9					=	i-C_4H_8	+	H	$1.00{\cdot}10^{14}$	0.0	151.88
R391	i-C_4H_9	+	O_2			=	i-C_4H_8	+	HO_2	$2.41{\cdot}10^{10}$	0.0	0.0
6.4. t-C_4H_9 reactions												
R392	t-C_4H_9					=	H	+	i-C_4H_8	$8.30{\cdot}10^{13}$	0.0	159.63
R393	t-C_4H_9					=	C_3H_6	+	CH_3	$1.00{\cdot}10^{16}$	0.0	193.0
R394	t-C_4H_9	+	O_2			=	i-C_4H_8	+	HO_2	$6.02{\cdot}10^{10}$	0.0	-13.22
R395	t-C_4H_9	+	t-C_4H_9			=	i-C_4H_{10}	+	i-C_4H_8	$7.23{\cdot}10^{16}$	-1.73	0.0
6.5. i-C_4H_{10} reactions												
R396	i-C_4H_{10}					=	CH_3	+	i-C_3H_7	$1.10{\cdot}10^{26}$	-2.61	377.98
R397	i-C_4H_{10}					=	t-C_4H_9	+	H	$1.00{\cdot}10^{15}$	0.0	390.7
R398	i-C_4H_{10}					=	i-C_4H_9	+	H	$1.00{\cdot}10^{15}$	0.0	410.4
R399	i-C_4H_{10}	+	H			=	t-C_4H_9	+	H_2	$6.02{\cdot}10^{5}$	2.4	10.81
R400	i-C_4H_{10}	+	H			=	i-C_4H_9	+	H_2	$1.81{\cdot}10^{6}$	2.54	28.27
R401	i-C_4H_{10}	+	O			=	t-C_4H_9	+	OH	$1.56{\cdot}10^{5}$	2.5	4.66
R402	i-C_4H_{10}	+	O			=	i-C_4H_9	+	OH	$4.28{\cdot}10^{5}$	2.5	15.25
R403	i-C_4H_{10}	+	OH			=	t-C_4H_9	+	H_2O	$5.73{\cdot}10^{10}$	0.51	0.27
R404	i-C_4H_{10}	+	OH			=	i-C_4H_9	+	H_2O	$2.29{\cdot}10^{8}$	1.53	3.24
R405	i-C_4H_{10}	+	HO_2			=	i-C_4H_9	+	H_2O_2	$3.01{\cdot}10^{4}$	2.55	64.85
R406	i-C_4H_{10}	+	HO_2			=	t-C_4H_9	+	H_2O_2	$3.61{\cdot}10^{3}$	2.55	44.07
R407	i-C_4H_{10}	+	CH_3			=	t-C_4H_9	+	CH_4	$9.04{\cdot}10^{-1}$	3.46	19.24
R408	i-C_4H_{10}	+	CH_3			=	i-C_4H_9	+	CH_4	$1.36{\cdot}10^{1}$	3.65	29.9
R409	i-C_4H_{10}	+	O_2			=	i-C_4H_9	+	HO_2	$4.04{\cdot}10^{13}$	0.0	213.1
R410	i-C_4H_{10}	+	O_2			=	t-C_4H_9	+	HO_2	$3.97{\cdot}10^{13}$	0.0	184.08
R411	i-C_4H_{10}	+	CH_3O_2			=	i-C_4H_9	+	CH_3O_2H	$3.01{\cdot}10^{4}$	2.55	64.85
R412	i-C_4H_{10}	+	CH_3O_2			=	t-C_4H_9	+	CH_3O_2H	$3.61{\cdot}10^{3}$	2.55	44.07
7. Chemiluminescence reactions												
7.1. OH* reactions												
R413	H	+	O	+	M(1)	=	OH*	+	M(1)	$1.5{\cdot}10^{13}$	0.0	25
R414	CH	+	O_2			=	OH*	+	CO	$1.8{\cdot}10^{11}$	0.0	0.0
R415	CHO	+	O			=	OH*	+	CO	$2.89{\cdot}10^{11}$	0.0	1.93
R416	OH*					=	OH			$1.45{\cdot}10^{6}$	0.0	0.0
R417	OH*	+	O_2			=	OH	+	O_2	$2.1{\cdot}10^{12}$	0.5	-2.02
R418	OH*	+	H_2O			=	OH	+	H_2O	$5.93{\cdot}10^{12}$	0.5	-3.61
R419	OH*	+	H_2			=	OH	+	H_2	$2.95{\cdot}10^{12}$	0.5	-1.86
R420	OH*	+	CO_2			=	OH	+	CO_2	$2.76{\cdot}10^{12}$	0.5	-4.06
R421	OH*	+	CO			=	OH	+	CO	$3.23{\cdot}10^{12}$	0.5	-3.3
R422	OH*	+	CH_4			=	OH	+	CH_4	$3.36{\cdot}10^{12}$	0.5	-2.66
R423	OH*	+	OH			=	OH	+	OH	$6.01{\cdot}10^{12}$	0.5	-3.19
R424	OH*	+	H			=	OH	+	H	$1.31{\cdot}10^{12}$	0.5	-0.7
R425	OH*	+	N_2			=	OH	+	N_2	$1.08{\cdot}10^{11}$	0.5	-5.19
R426	OH*	+	Ar			=	OH	+	Ar	$1.69{\cdot}10^{12}$	0.0	17.32
7.2. CH* reactions												
R427	C_2H	+	O_2			=	CH*	+	CO_2	$1.8{\cdot}10^{11}$	0.0	0.0
R428	C_2H	+	O			=	CH*	+	CO	$1.8{\cdot}10^{11}$	0.0	0.0

R429	C_2	+	OH	=	CH*	+	CO	$1.8{\cdot}10^{11}$	0.0	0.0
R430	CH*			=	CH			$1.86{\cdot}10^{6}$	0.0	0.0
R431	CH*	+	O_2	=	CH	+	O_2	$2.48{\cdot}10^{6}$	2.14	-7.2
R432	CH*	+	CO_2	=	CH	+	CO_2	$2.4{\cdot}10^{-1}$	4.3	-7.1
R433	CH*	+	CO	=	CH	+	CO	$2.44{\cdot}10^{12}$	0.5	0.0
R434	CH*	+	CH_4	=	CH	+	CH_4	$1.73{\cdot}10^{13}$	0.0	0.7
R435	CH*	+	H_2O	=	CH	+	H_2O	$5.3{\cdot}10^{13}$	0.0	0.0
R436	CH*	+	H	=	CH	+	H	$2.01{\cdot}10^{14}$	0.0	5.7
R437	CH*	+	OH	=	CH	+	OH	$7.13{\cdot}10^{13}$	0.0	5.7
R438	CH*	+	H_2	=	CH	+	H_2	$1.47{\cdot}10^{14}$	0.0	5.7
R439	CH*	+	N_2	=	CH	+	N_2	$3.03{\cdot}10^{2}$	3.4	-1.6
R440	CH*	+	Ar	=	CH	+	Ar	$3.13{\cdot}10^{11}$	0.0	0.0
7.3. C_2* reactions										
R441	$^1CH_2$	+	C	=	C_2*	+	H_2	$2.4{\cdot}10^{12}$	0.0	0.0
R442	C_3	+	O	=	C_2*	+	CO	$5.2{\cdot}10^{11}$	0.0	0.0
R443	C_2*			=	C_2			$1.0{\cdot}10^{7}$	0.0	0.0
R444	C_2*	+	O_2	=	C_2	+	O_2	$4.8{\cdot}10^{13}$	0.0	0.0
R445	C_2*	+	CO_2	=	C_2	+	CO_2	$4.8{\cdot}10^{13}$	0.0	0.0
R446	C_2*	+	H_2O	=	C_2	+	H_2O	$4.8{\cdot}10^{13}$	0.0	0.0
R447	C_2*	+	CO	=	C_2	+	CO	$4.8{\cdot}10^{13}$	0.0	0.0
R448	C_2*	+	CH_4	=	C_2	+	CH_4	$4.8{\cdot}10^{13}$	0.0	0.0
R449	C_2*	+	H	=	C_2	+	H	$4.8{\cdot}10^{13}$	0.0	0.0
R450	C_2*	+	H_2	=	C_2	+	H_2	$4.8{\cdot}10^{13}$	0.0	0.0
R451	C_2*	+	OH	=	C_2	+	OH	$4.8{\cdot}10^{13}$	0.0	0.0
R452	C_2*	+	Ar	=	C_2	+	Ar	$4.8{\cdot}10^{13}$	0.0	0.0
8.1. C reactions										
R453	C	+	H_2O	=	CHO	+	H	$3.0{\cdot}10^{12}$	0.0	0.0
R454	C	+	OH	=	H	+	CO	$5.0{\cdot}10^{13}$	0.0	0.0
R455	C	+	OH	=	CH	+	O	$2.41{\cdot}10^{14}$	0.0	91.0
R456	C	+	CH	=	C_2	+	H	$1.0{\cdot}10^{13}$	0.0	0.0
R457	C	+	$^1CH_2$	=	C_2	+	H_2	$3.0{\cdot}10^{12}$	0.0	0.0
R458	C	+	$^3CH_2$	=	C_2	+	H_2	$3.0{\cdot}10^{12}$	0.0	0.0
8.2. C_2 reactions										
R459	C_2H	+	O	=	C_2	+	OH	$1.2{\cdot}10^{13}$	0.0	0.0
R460	C_2H	+	H	=	C_2	+	H_2	$6.2{\cdot}10^{13}$	0.0	73.0
R461	C_2	+	OH	=	C_2O	+	H	$5.0{\cdot}10^{13}$	0.0	0.0
R462	C_2	+	O_2	=	CO	+	CO	$9.0{\cdot}10^{12}$	0.0	4.1
R463	C_2	+	O	=	CO	+	C	$1.0{\cdot}10^{14}$	0.0	0.0
R464	C_2	+	OH	=	CH	+	CO	$5.0{\cdot}10^{13}$	0.0	0.0
R465	C_2	+	CH_4	=	C_2H	+	CH_3	$3.0{\cdot}10^{13}$	0.0	2.47
R466	C_2	+	C_2H_2	=	C_2H	+	C_2H	$1.0{\cdot}10^{14}$	0.0	0.0
R467	C_2	+	C_2H_4	=	C_2H	+	C_2H_3	$1.0{\cdot}10^{14}$	0.0	0.0
R468	C_2	+	C_2H_6	=	C_2H	+	C_2H_5	$5.0{\cdot}10^{13}$	0.0	0.0
8.3. C_2O reactions										
R469	C_2	+	O_2	=	C_2O	+	O	$2.0{\cdot}10^{14}$	0.0	33.8
R470	CH	+	CO	=	C_2O	+	H	$1.9{\cdot}10^{11}$	0.0	0.0
R471	C_2O	+	H	=	CH	+	CO	$4.8{\cdot}10^{13}$	0.0	0.0
R472	C_2O	+	O	=	CO	+	CO	$4.8{\cdot}10^{13}$	0.0	0.0
R473	C_2O	+	OH	=	CH	+	CO_2	$2.0{\cdot}10^{13}$	0.0	0.0
8.4. C_3 reactions										
R474	C	+	C_2H	=	C_3	+	H	$2.0{\cdot}10^{16}$	-1.0	0.0
R475	C_2	+	CH	=	C_3	+	H	$5.0{\cdot}10^{13}$	0.0	0.0
R476	C_3	+	OH	=	CO	+	C_2H	$2.0{\cdot}10^{13}$	0.0	0.0
R477	C_3	+	O_2	=	CO_2	+	C_2	$9.0{\cdot}10^{12}$	0.0	46.1

R478	C_3	+	O	=	CO	+	C_2	$5.0{\cdot}10^{13}$	0.0	0.0
8.5. C_3H_2 reactions										
R479	CH	+	C_2H_2	=	C_3H_2	+	H	$9.4{\cdot}10^{13}$	0.0	-2.09
R480	C_3H	+	H_2	=	C_3H_2	+	H	$4.0{\cdot}10^{05}$	2.4	4.2
R481	C_3H_2	+	O	=	CHO	+	C_2H	$4.0{\cdot}10^{13}$	0.0	0.0
R482	C_3H_2	+	OH	=	CHO	+	C_2H_2	$1.0{\cdot}10^{13}$	0.0	0.0
8.6. C_3H reactions										
R483	C_3	+	H_2	=	C_3H	+	H	$4.1{\cdot}10^{5}$	2.4	92.0
R484	CH	+	C_2H	=	C_3H	+	H	$5.0{\cdot}10^{13}$	0.0	0.0
R485	C_3H	+	O	=	CO	+	C_2H	$4.0{\cdot}10^{13}$	0.0	0.0
R486	C_3H	+	OH	=	CO	+	C_2H_2	$2.0{\cdot}10^{13}$	0.0	0.0
R487	C_3H	+	O_2	=	CO	+	HCCO	$3.0{\cdot}10^{13}$	0.0	0.0

Erklärung

Hiermit versichere ich, daß ich die Arbeit selbständig verfaßt und keine anderen als die angegebenen Quellen und Hilfsmittel verwendet habe.

Heidelberg, den 29.03.2011

Trupti Kathrotia